N 69 32557

NASA CR-72491
WRL 8962-18-F

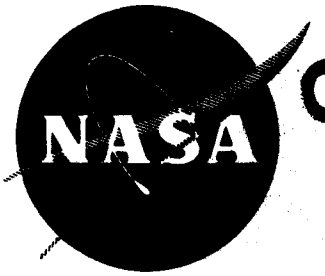

MEASUREMENT OF TEMPERATURE PROFILES IN HOT GASES BY EMISSION-ABSORPTION SPECTROSCOPY

by
F. S. Simmons, H. Y. Yamada, and C. B. Arnold

INFRARED AND OPTICS LABORATORY
WILLOW RUN LABORATORIES
THE UNIVERSITY OF MICHIGAN

prepared for
NATIONAL AERONAUTICS AND SPACE ADMINISTRATION

NASA Lewis Research Center
Contract NAS3-9419
Carl B. Norgren, Project Manager
Air Breathing Engines Division
Donald R. Buchele, Research Advisor
Instrument and Computing Division

NOTICES

Sponsorship. The work reported herein was conducted by the Willow Run Laboratories of the Institute of Science and Technology for the National Aeronautics and Space Administration under NASA Contract NAS 3-9419 with Mr. Carl B. Norgren, Air Breathing Engines Division, as Project Manager. Contracts and grants to The University of Michigan for the support of sponsored research are administered through the Office of the Vice-President for Research.

Availability Notice. Requests for copies of this report should be referred to

National Aeronautics and Space Administration
Scientific and Technical Information Facility
P. O. Box 33
College Park, Md. 20740

NASA CR-72491
WRL 8962-18-F

FINAL REPORT

MEASUREMENT OF TEMPERATURE PROFILES IN HOT GASES BY EMISSION-ABSORPTION SPECTROSCOPY

by
F. S. Simmons, H. Y. Yamada, and C. B. Arnold

Infrared and Optics Laboratory
Willow Run Laboratories
The University of Michigan
Ann Arbor

prepared for
NATIONAL AERONAUTICS AND SPACE ADMINISTRATION

April 1969

CONTRACT NAS3-9419

NASA Lewis Research Center
Cleveland, Ohio
Carl B. Norgren, Project Manager
Air Breathing Engines Division
Donald R. Buchele, Research Advisor
Instrument and Computing Division

ABSTRACT

Measurements of spectral radiances and absorptances in the 2-3-μm region are presented for several samples of H_2O, CO_2, and HF, and a mixture of H_2O, CO_2, and N_2 in a 60-cm cell heated in a furnace such that various temperature profiles could be imposed along the optical path. The spectral data were converted into apparent temperatures corresponding to the ratio of spectral radiance to absorptance as a function of frequency. Temperature profiles in the sample gases were deduced from the variation of apparent temperature with absorptance, using molecular band-model calculations and assuming knowledge of the profile shape. The deduced temperature profiles are shown to agree quite well with direct measurements by thermocouples attached to the cell.

CONTENTS

FIGURES

MEASUREMENT OF TEMPERATURE PROFILES IN HOT GASES BY EMISSION-ABSORPTION SPECTROSCOPY
Final Report

SUMMARY

This study was undertaken to explore the application of infrared emission-absorption spectroscopy as a means of determining temperature profiles in nonuniform hot gases such as the exhaust jets of advanced air-breathing engines. Experimental measurements were made using a double-beam ratio-recording spectrometer which could accommodate long sample cells heated in a segmented furnace so that various temperature profiles could be maintained in the gas sample. Spectral radiances and absorptances in the 2-3-μm region were obtained for various pressures and temperature profiles in H_2O vapor, CO_2, HF, and a mixture of CO_2, H_2O, and N_2 in a 60-cm cell. The spectral data were reduced to apparent temperatures, which are defined as those temperatures the Planck functions of which are the observed ratios of spectral radiance to absorptance, as a function of frequency throughout the various vibration-rotation bands.

A general computer program was written for the calculation of molecular radiative transfer. For the case of polyatomic molecules, the calculation was based on a band model consisting of a random array of lines of nearly equal intensity; for diatomic molecules exhibiting nonoverlapping lines, the calculation was based on expressions for the total radiances and equivalent widths of Lorentz lines for nonisothermal paths. Calculations based on the temperature profile in the cell measured by thermocouples were shown to agree well with the observed spectra.

The inversion of the observed radiance and absorptance measurements proceeded in the following manner. The general shape of the temperature profile in the sample was assumed to be known, and was approximated in terms of simple geometric forms so that the profile could be characterized in terms of a few parameters. These parameters were then adjusted in straightforward calculations using the appropriate radiative-transfer expression until a best fit was obtained with the observed spectra. It was found to be most convenient and reliable to fit the band-model calculations to plots of apparent temperature vs. absorptance, and the isolated-line calculations to plots of apparent temperature vs. a generalized rotational quantum number. The resultant temperature profiles so deduced showed satisfactory agreement with the thermocouple measurements in all cases except those in which an inappropriate profile shape was assumed.

It was therefore concluded that infrared emission-absorption spectroscopy applied in this manner shows excellent promise as a fairly simple and reliable means of determining temperature profiles in hot gas streams such as the exhausts of jet or rocket engines for which a priori knowledge of the general shape of the temperature profile is available. However, some further development of the method would be requisite; in particular, it would be most appropriate to carry out an investigation exploring combustion products in a laboratory apparatus before proceeding to applications involving full-size jet or rocket engines.

1
INTRODUCTION

Since the turn of the century, spectroscopy has seen wide use as the means for determining temperatures in hot gaseous sources ranging from stellar atmospheres to the flame of a bunsen burner. The basic principles involved and the many experimental techniques that have been employed are well documented in the literature, and have been reviewed in a number of textbooks [1-3] and in the proceedings of periodic symposia on temperature measurements [4]. However, most of this work has been based on the simplifying assumption that the gas is a completely equilibrated isothermal source, and much of it on the further assumption that the gas is optically thin. For the latter case, measurements of the spectral distribution of emission (or absorption) alone is sufficient, in principle, for the determination of temperature. However, when appreciable self-absorption of emitted radiation must be accounted for, then measurements of both emission and absorption are required; hence the term emission-absorption pyrometry.

For nonisothermal gases in local thermodynamic equilibrium, the application of either spectral distribution or absorption-emission techniques to determine a single "effective temperature" can be shown to produce a result with little meaning: the value of the resultant "temperature" would be wavelength dependent, hence not a parameter useful for characterizing the physical state of the gas.

For the case in which thermal equilibrium does not prevail even locally, there are difficulties in even defining temperature; hence, measurements in either optically thin or dense gases lack meaning in correspondence with the extent of the disequilibrium.

The present study has been restricted to gases of appreciable optical depths in local thermodynamic equilibrium, and is concerned with the measurement of temperature profiles using infrared emission-absorption spectroscopy. The specific objective of the work is to explore the utility of this experimental technique as a possible diagnostic tool for the performance evaluation of advanced air-breathing engines.

Previous studies at The University of Michigan were concerned with the problem of calculating infrared radiation from highly nonuniform hot gaseous sources. In the course of that work, expressions were derived for the integrated radiances and equivalent widths of isolated spectral lines [5-7], and applied in band-model expressions for the more general case [8]. Calculated values of the net spectral radiances from hot sources, in which the temperature profiles were known, were then shown to compare well with direct observations [9].

In this work, the inverse problem is considered: given the observed emission and absorption spectra, how well can the temperature profile within a nonisothermal source be deduced?

2
THEORETICAL BACKGROUND

2.1. DEFINITIONS AND BASIC RELATIONS

Throughout this report, the radiometric symbols and nomenclature are those approved by the Commission on Symbols, Units, and Nomenclature of the International Union of Pure and Applied Physics. All symbols are defined in appendix E.

The governing equation for emission-absorption pyrometry derives from Kirchhoff's law of radiation, and is given by

$$L_\nu^*(T^*) = L_\nu/\alpha(\nu) \tag{1}$$

where L_ν is the observed spectral radiance (specific intensity) at a frequency ν along a particular line of sight through the gas and $\alpha(\nu)$ is the corresponding spectral absorptance; their ratio, L_ν^*, is designated as the Planck function of an apparent temperature, T^*. For uniform isothermal systems, T^* can be identified as the true thermodynamic temperature, T, and equation (1) can be directly applied. For all other cases, T^* is an apparent temperature which is nothing but a convenient alternative expression of an effective blackbody spectral radiance.

A distinction should be noted between T^* and a quantity often referred to as an "apparent temperature," T_{br}, which is more appropriately termed the "brightness temperature," and is defined by

$$L_\nu \equiv L_\nu^*(T_{br}) \tag{2}$$

Thus T_{br} is seen to be an alternative expression of spectral radiance; i.e., it is that temperature at which the Planck function gives the observed radiance. Correspondingly, T^* is an alternative expression of the ratio of spectral radiance to spectral absorptance; both are therefore functions of wavelength in general. It might be noted that spectral radiance can also be expressed in terms of a spectral emissivity, $\epsilon(\nu)$, defined by

$$L_\nu \equiv \epsilon(\nu)L_\nu^*(T) \tag{3}$$

The quantity $\epsilon(\nu)$ is equal to the spectral absorptance in an isothermal gas, by virtue of Kirchhoff's law, but of course loses its meaning in a nonisothermal gas.

The spectral radiance and absorptance in equation 1, in the strictest sense, refer to radiation in a spectral interval between ν and $\nu + d\nu$; actually, of course, measurements are always made of the average radiant power in a finite interval $\delta\nu$. For isothermal gases, it is easy to prove that the ratio of observed radiance to absorptance is independent of the spectral

interval $\delta\nu$, represented by the response function of the measuring instrument, provided only that it remain the same for both the emission and the absorption measurement [10], hence justifying the identification of T^* as T in equation 1. For the nonisothermal case, this is not generally so, and equation 1 in its simple form is of little use; more of the details of the origin of the radiation are required, as outlined in the sections to follow.

2.2. NONISOTHERMAL GROWTH

Consider an isolated spectral line of a gas in local thermodynamic equilibrium, as observed with an instrument of moderate resolution, having a slit function $g(\nu)$ whose effective width $\delta\nu$ is much greater than the line width. The indication of a well-behaved instrument, linear in response, would be proportional to the total radiance, L, of the spectral line:

$$L \equiv \int_0^\infty g(\nu) L_\nu \, d\nu \tag{4}$$

Infrared lines at ordinary pressures and temperatures exhibit contours well described by the Lorentz dispersion formula, giving for the spectral absorption coefficient, $k(\nu, T)$,

$$k(\nu, T) = \frac{S(T)}{\pi} \frac{\gamma(P, T)}{\gamma^2 + (\nu - \nu_0)^2} \tag{5}$$

where S(T) is the line strength, ν_0 is the line center frequency, and $\gamma [= \gamma(P, T)]$ is the pressure- and temperature-dependent half-width.

If equation 5 is substituted into the equation of radiative transfer in integral form, an appropriate transformation introduced, and integration made over frequency, the resultant relation is [5]

$$L = 2\pi\gamma_e \int_0^{f(x_L)} L_\nu^*(f) \, df \tag{6}$$

where γ_e is an effective (mass-weighted) average line width, and $f [= f(x)]$ is the Ladenburg-Reiche function

$$f(x) = xe^{-x}[J_0(ix) - iJ_1(ix)] \tag{7}$$

J_0 and J_1 being Bessel functions of the first kind with the argument, the dimensionless optical depth x, defined by

$$x = (2\pi\gamma_e)^{-1} \int_0^X S(X')F(X') \, dX' \tag{8}$$

in which X is the ordinary optical depth (cm-atm), S(X) is the temperature-dependent line strength, and $F(X) = 1$ or $\gamma(X)/\gamma_e$, respectively, for nearly weak or nearly strong lines. Use of a function $F(X) = [\gamma(X)/\gamma_e]^\eta$, where $0 < \eta < 1$ is an empirical factor, provides a

convenient means of interpolation between the two [5]. The prime in equation 8 simply indicates the quantity as a variable of integration; the quantity x_L in equation 6 is the value of x for the entire path through the nonisothermal gas.

In this case, the integrated absorptance, usually termed the equivalent width, W, is given by

$$W = 2\pi\gamma_e f(x_L) \tag{9}$$

(The corresponding relations for Doppler lines are given in reference 6.)

Although collision theory can in some cases provide Lorentz half-widths, values are more generally taken from semi-empirical expressions such as

$$\gamma(P, T) = \gamma_0(P_o, T_o)\frac{P}{P_o}\left(\frac{T_o}{T}\right)^n \tag{10}$$

in which γ_0, the line width at reference pressure P_o and reference temperature T_o, and the exponent n are experimentally determined. Acceptance of a value n = 1/2, which follows from simple kinetic theory, and neglect of the dependence of half-width on rotational quantum number, are usually considered justifiable for engineering purposes.

2.3. BAND-MODEL FORMULATIONS

Equation 6 can easily be extended to a molecular band consisting of nonoverlapping spectral lines. In this case, the quantities of interest are the average spectral radiance and absorptance in the interval $\delta\nu$, which are given by

$$\bar{L}_\nu = \beta_e \int_0^{f(\bar{x}_L)} L_\nu^*(\bar{f})\, d\bar{f} \tag{11}$$

and

$$\bar{\alpha}(\nu) = \beta_e f(\bar{x}_L) \tag{12}$$

in which β_e is the effective value of a factor characterizing the extent of line overlapping:

$$\beta = 2\pi\bar{\gamma}/d \tag{12a}$$

where $\bar{\gamma}$ is the average line half-width and d is the average spacing between lines. In this case, $\bar{f} = f(\bar{x})$, in which the dimensionless optical depth $\bar{x}$ is defined by

$$\bar{x} = \beta_e^{-1} \int_0^X \bar{k}(X')F(X')\, dX' \tag{13}$$

where

$$\bar{k} = \bar{S}/d \tag{13a}$$

is the average spectral absorption coefficient, the ratio of average line strength to average spacing, and $F(X) = (\beta/\beta_e)^{\eta}$ in analogy to the single-line case.

Equation 11 can be further extended to handle molecular bands in which line overlapping is appreciable [8]; the resultant expressions for average spectral radiance and absorptance are:

$$\bar{L}_\nu = \beta_e \int_0^{f(\bar{x}_L)} L_\nu^*(\bar{f}) \exp[-\beta_e \bar{f}]\, d\bar{f} \tag{14}$$

and

$$\bar{\alpha}_L = 1 - \exp[-\beta_e f(\bar{x}_L)] \tag{15}$$

If an average transmittance, $\bar{\tau}$, is defined by

$$\bar{\tau} = 1 - \bar{\alpha} = \exp[-\beta_e f(\bar{x})] \tag{16}$$

equation 14 can be rewritten simply as

$$\bar{L}_\nu = \int_{\bar{\tau}_L}^{1} L_\nu^*(\bar{\tau})\, d\bar{\tau} \tag{17}$$

Equation 17 is in form the radiative-transfer expression used in experimental studies at Warner and Swasey [11], General Dynamics [12], and in calculations carried out at NASA MSFC [13]; equation 14 is the form used in previous studies at this laboratory [14]. The derivation of a comparable expression in a slightly different form, and examples of its use in some hypothetical flames in which neither line strengths nor widths varied with temperature, have also recently been reported [15].

Equations 11, 12, 14, and 15 reduce to more familiar forms for the strong- and weak-line limits [9]; however, there is little advantage in using such approximations for nonisothermal calculations. A machine calculation would be used in any event, and the above equations are about as easy to program. There is some advantage, however, in using a simple analytical approximation to the Ladenburg-Reiche function [16]; this will be discussed in more detail in section 2.4.

Equation 17 can also be extended to handle mixtures of gases. Since the spectral line positions in the vibration-rotation bands of different gases would be uncorrelated, the incremental transmittances would be multiplicative. In this case, $\bar{\tau}$ would represent the product incremental transmittance, which would be used in the summation to yield the observed radiance.

2.4. EVALUATION OF BAND-MODEL PARAMETERS

In principle, there are two methods by which the band-model parameters, equations 12a and 13a (or any other pair formed from the three basic variables: the line strengths, widths,

and positions) can be evaluated. Detailed information on these line parameters can be appropriately averaged, or the lumped quantities can be determined directly by experiment. The former approach has been applied in calculations of atmospheric transmission in the infrared [17]; however, for hot gases, the population of higher rotational and vibrational states results in an increase in the numbers of lines and in the appearance of hot bands of uncertain strengths. Hence, for polyatomic molecules with their various degrees of freedom, such an approach is not practical at the present time for most engineering purposes. (A line-by-line calculation of the opacity of hot water vapor in cool stars has been made recently [18]; a total of 2.3 million lines were included in the calculation, which required 40 hours of IBM 7094 computer time.) On the other hand, for some diatomic molecules, e.g., HF, there is sufficient and reliable information on strengths and widths with which one could proceed in such a manner. However, the need for a band-model diminishes and line-by-line calculations become more feasible as the number of lines requiring consideration becomes smaller.

The alternative method for evaluating band-model parameters is by direct experimental observations using isothermal samples of the emitting-absorbing gas. The average spectral absorption coefficient, equation 13a, is obtained from observations for path lengths and pressures low enough that the gas is optically thin; i.e., all lines are weak and hence their growth is linear. This condition is specified by $x \to 0$, for which equation 12 reduces to

$$\bar{k}(\nu, T) = \bar{\alpha}(\nu, T)/X_L, \quad \alpha(\nu, T) \ll 1 \tag{18}$$

where X_L is the optical depth in cm-atm and $\bar{\alpha}(\nu, T)$ is the observed average spectral absorptance in the interval $\delta\nu$. Note that the necessary condition is that $\alpha(\nu, T) \ll 1$, not $\bar{\alpha}(\nu, T) \ll 1$. The latter condition can and very often does only signify that the resolution of the observing instrument is low (i.e., the slit function is much greater than line widths); this situation could therefore be encountered with the lines themselves being strong. Accordingly, in practice, observations using a number of path lengths are required to establish that the growth is linear. Note also that reduction in pressure alone is not sufficient; although the optical depth $X = PL$ will decrease, since the line width varies directly with pressure (cf. eq. 10), the absorptance will not decrease at the line center as rapidly as elsewhere, so that the required condition of linear growth cannot be readily observed for arbitrary values of path length.

Evaluation of the other band-model parameter requires measurements in which all lines are strong; i.e., the growth varies as the square root of the optical depth. These conditions permit the evaluation of the quantity

$$[(\bar{S}/d)(\bar{\gamma}/d)]^{1/2} = \frac{\bar{\alpha}(\nu, T)}{2X^{1/2}}, \quad \alpha(\nu_0, T) \sim 1 \tag{19}$$

from which the line overlap factor (eq. 12a) can be extracted. This evaluation is more difficult than the other for several reasons. The long path lengths required for most of the lines in the $\delta\nu$ to become strong, especially in the wings and troughs of bands, create experimental difficulties; for the large amounts of absorber required, line overlapping cannot be completely

eliminated; and the unavoidable presence of some weak lines compromises to some extent the validity of the results.

Again, variation of pressure alone is not sufficient; increasing concentrations of absorbers for a given path length do increase the optical depth, but the concomitant broadening of the lines tends to lower absorptances at the line center, thus obviating square-root growth.

In practice, both band-model parameters are evaluated by experiments in which a sufficient range of path lengths can be achieved so that the variation from linear to square-root growth can be observed. The extent to which this can be accomplished is the principal factor limiting the accurate evaluation of band-model parameters and hence the utility of band models for radiating gases.

An important and often overlooked fact is that band models, although based on theoretical principles, in effect are empirical formulations requiring as input experimentally determined parameters. Hence, it is not imperative that the parameters $\bar{k}$ and β truly represent the ratios of mean line strength to spacing and mean line width to spacing; there is an arbitrary character to these quantities in the first place, since one must prescribe a lower limit to the strengths of lines to be considered in a detailed analysis. Therefore, the question of how realistically a particular band model represents an actual molecule is not of prime importance. The significant question is how well it functions in its capacity as an interpolation device to utilize isothermal laboratory measurements for calculations of radiative transfer in inhomogeneous gases. In this light, the use of more complex band models based on more realistic assumptions regarding properties of the lines in a molecular band is not necessarily desirable. In fact, as illustrated below, the advantage can be largely illusory.

Equations 11, 12, 14, and 15 were derived for a molecular band consisting of Lorentz lines of nearly equal strengths randomly positioned. In order to illustrate the fact that more realistic line-intensity distributions do not necessarily improve the model, consider equation 12 for the case of identical nonoverlapping Lorentz lines in an isothermal gas. In the interval $\delta\nu$

$$\bar{\alpha}(\nu, T) = \beta f(x) \tag{20}$$

where β is defined by equation 12a and $x = SX/2\pi\gamma$. Consider now an array of nonoverlapping Lorentz lines with a probability distribution of strength $p(S) = \bar{S}^{-1} \exp[-S/\bar{S}]$ where p(S) is the probability of finding a line of strength S in the interval S, S + dS and $\bar{S}$ is the mean line strength in the interval $\delta\nu$. It is easy to show that in this case [19]

$$\bar{\alpha}_p(\nu, T) = \frac{2\pi(\bar{\gamma}/d_p)x_p}{\sqrt{1 + 2x_p}} \tag{21}$$

where $x_p = \bar{S}X/2\pi\bar{\gamma}$. The subscript p in this case denotes a probability strength distribution.

These nonoverlapping models are the special cases of the two corresponding general models, which are appropriate to the evaluation of the two band-model parameters. In the weak-line limit, equations 20 and 21 reduce to

$$x \to 0, \quad \bar{\alpha} \to 2\pi(\bar{\gamma}/d)x \tag{22}$$

$$x_p \to 0, \quad \bar{\alpha}_p \to 2\pi(\bar{\gamma}/d_p)x_p \tag{23}$$

and in the strong-line limit to:

$$x \to \infty, \quad \bar{\alpha} \to 2(\bar{\gamma}/d)\sqrt{2\pi x} \tag{24}$$

$$x_p \to \infty, \quad \bar{\alpha}_p \to \pi(\bar{\gamma}/d_p)\sqrt{2x_p} \tag{25}$$

Since the values of $\bar{S}$ and d_p will depend on an arbitrary lower limit of intensity below which one could identify large numbers of very low intensity lines not worthy of considering in a particular problem, these quantities are not precisely defined, and may be chosen to suit convenience. Consider the consequences of equating (22) with (23), and (24) with (25):

$$\bar{S}/d_p = \bar{S}/d \tag{26}$$

$$\bar{\gamma}/d_p = (4/\pi)(\bar{\gamma}/d) \tag{27}$$

and

$$x_p = (\pi/4)x \tag{28}$$

Substituting (27) and (28) into (21):

$$\bar{\alpha}_p = \frac{2\pi(\bar{\gamma}/d)x}{\sqrt{1 + (\pi/2)x}} \tag{29}$$

in which the quantity $x/\sqrt{1 + (\pi/2)x}$ is the approximation to the Ladenburg-Reiche function $xe^{-x}[J_0(ix) - iJ_1(ix)]$ that has been recently proposed [16]. Hence, the two band models yield essentially the same results, and by virtue of (26) and (27), band-model parameters obtained through the use of one model may be used with the other. The above result illustrates the more general fact that calculations with band models are not particularly sensitive to the line strength distribution function that is assumed in the formulation. This fact is best illustrated in figure 3 of reference 19, in which the experimental data of several investigators are fitted equally well by the Ladenburg-Reiche curve of growth, representing the band-model formulation used in the present study, as by one based on a more realistic distribution of line strengths. An analysis of errors to be expected in the application of various band-model approximations to inhomogeneous gases is given in reference 20.

2.5. EMISSION-ABSORPTION PYROMETRY

Consider now the application of emission-absorption spectroscopy to the case of an inhomogeneous nonisothermal gas in local thermodynamic equilibrium. For this case, the ratio of observed spectral radiance to spectral absorptance will vary with optical depth,hence in general with wavelength. At a particular wavelength, the value of the spectral absorptance will depend primarily on the absorber concentration profile; the value of spectral radiance depends

on both the concentration and the temperature profiles. For observations at moderate resolution, at a particular wavelength the indicated values of both quantities will depend on the instrument slit opening, but their ratio will not. Therefore, while in principle spectral radiance and absorptance distributions could be analyzed to determine temperature and concentration profiles, the analysis of the emission-absorption ratio offers the considerable advantage of eliminating the uncertainties introduced by inexact knowledge of the shape and width of the instrument slit function.

Consider first the case of isolated Lorentz spectral lines treated individually. Upon substitution of equations 6 and 9, equation 1 becomes [5]

$$L_\nu^*(T^*) = \frac{1}{f(x_L)} \int_0^{f(x_L)} L_\nu^*(f)\,df \tag{30}$$

where f(x) and x are defined by equations 7 and 8. Equation 30 indicates the manner in which the blackbody radiance of the local temperature within the nonisothermal body of gas is averaged along the line of sight; in essence it represents the appropriate weighting of the blackbody radiance function of the local temperatures by concentration and line-strength variations.

Equation 30 also represents the emission-absorption expression for the case of a molecular band consisting of nonoverlapping Lorentz lines, if x is replaced with $\bar{x}$ as defined by equation 13.

For the case of a molecular band with some line overlapping, substitution of equations 16 and 17 into equation 1 yields

$$L_\nu^*(T^*) = (1 - \bar{\tau}_L)^{-1} \int_{\bar{\tau}_L}^{1} L_\nu^*(\bar{\tau})\,d\bar{\tau} \tag{31}$$

There are basically two approaches through which temperature profiles can be deduced from a set of measurements of spectral radiances and absorptances at various wavelengths. Given a set of T^*, the values of T can in principle be obtained by an appropriate inverse transformation, i.e., a mathematical inversion of (30) or (31). This inversion could in principle be accomplished analytically as, for example, in the case of the Abel transform applied to the expression for the observed transverse radiance of an optically thin axisymmetric source. In practice, such inversions must generally be handled numerically. The problem in essence is the solution of a set of n radiance equations to obtain a temperature profile approximated by n isothermal zones. The n equations must represent n substantially different optical depths; this can be achieved either by n observations at a particular frequency but different path lengths (as in the transverse scan of an axisymmetric source) or by observations at n frequencies for the same path. The latter case is more generally applicable, but also more difficult in that the n equations must be solved simultaneously rather than sequentially. Generally, moderate-resolution molecular-band radiation is utilized in such studies; however the same principle applies to high-resolution observations of the contour of an isolated spectral line.

This method appears to be straightforward: spectral data are obtained at n frequencies and used to solve n simultaneous radiance equations for n unknown local temperatures along the line of sight. However, the problem is not so simple because of the nonlinearity of the Planck function and the factors governing the growth of spectral lines, in particular the strongly nonlinear variation of line strengths with temperature. The main difficulties encountered are the mathematical instabilities and nonuniqueness of solutions which result primarily from the imprecision of the input data. Further discussions of these problems are to be found in the recent literature, much of which is concerned with the deduction of atmospheric temperature profiles from satellite observations [21-26].

The alternative approach, and the one employed in this investigation, in essence consists of a set of straightforward calculations using equations 30 or 31 and a model by which the temperature profile within the nonuniform body of gas is characterized by a very few parameters which are adjusted until the best agreement is obtained between calculated and observed values of T^*. This approach, which can also be characterized as an inversion in the broadest sense, does, of course, presume some prior knowledge of the shape of the temperature profile. However, this requirement is not much of a constraint for many engineering applications in which the general pattern of a high-temperature flow field can easily be specified. Likewise the argument that, mathematically, the minimization of differences between observed and calculated T^* does not necessarily imply a corresponding minimum between actual and calculated T [27] need not be a deterrent to this approach. Under the imposed constraint of a known shape to the temperature profile, it is difficult to see how large errors could be engendered by this approach. On this pragmatic basis, then, the present investigation was carried out, the objective being to determine how well temperature profiles could be so deduced, and thereby to assess the utility of emission-absorption spectroscopy so applied.

3
EXPERIMENTAL PROGRAM

3.1. APPARATUS AND PROCEDURES

The apparatus used in this investigation is shown in figure 1. In essence, it consists of a segmented combustion-tube furnace, housing a sample cell 60 cm in length, and positioned in one beam of a double-beam ratio-recording spectrometer which had been designed specifically for the study of emission and absorption in nonisothermal gases [28].

Figure 2 is a schematic of the optical arrangement. Light from a graphite-tube blackbody source [29] is split into two beams by a pair of diagonals and redirected into a pair of spherical mirrors. One beam passes through the sample cell in the furnace; the two beams are collected by another pair of spherical mirrors which reimage the blackbody aperture onto the slit of the monochromator. Iris diaphragms at each of the second pair of spheres serve to limit the angular field and to balance the beams.

Each chopper is made with two rows of holes differing in number so that the two beams are chopped at different frequencies, 420 and 780 Hz, which were chosen to facilitate signal separation. For absorption measurements, the chopper next to the blackbody is used; thus emission from the hot gas is not sensed. For emission measurements, the chopper next to the monochromator is used with the upstream shutter in the sample beam closed after the beams are balanced; thus the ratio of emission from the furnace to that of the blackbody is obtained.

The monochromator is equipped with a 300 lines/mm grating blazed at 3 μm. A germanium filter in front of the entrance slit cuts off the radiation below 1.8 μm to eliminate second-order light. An elliptical mirror images the exit slit onto a PbS detector, a 0.25 × 2.0-mm Type P Kodak Ektron cell installed in a Dewar and cooled with liquid nitrogen.

The entire optical path outside the sample cell is thoroughly flushed by dry nitrogen in order to minimize absorption due to H_2O and CO_2 present in the atmosphere.

The electronic circuit is illustrated in figure 3. The signal from the detector is amplified, separated into two components by a filter network, and synchronously rectified by a demodulation circuit which is controlled by the signals of two photodiodes facing a pair of small lamps across the chopper. The intermodulation between beams was determined to be less than 1%, and through the use of a set of sectored discs rotated at high speed in the sample beam, the linearity of the entire system was established to be within 1%.

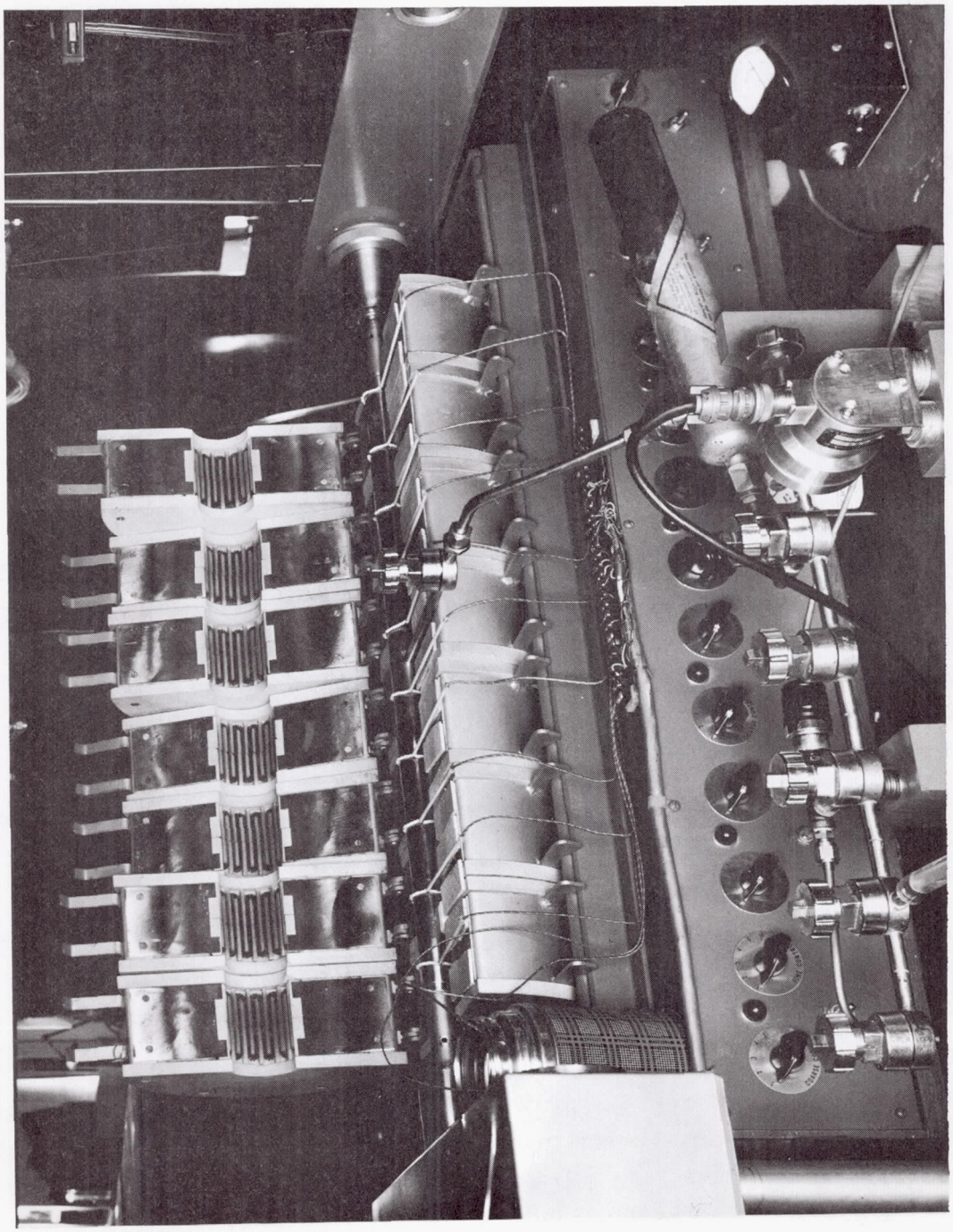

FIGURE 1. EXPERIMENTAL APPARATUS

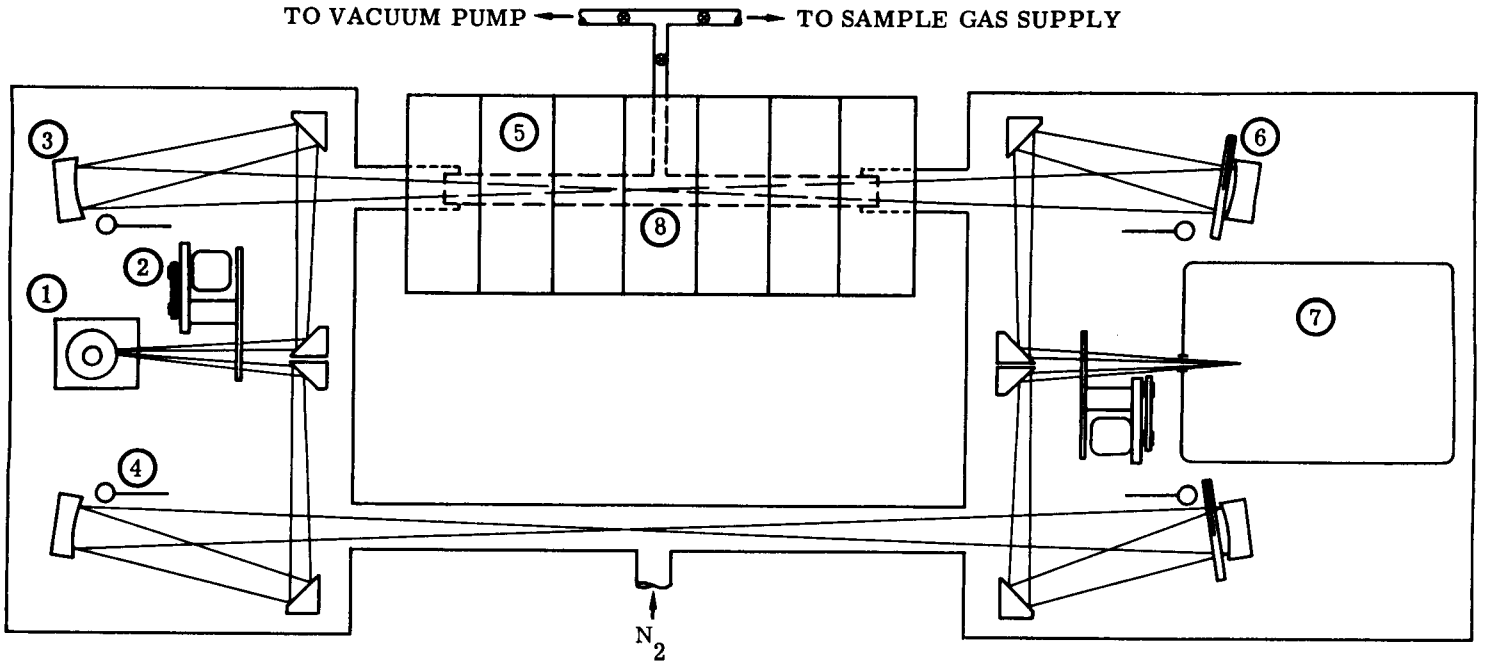

① BLACKBODY
② CHOPPER
③ SPHERICAL MIRROR
④ SHUTTER
⑤ 7-SECTION FURNACE
⑥ IRIS DIAPHRAGM
⑦ GRATING MONOCHROMATOR
⑧ TEST CELL

FIGURE 2. OPTICAL ARRANGEMENT

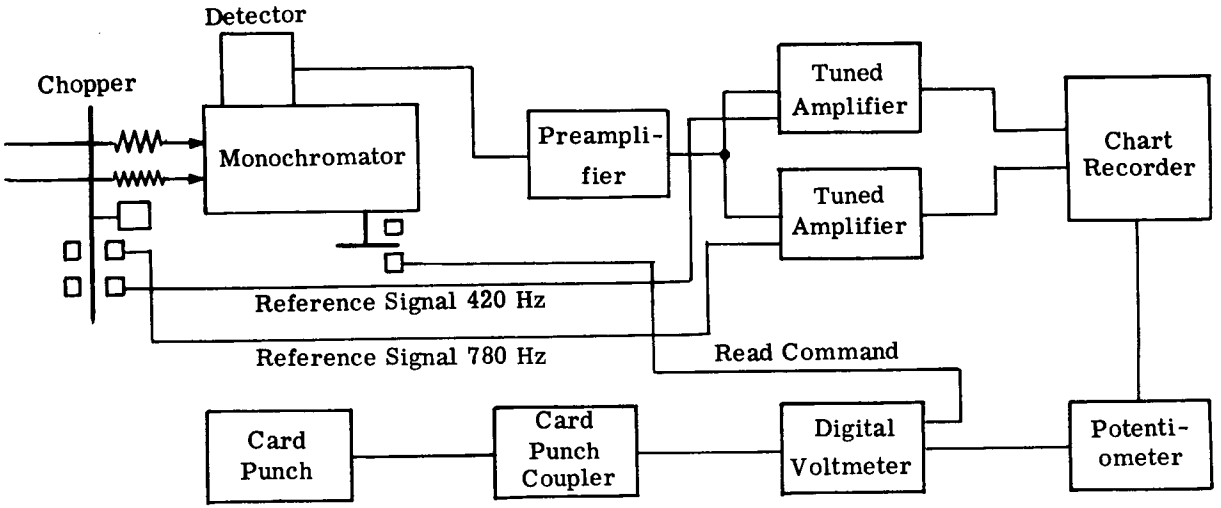

FIGURE 3. ELECTRONIC CIRCUIT

The output signals were displayed on a recording potentiometer. The reference beam signal was placed across the slide wire and the sample signal across the slider, so that the ratio of radiances in the two beams was indicated. A multiple-turn potentiometer connected to the shaft of the slider provided a signal which was passed through an analog-to-digital converter and recorded on punched cards; the readout command signal for the card punch was provided by a photodiode facing a lamp across a slotted disc on the monochromator wavelength drive.

Two types of sample cells were used in the present study; both were 60 cm in length and approximately 25 mm in diameter. The data for H_2O and CO_2 were obtained using a cell fabricated from fused silica; for the HF measurements, a Monel cell with bonded sapphire windows was fabricated. Carbon dioxide and hydrogen fluoride samples were admitted to the evacuated cell from supply cylinders through appropriate plumbing; the amount was monitored and measured with a bonded strain-gage absolute-pressure transducer. A liquid-nitrogen cold-trap and a mechanical pump comprised the vacuum system for disposing of the samples. Water vapor samples were introduced and measured by the arrangement shown in figure 4. The cell was evacuated and maintained at a uniform temperature. Distilled water was heated in a flask to a temperature at which the vapor pressure had the desired value. Since the sample cell and connecting tubes were maintained at a higher temperature than that of the flask, no condensation could occur during loading. Hence, the optical depth of the sample could be specified by the temperature of the cell and the vapor pressure in the flask. The CO_2 was of a purity commercially available. However, in order to eliminate H_2O from the HF samples, additional purification was carried out by the procedure described in reference 30.

Charges of H_2O and CO_2 could be contained in the quartz sample cell indefinitely with no long-term change in partial pressure detectable either by direct measurement or by observation of absorption. However, in spite of thorough presoaking, charges of HF would gradually diminish, presumably as the consequence of adsorption on the Monel cell walls. During the course of a run involving emission and absorption scans, decreases on the order of several percent were encountered. Therefore, data were collected in the following sequence: absorption, emission, absorption; the two absorption scans were then averaged prior to combination with the emission data for the evaluation of apparent temperatures. The partial pressures indicated in table I for these runs accordingly represent the average of the initial and final values.

The temperature distribution in the sample cell was measured by 10 chromel-alumel thermocouples equally spaced with one at the plane of each window. For the H_2O and CO_2 measurements, the thermocouples were welded to a thin stainless-steel sleeve which fitted closely over the quartz sample cell; for the HF measurements, the thermocouples were welded directly to the Monel cell. In an earlier study [31], in order to ascertain whether the temperature profile in the gas sample within the cell could be reliably assumed to be that measured along the outside wall of the cell, a test was made as illustrated in figure 5. The sample cell was simulated

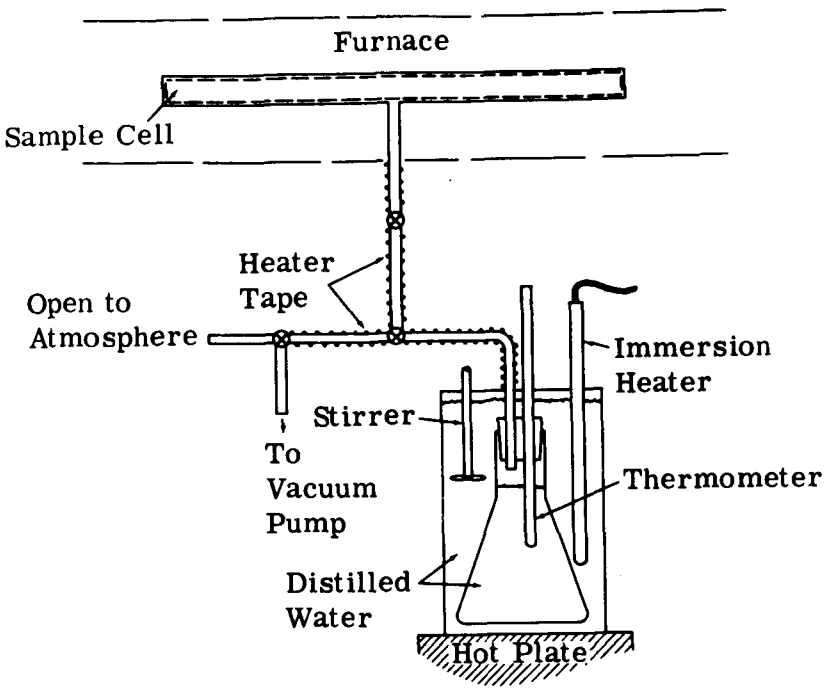

FIGURE 4. METHOD FOR LOADING CELL WITH WATER VAPOR

TABLE I. SUMMARY OF EXPERIMENTAL CONDITIONS

Run	Gas	P (mm Hg)	Temperatures (^{o}K) (Station 1 closest to monochromator) 1	2	3	4	5	6	7	8	9	10
10216803	CO_2	1520	1146	1147	1144	1146	1143	1146	1146	1147	1146	1148
10216811	H_2O	670	382	537	723	953	1128	1160	990	751	558	389
10216812	CO_2	760	386	528	719	953	1130	1160	979	737	541	387
10246808	CO_2	760	390	464	537	641	715	824	914	994	1061	1153
10246813	H_2O	692	392	513	593	671	745	835	918	993	1059	1152
10286811	CO_2	760	424	649	884	1147	1147	1149	1147	873	637	424
10286816	CO_2	760	368	535	813 (1193)*	1136	855 (1135)	871	1136	812 (1197)	541	374
10286821	CO_2	760	518	1132	1160	781	1060	1062	777	1160	1114	536
12056804	HF	397	498	723	892	1105	1184 (1224)	1189	1090	908	725	497
12056808	HF	751	494	723	896	1107	1186 (1234)	1189	1092	908	725	489
12056812	HF	191	488	725	898	1112	1192	1199	1100	913	729	485
12276804	HF	367	645	1073	1189	1209	1056	934	1206	1182	1093	644
12276807	HF	760	643	1046	1194	1212	1060	934	1209	1178	1074	643
	H_2O	57										
10216807	CO_2	28	378	537	723	958	1127	1158	990	752	555	383
	N_2	675										
	H_2O	54										
10246812	CO_2	28	395	517	594	673	744	833	915	990	1057	1153
	N_2	679										
10246818	CO	1520	388	485	554	639	729	831	918	994	1061	1150

*Values in parentheses obtained between stations using movable thermocouple.

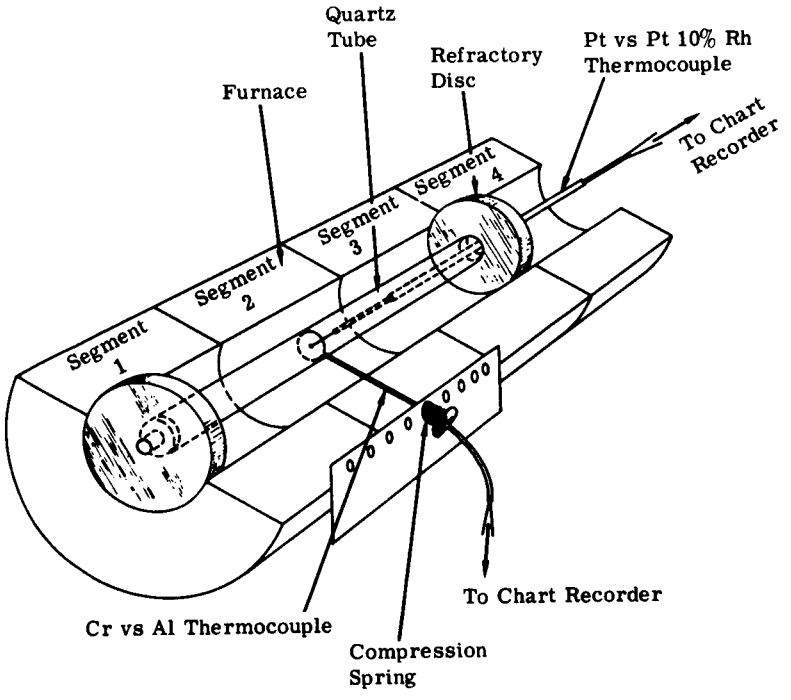

FIGURE 5. VERIFICATION OF TEMPERATURE-PROFILE MEASUREMENT

by a fused silica tube 1 ft long and 1 in. in diameter, mounted in the furnace between two refractory discs. The outside temperature was measured with chronel-alumel thermocouples looped about the tube; the air temperature within the tube was measured by a small-gauge platinum-platinum 10% rhodium thermocouple. Negligible differences were observed between the outside and inside temperatures at any station; hence it was concluded that the radial gradient would be insignificant at any plane for a sample gas whose thermal conductivity was comparable to that of air at a pressure of 1 atm.

The wavelength calibration of the spectrometer followed from the observed spectrum of HF. The line positions for HF are very well known, so that this gas represents perhaps the best available calibration source for infrared spectrometers operating in the region 2.3 to 3.5 μm. The slit function of the spectrometer was deduced from the observations of the weaker lines in the HF bands; its shape was very nearly triangular, and the half-width was approximately constant with wavelength, hence varied with frequency. Most of the data were obtained at a slit opening such that the effective slit width varied from about 2.5 cm^{-1} at 3000 cm^{-1} to 5.0 cm^{-1} at 4000 cm^{-1}.

The intensity calibration of the spectrometer could be made in one of two fashions. With a mirror on the back side of one of the downstream shutters, the temperature of the blackbody could be observed using an optical pyrometer. However, this procedure required a correction for the fact that the mirror reflectances and window transmittances varied from 0.65 μm, where the optical pyrometer bandpass was centered, to 2.5 μm, where the measurements were made; and the magnitudes of these corrections were difficult to accurately evaluate in situ. Therefore, an alternative calibration procedure was adopted: a blackbody source whose emission in the 2.7-μm region could be accurately evaluated was positioned in the sample beam. The most convenient source for this method was a 2-atm charge of CO_2 in the sample cell itself, which was then maintained at a temperature as close as possible to isothermal. The center of the 2.7-μm CO_2 band was black under these conditions; hence its emission could be obtained from the Planck function of the measured cell temperature. Under the above isothermal conditions with an optically dense charge in the cell, the emission from the cell window, being at the same temperature as the gas in the cell, did not influence the observed radiation. However, in general, a correction for window emission was required; the manner in which this was incorporated into the data reduction procedure is detailed in appendix A.

The raw data recorded on punched cards were processed using the University's IBM 360 computer; the reduced data were provided on punched cards from which an automatic curve plotter could in convenient format produce the spectra in terms of spectral radiance or absorptance, plotted against wavelength or frequency as desired.

3.2. PRESENTATION OF SPECTRA

Spectral radiances and absorptances in the 2.7-μm region were measured for a number of temperature profiles using pure samples of H_2O vapor and CO_2. Measurements were also obtained for two of the profiles using a mixture of these gases with nitrogen in a proportion simulating the products of combustion of CH_4 with air at a fuel/air weight ratio of 0.02 (except that the surplus oxygen was replaced with nitrogen). Finally, a number of observations were made of the 2.3-μm overtone band of CO and the 2.5-μm fundamental band of HF. Table I summarizes the data collected and the conditions of the measurements.

A complete set of radiance and absorptance spectra are presented in appendix B. The data for CO_2, H_2O, and CO were collected using the automatic card-punching output of the spectrometer; hence, the reduced data are displayed. The resultant spectra for the CO_2 and H_2O runs are quite faithful to the original chart recordings that were also obtained. On the other hand, the strength of the 2.3-μm overtone band of CO is so weak that, even with the high cell loadings, the reduced spectra were considerably altered in appearance because of the uncertainties in the very low values of the observed absorptances. The data for HF were collected only by chart recording, since punched-card recording of the widely separated intense lines with fidelity would have required very long scan times which were not desirable for several reasons. Accordingly, the radiance and absorptance spectra for HF are reproductions of the original recordings; the full-scale lines for emission were traced in by superimposing the appropriate prerun or postrun scans with the cell evacuated.

3.3. COMPARISONS WITH PREDICTED SPECTRA

The deduction of temperature profiles from observed spectra is a much more uncertain process than the calculation of nonisothermal spectra given the temperature profile. Accordingly, it is in order to examine first how well nonisothermal spectra can be calculated using a band-model expression. Therefore, a number of the spectra obtained in this study were compared with radiances and absorptances predicted as follows.

Equations 16 and 17, as combined in equation 31, were programmed, using a trapezoidal approximation, in Fortran IV language for computation by University's IBM 360 computer. Equation 31 not only encompasses the nonoverlapping band-model approximation but also the isolated line expression as given by equation 30. The General Dynamics tabulations of band-model parameters for H_2O and CO_2 were used in the present investigation [12, 32]; a sample calculation is shown in appendix C. Figures 6 through 9 are typical of the observed values of spectral radiance, absorptance, and apparent temperatures for H_2O and CO_2 in comparison with the predicted values. In general, the agreement is satsifactory.

For HF, computed values of line strengths and widths [33, 34] were used in equation 30. Since the large charges of HF in the 60-cm cell produced considerable overlapping in the wings

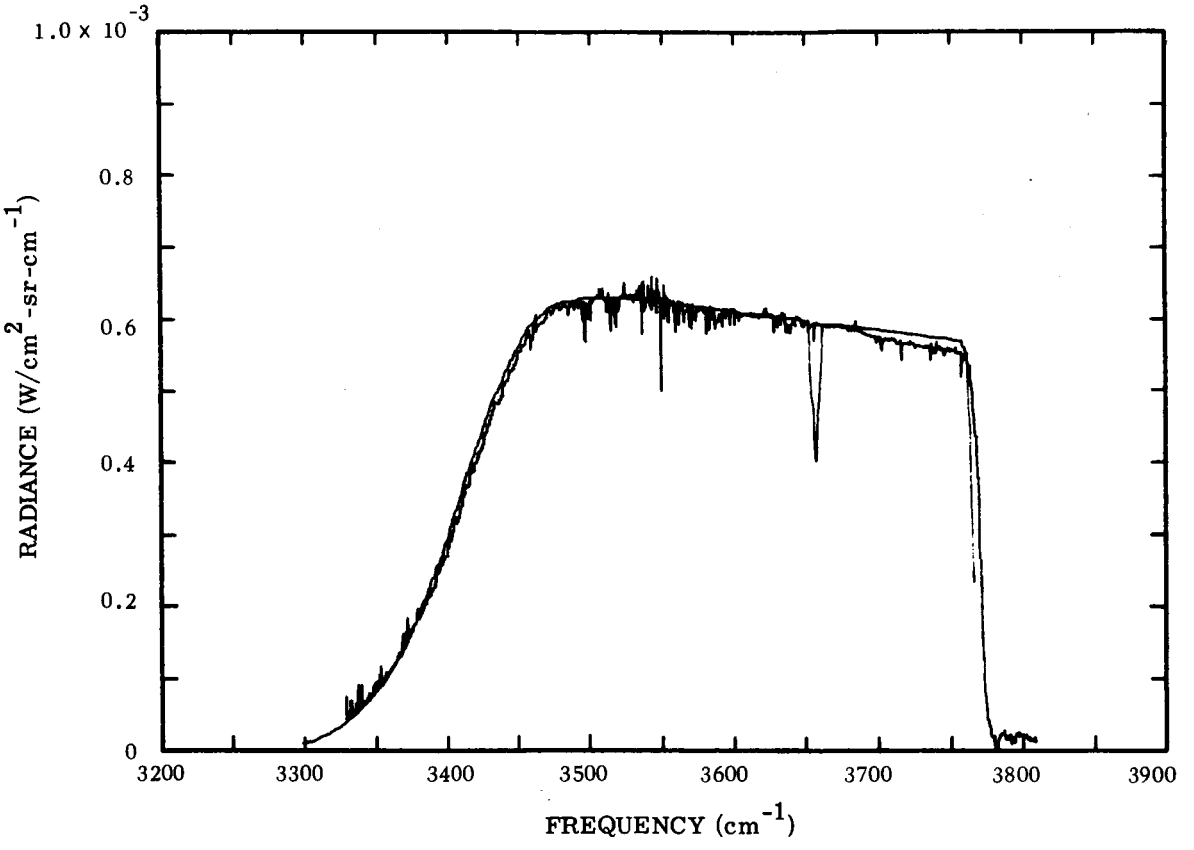

(a) Radiance vs. Frequency

FIGURE 6. COMPARISON OF ISOTHERMAL CO_2 SPECTRA WITH BAND-MODEL CALCULATIONS (RUN 10216803)

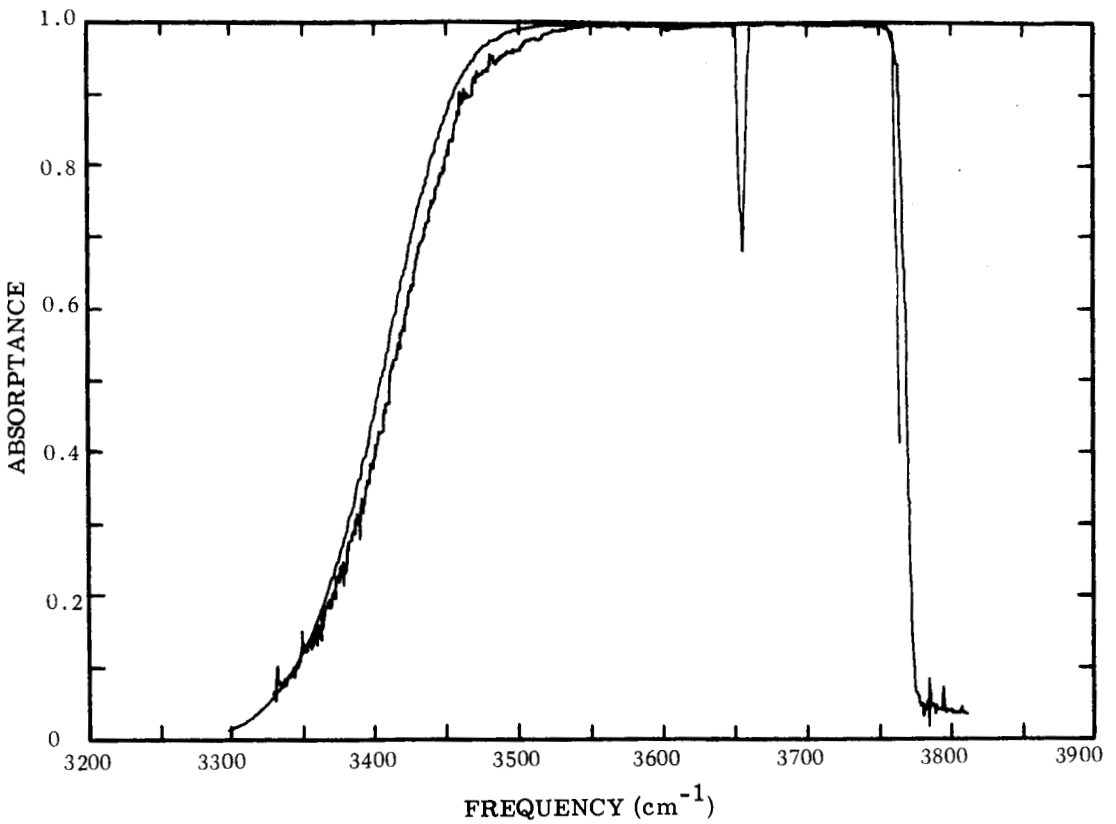

(b) Absorptance vs. Frequency

FIGURE 6. COMPARISON OF ISOTHERMAL CO_2 SPECTRA WITH BAND-MODEL CALCULATIONS (RUN 10216803) (Continued)

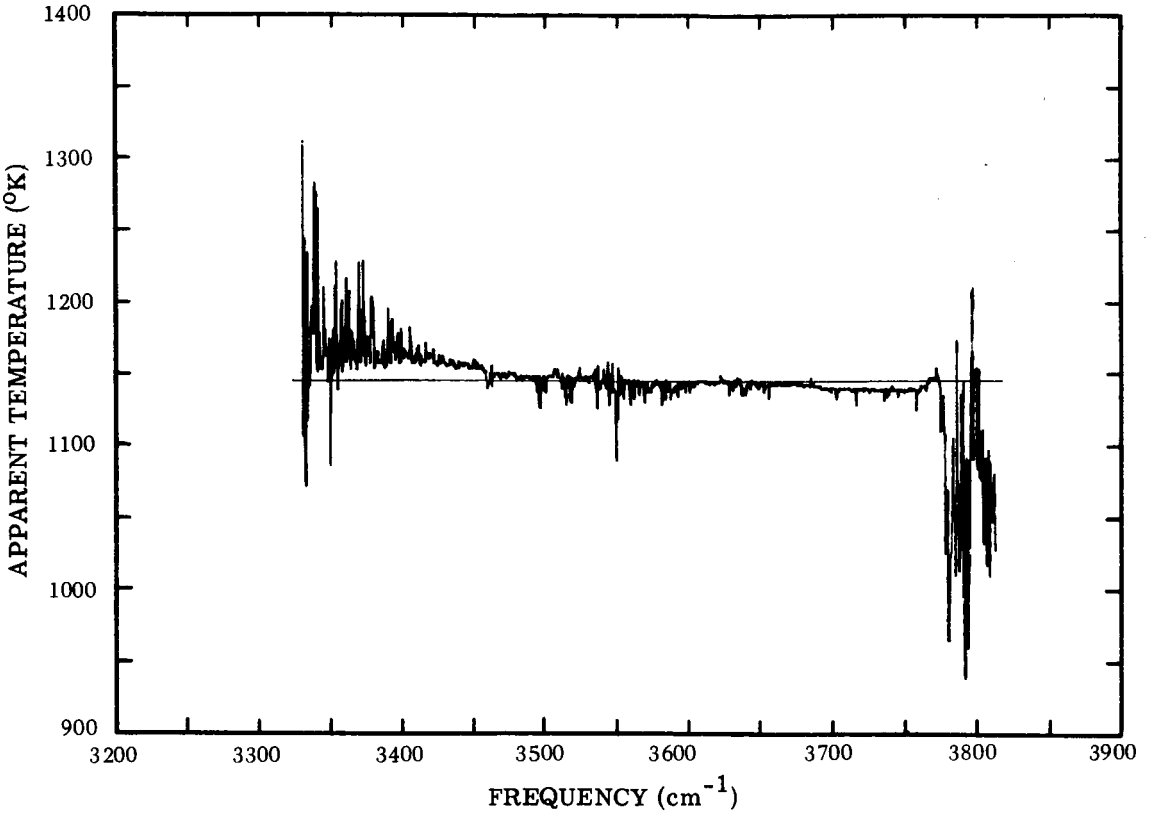

(c) Apparent Temperature vs. Frequency

FIGURE 6. COMPARISON OF ISOTHERMAL CO_2 SPECTRA WITH BAND-MODEL CALCULATIONS (RUN 10216803) (Concluded)

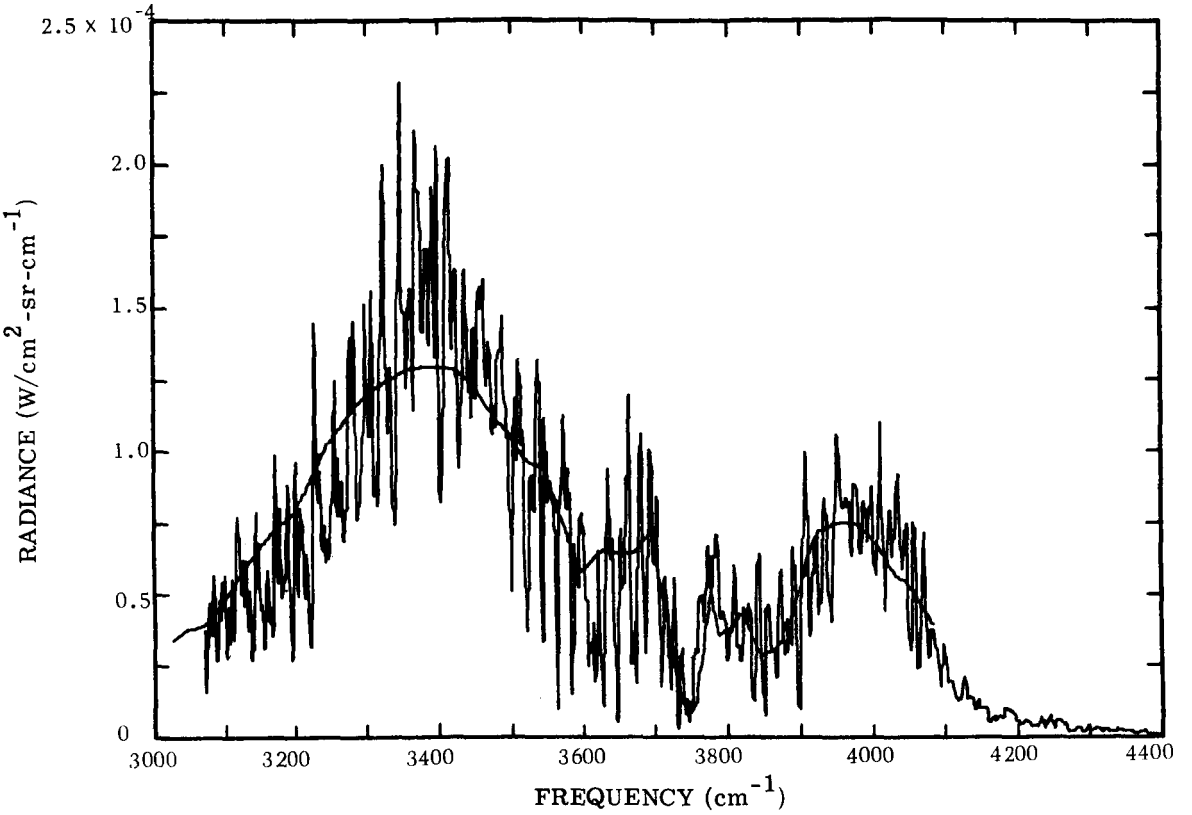

(a) Radiance vs. Frequency

FIGURE 7. COMPARISON OF NONISOTHERMAL H_2O SPECTRA WITH BAND-MODEL CALCULATIONS (RUN 10216811)

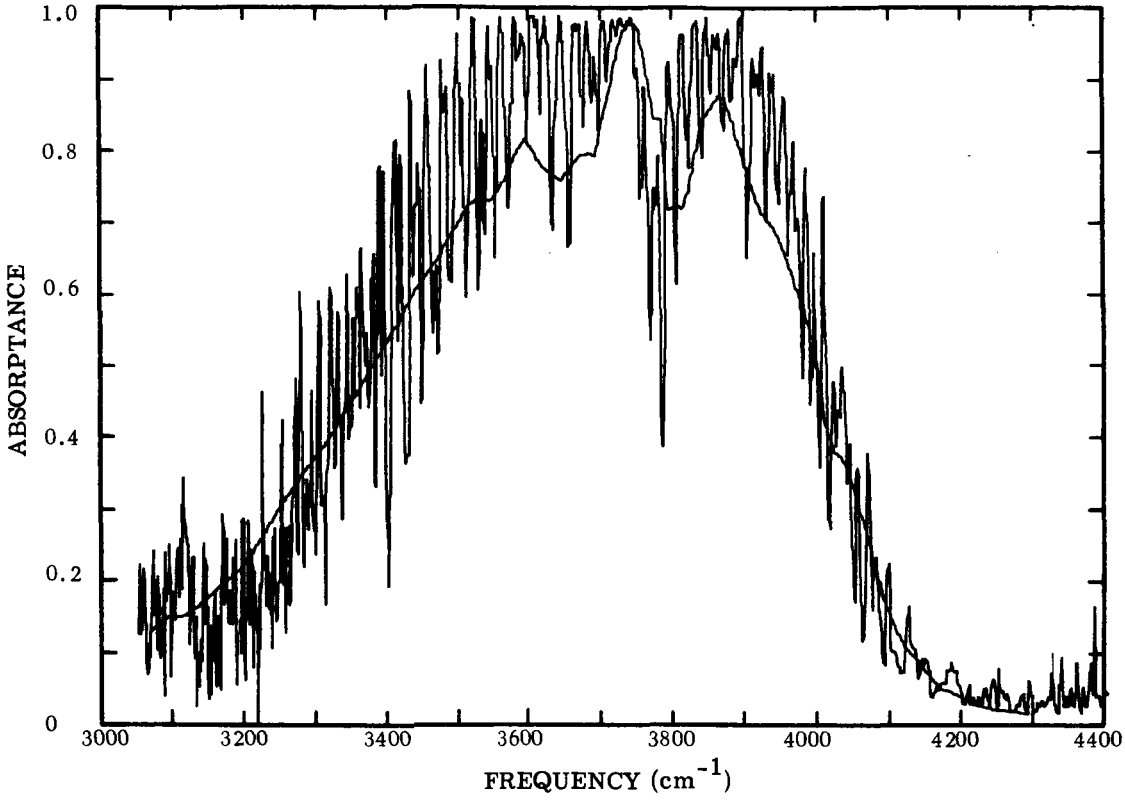

(b) Absorptance vs. Frequency

FIGURE 7. COMPARISON OF NONISOTHERMAL H_2O SPECTRA WITH BAND-MODEL CALCULATIONS (RUN 10216811) (Continued)

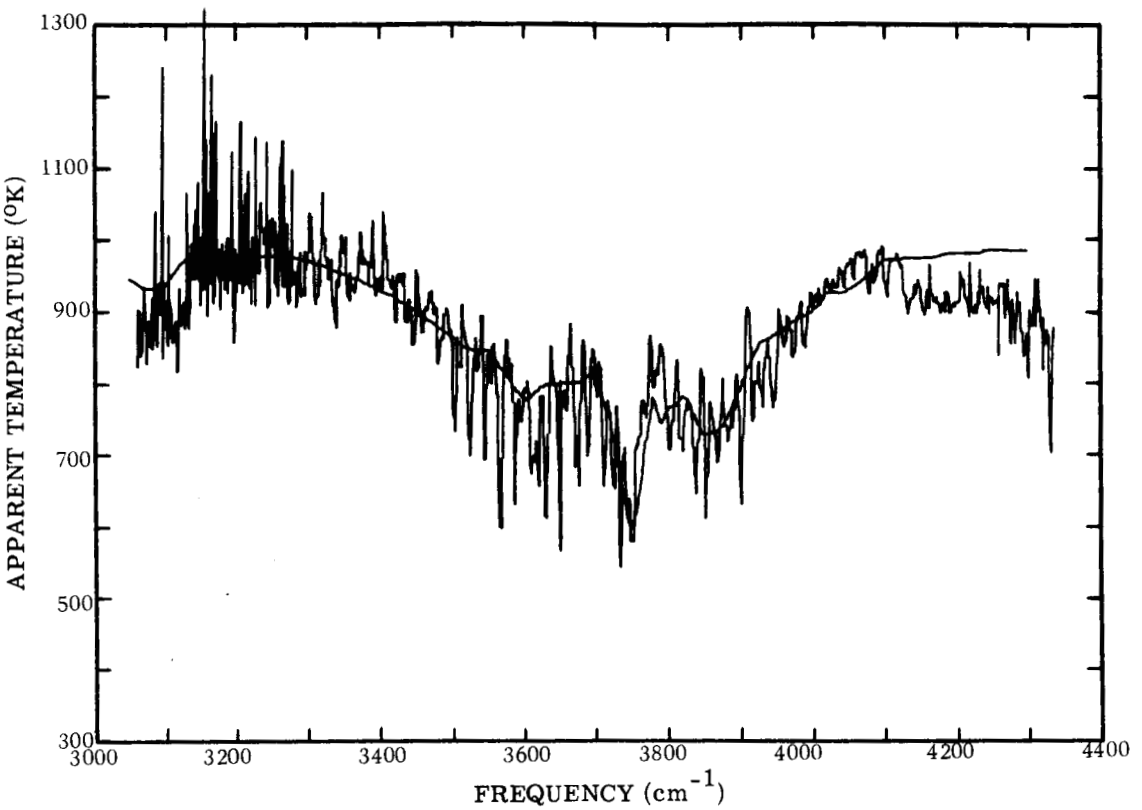

(c) Apparent Temperature vs. Frequency

FIGURE 7. COMPARISON OF NONISOTHERMAL H_2O SPECTRA WITH BAND-MODEL CALCULATIONS (RUN 10216811) (Concluded)

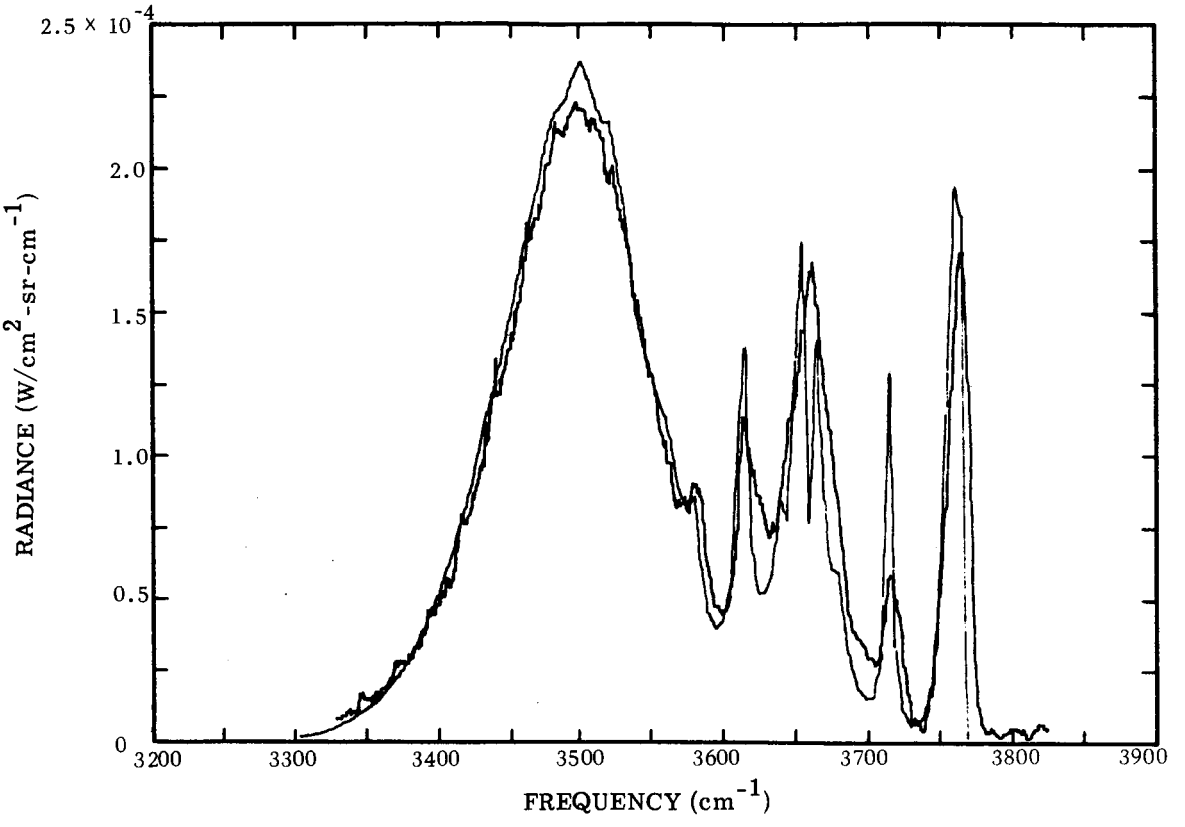

(a) Radiance vs. Frequency

FIGURE 8. COMPARISON OF NONISOTHERMAL CO_2 SPECTRA WITH BAND-MODEL CALCULATIONS (RUN 10216812)

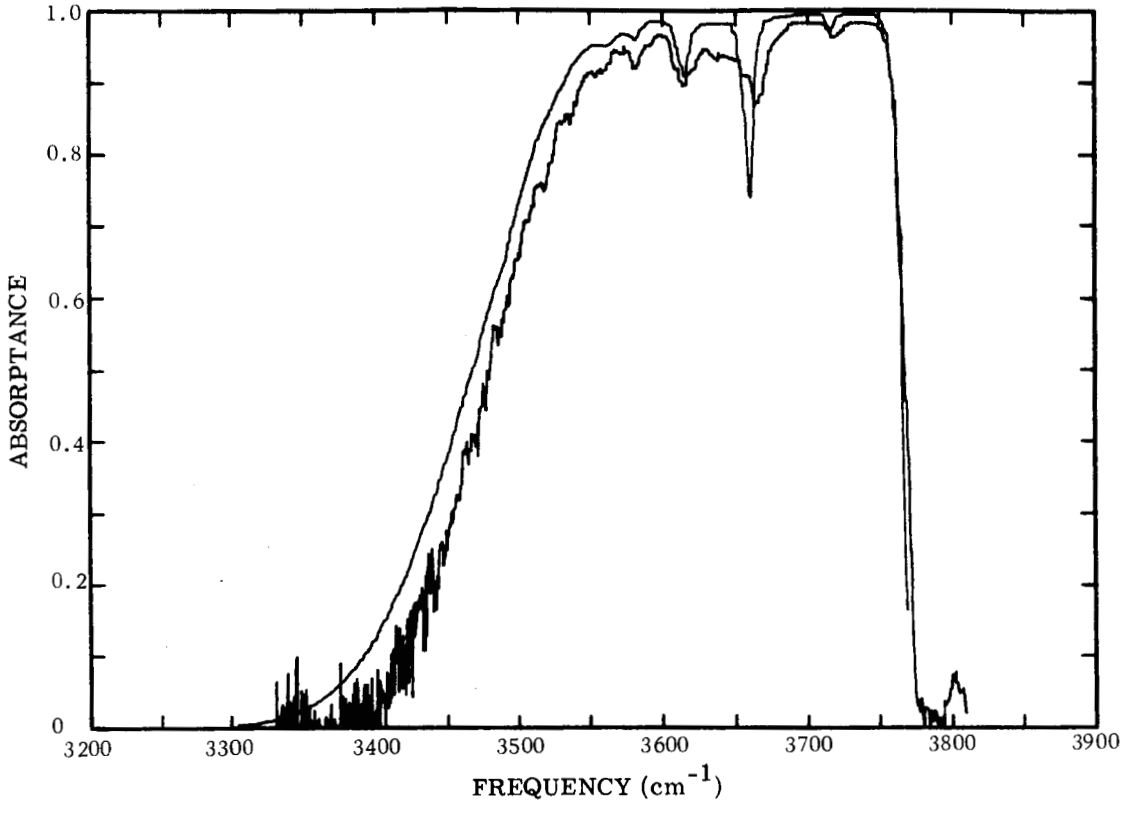

(b) Absorptance vs. Frequency

FIGURE 8. COMPARISON OF NONISOTHERMAL CO_2 SPECTRA WITH BAND-MODEL CALCULATIONS (RUN 10216812) (Continued)

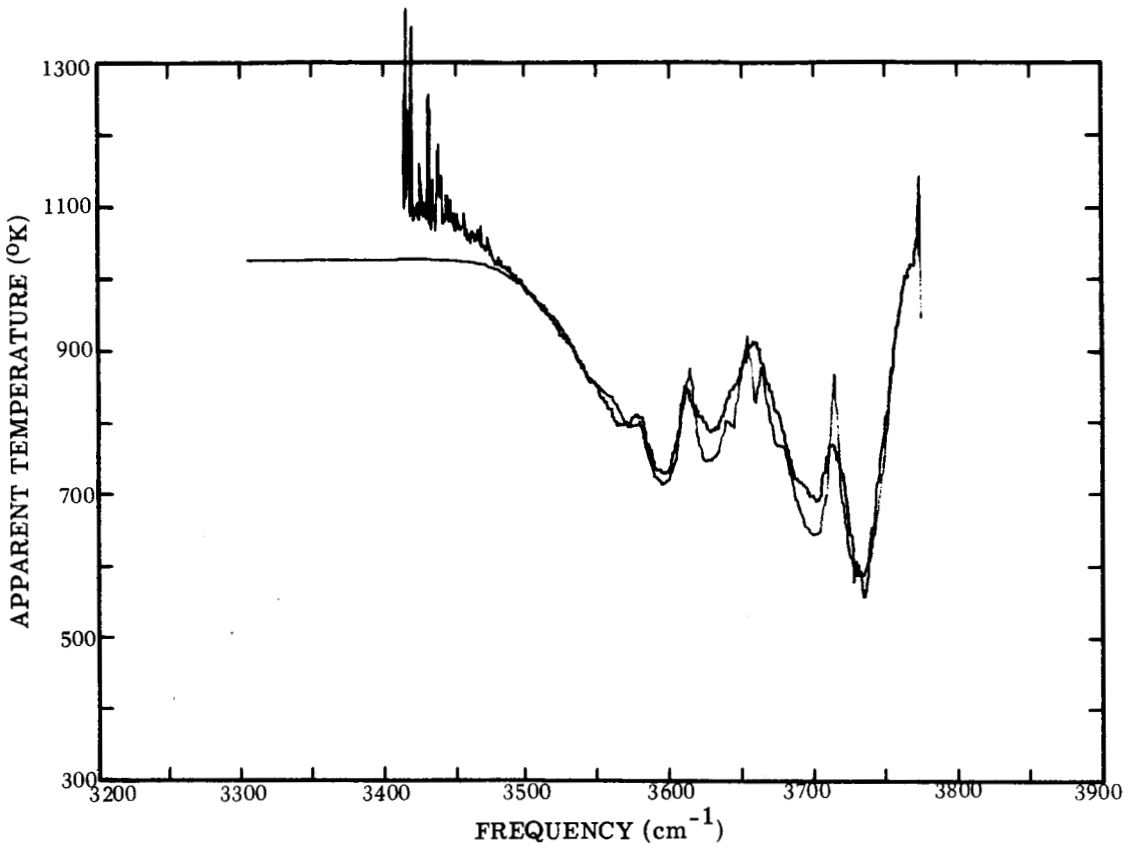

(c) Apparent Temperature vs. Frequency

FIGURE 8. COMPARISON OF NONISOTHERMAL CO_2 SPECTRA WITH BAND-MODEL CALCULATIONS (RUN 10216812) (Concluded)

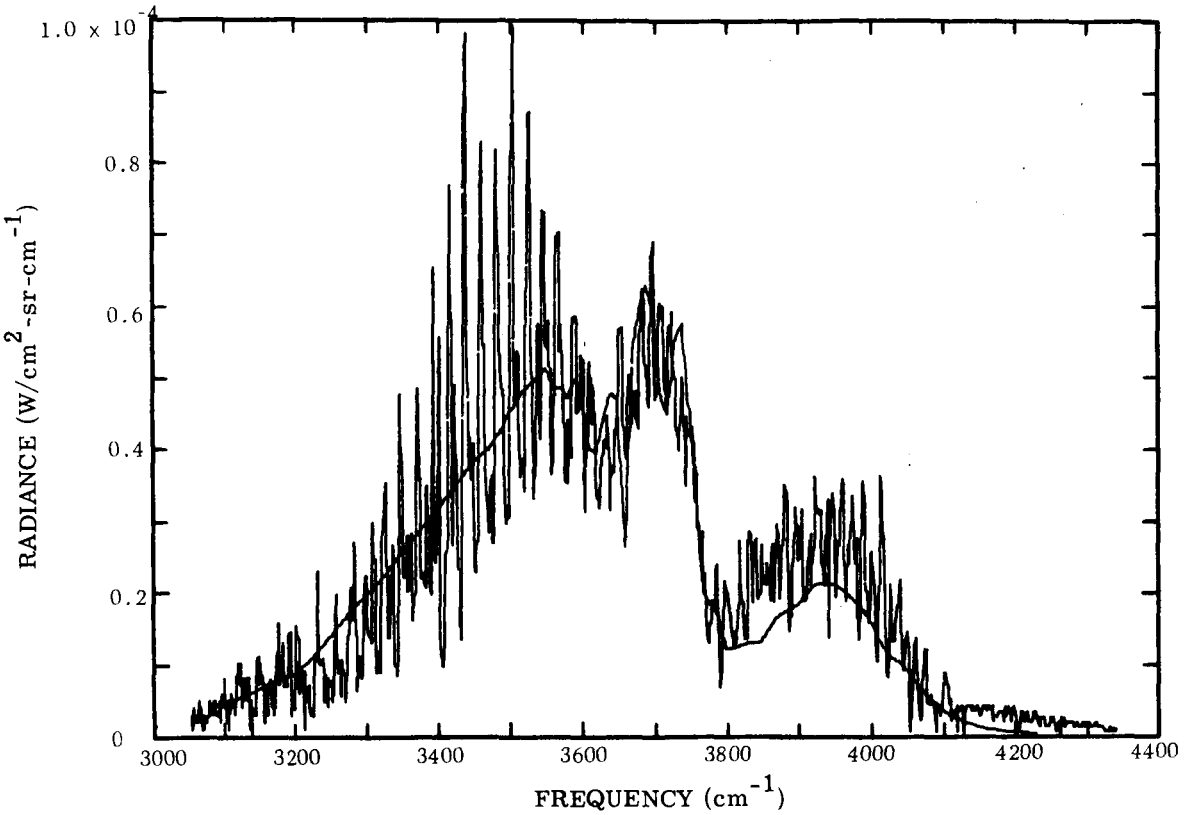

(a) Radiance vs. Frequency

FIGURE 9. COMPARISON OF NONISOTHERMAL $H_2O/CO_2/N_2$ SPECTRA WITH BAND-MODEL CALCULATIONS (RUN 10216807)

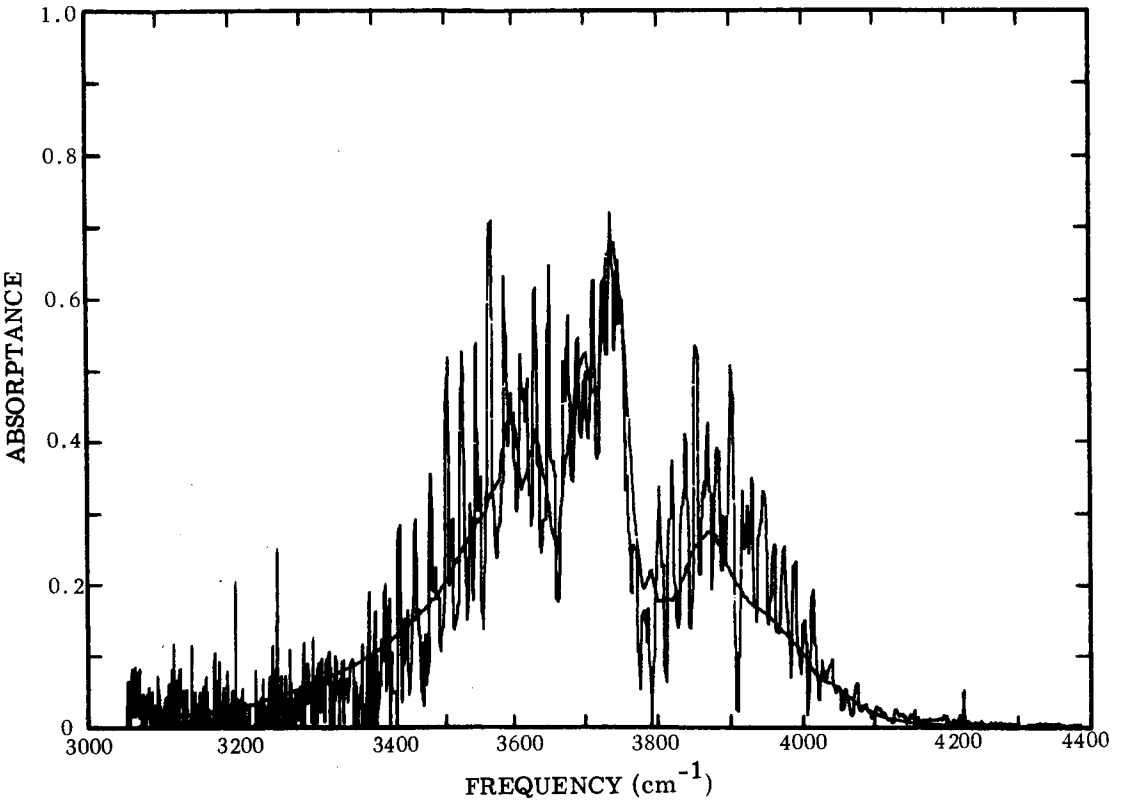

(b) Absorptance vs. Frequency

FIGURE 9. COMPARISON OF NONISOTHERMAL $H_2O/CO_2/N_2$ SPECTRA WITH BAND-MODEL CALCULATIONS (RUN 10216807) (Continued)

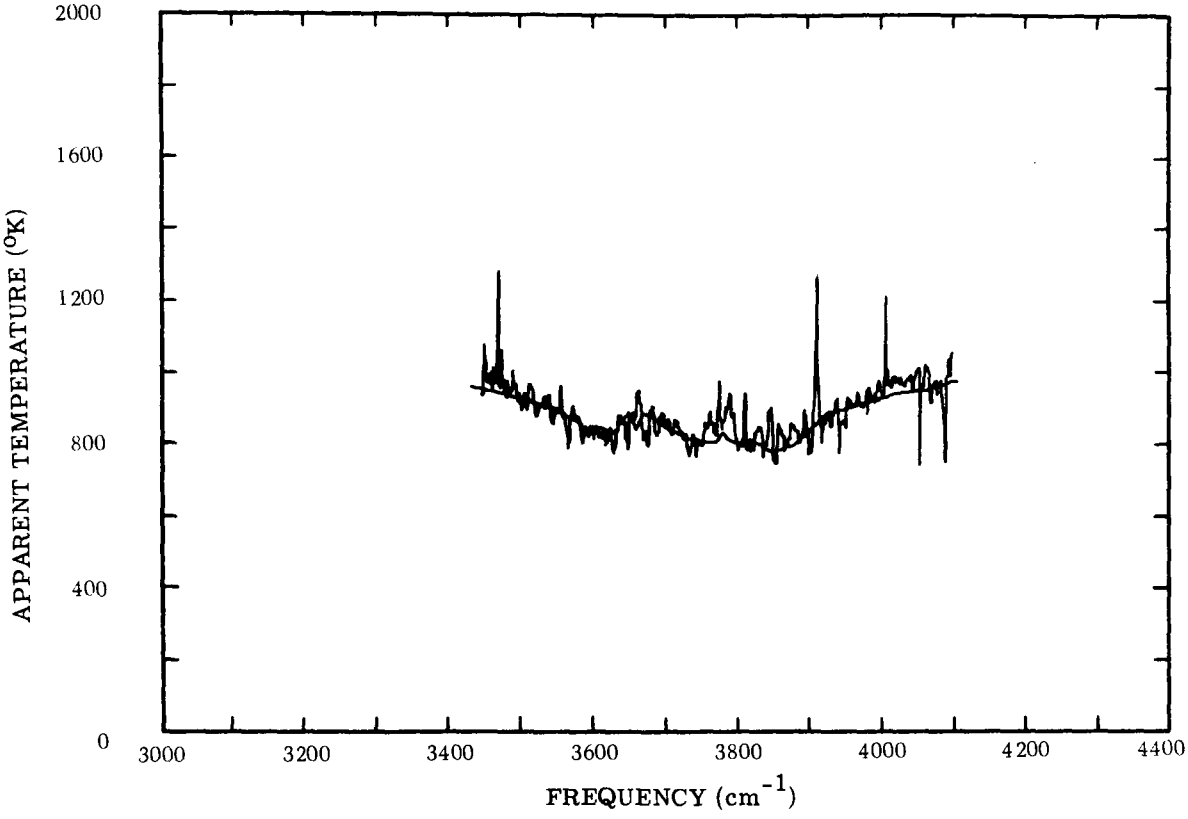

(c) Apparent Temperature vs. Frequency

FIGURE 9. COMPARISON OF NONISOTHERMAL $H_2O/CO_2/N_2$ SPECTRA WITH BAND-MODEL CALCULATIONS (RUN 10216807) (Concluded)

of the lines, total radiances and equivalent widths could not be readily evaluated from the observed spectra. Hence, comparisons were made only of the apparent temperatures, representing the ratio of observed peak radiances and absorptances, thus obviating the need for measuring areas under lines and estimating corrections for overlapping. Typical results are shown in figure 10, in which apparent temperatures are plotted against a generalized rotational quantum number for the $v = 0 \rightleftharpoons 1$ and $v = 1 \rightleftharpoons 2$ bands of HF, where the number designates vibrational state.

Figures 6 through 10 are indicative of the accuracy to which spectra can be calculated using the currently available knowledge of molecular band-model parameters (or in the case of HF the knowledge of the line strengths and widths). There are a number of anomalies in the band-model calculations which must be attributed to errors in the tabulations of the parameters. The most obvious of these is the glaring feature near 3660 cm^{-1} in the isothermal CO_2 spectra (fig. 6); it is not quite so evident but also present in the nonisothermal CO_2 spectra (fig. 8). It would, of course, be a simple matter to insert an appropriate false value into the tabulations in lieu of a reevaluation using original absorptance spectra. However, for the present study, no particular purpose would have been served by correcting these errors, which were simply ignored in the following analyses.

3.4. TEMPERATURE PROFILE DETERMINATIONS

In this investigation it was found to be more convenient to work with plots of apparent temperature vs. absorptance rather than vs. wavelength for successive comparisons of band-model predictions based on temperature-profile models. This result was consistent with the conclusion reached in an earlier study of H_2-F_2 flames [34], in which the final comparisons of theory and experiment were made in terms of apparent temperature vs. rotational quantum number. The convenience obtains from the rather simple shape of such plots, which were all quite similar. Physically, this similarity is easy to understand. At lower values of absorptance (or higher rotational quantum numbers for the case of HF), the hot gas is much more transparent, and the apparent temperature will approach a constant value corresponding to the optically thin gas and representing the average radiance along the entire optical paths. Conversely, as the absorptance approaches unity, the apparent temperature should approach the value corresponding to radiances at the near boundary, and in the limit would reach the actual temperature at that location. Thus, regardless of the shape of the actual profile, one would expect all the curves of apparent temperature vs. absorptance to be much alike and that, for a particular profile, the value of T^* should be a function mainly of absorptance and not very dependent on wavelength.

Using these curves of apparent temperatures vs. absorptance, temperature profiles were determined for the H_2O and CO_2 runs by successive calculations with the band-model program.

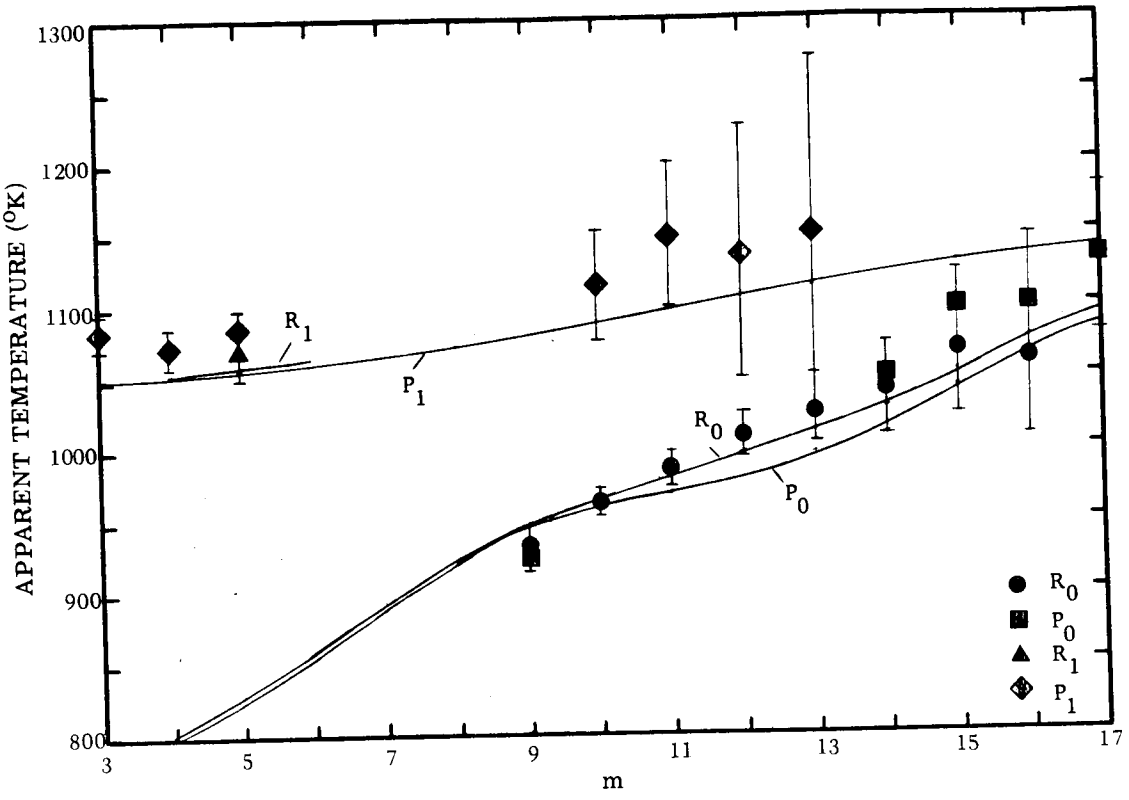

FIGURE 10. COMPARISON OF NONISOTHERMAL HF SPECTRUM WITH ISOLATED-LINE CALCULATIONS (RUN 12056804). R and P are branch designations.

Since this was an exploratory study, the parameters characterizing the temperature profiles were adjusted in simple sequences until a best fit between calculations and observations was obtained. This procedure is illustrated in complete detail in appendix D. The results of these inversions are shown in figures 11 through 17, in which the inferred temperature profiles are compared with the values measured directly by the thermocouples, as indicated by the crosses.

A variety of options were exercised in regard to the specification of the number of parameters characterizing the temperature profile. For example, linear and symmetrical triangular profiles can always be characterized by two parameters, the maximum and minimum temperatures. However, if one has the further constraint that the lower temperature is known, then these profiles can be characterized by only one parameter. Similarly, the number of parameters for the other profiles can vary; in the case of the truncated triangle, the width of the isothermal region at the higher temperature can be included as a parameter, or taken to be a known fixed value implicit in the a priori knowledge of the shape of the profile. Such specifications are not as arbitrary as they might seem at first glance. In many practical applications involving propulsion devices, the geometry of the system will clearly indicate the location and extent of temperature maxima and minima, and the lower temperature at the boundary of the gas stream can be related to a value easily measured on a duct or exhaust nozzle wall.

The corresponding comparisons of deduced and observed temperature profiles for the HF runs are shown in figures 18 through 22. For these comparisons, the profile models were again taken to consist of linear segments. However, in these runs, the shapes of actual profiles imposed on the sample were not so well approximated by linear segments as they would have been by curves consisting of parabolic segments. Figure 23 shows the results for a single maximum profile approximated with a parabola specified by one or two parameters.

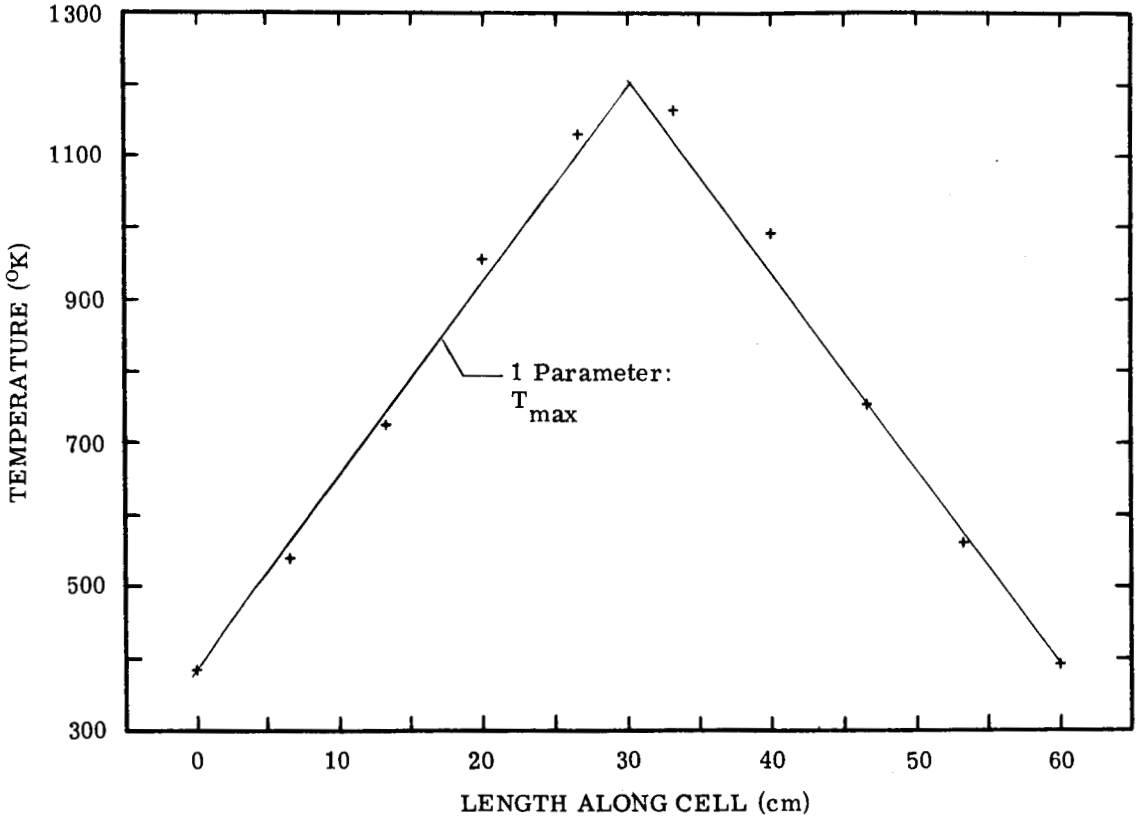

FIGURE 11. TEMPERATURE PROFILES EXTRACTED FROM EMISSION AND ABSORPTION SPECTRA (RUN 10216811)

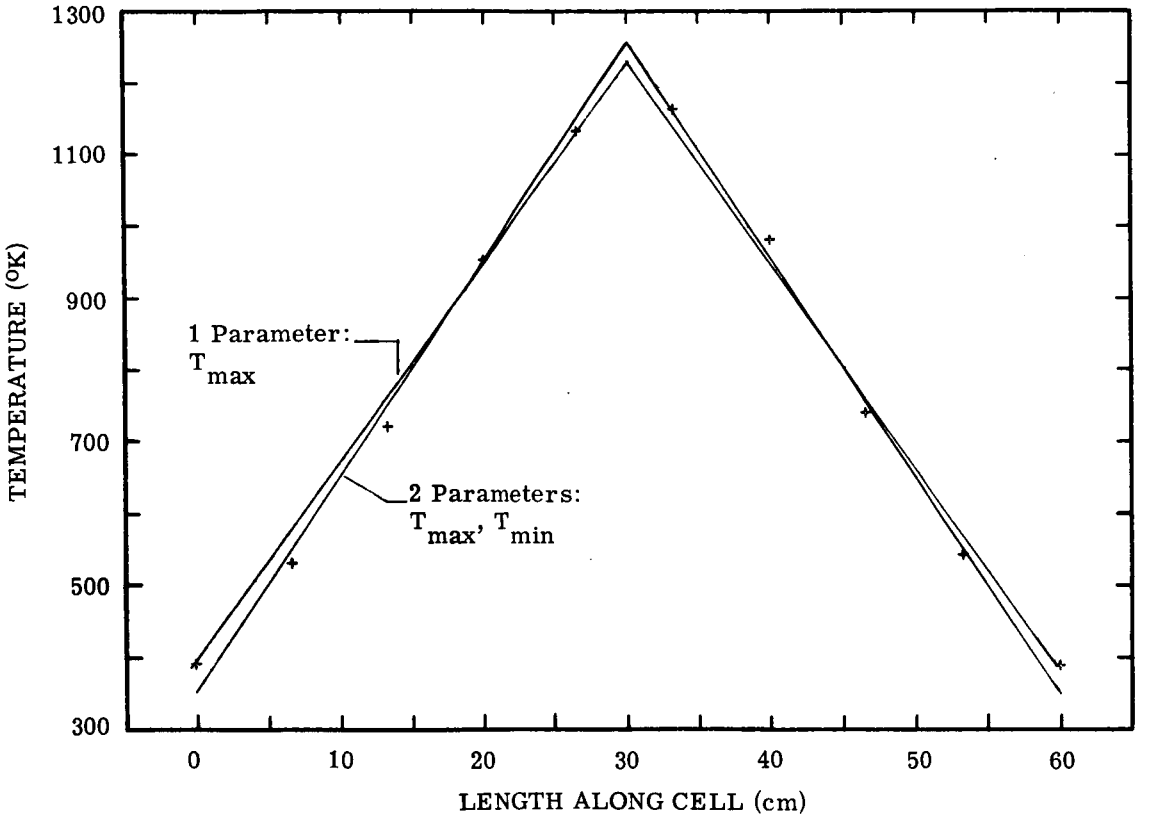

FIGURE 12. TEMPERATURE PROFILES EXTRACTED FROM EMISSION AND ABSORPTION SPECTRA (RUN 10216812)

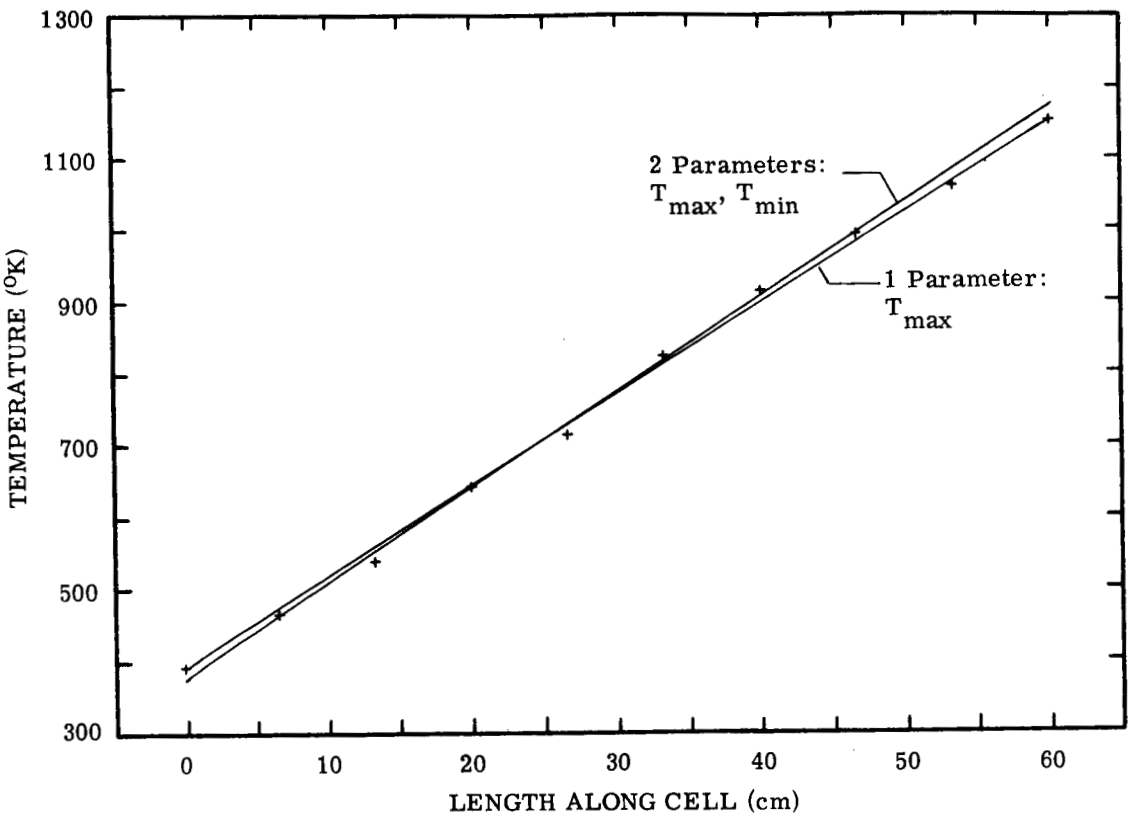

FIGURE 13. TEMPERATURE PROFILES EXTRACTED FROM EMISSION AND ABSORPTION SPECTRA (RUN 10246808)

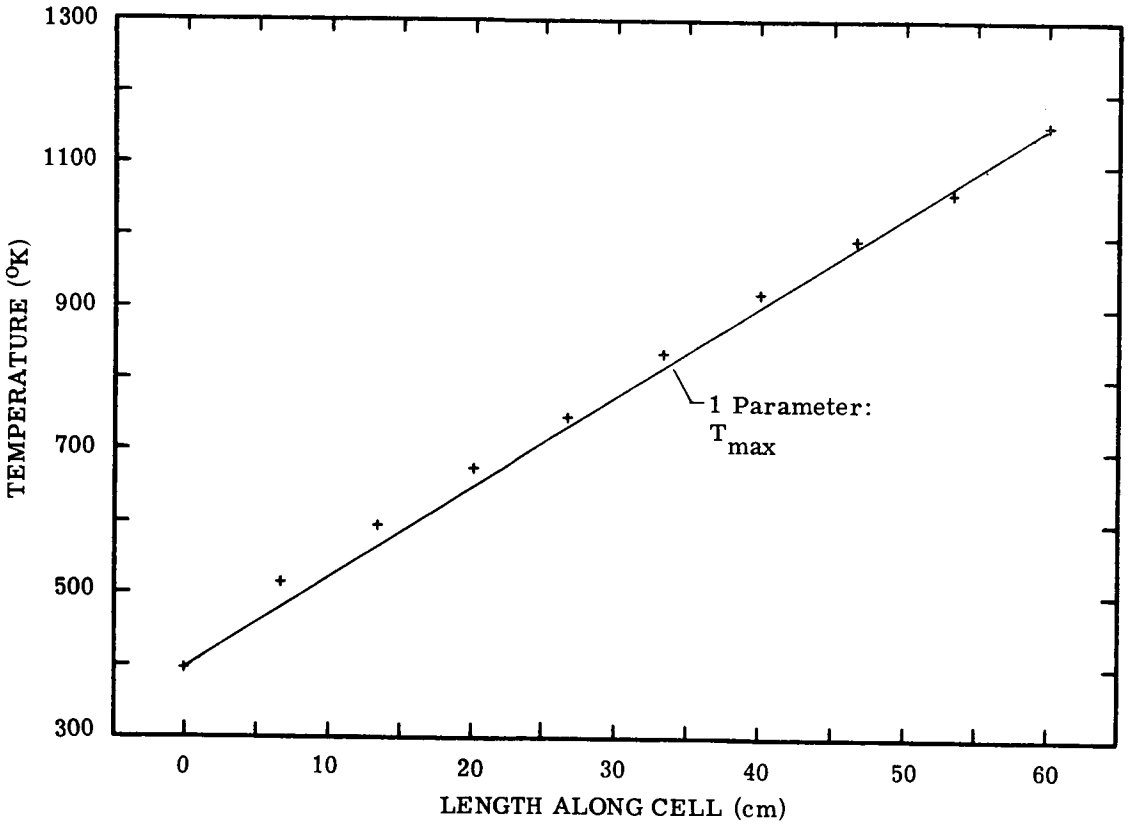

FIGURE 14. TEMPERATURE PROFILES EXTRACTED FROM EMISSION AND ABSORPTION SPECTRA (RUN 10246813)

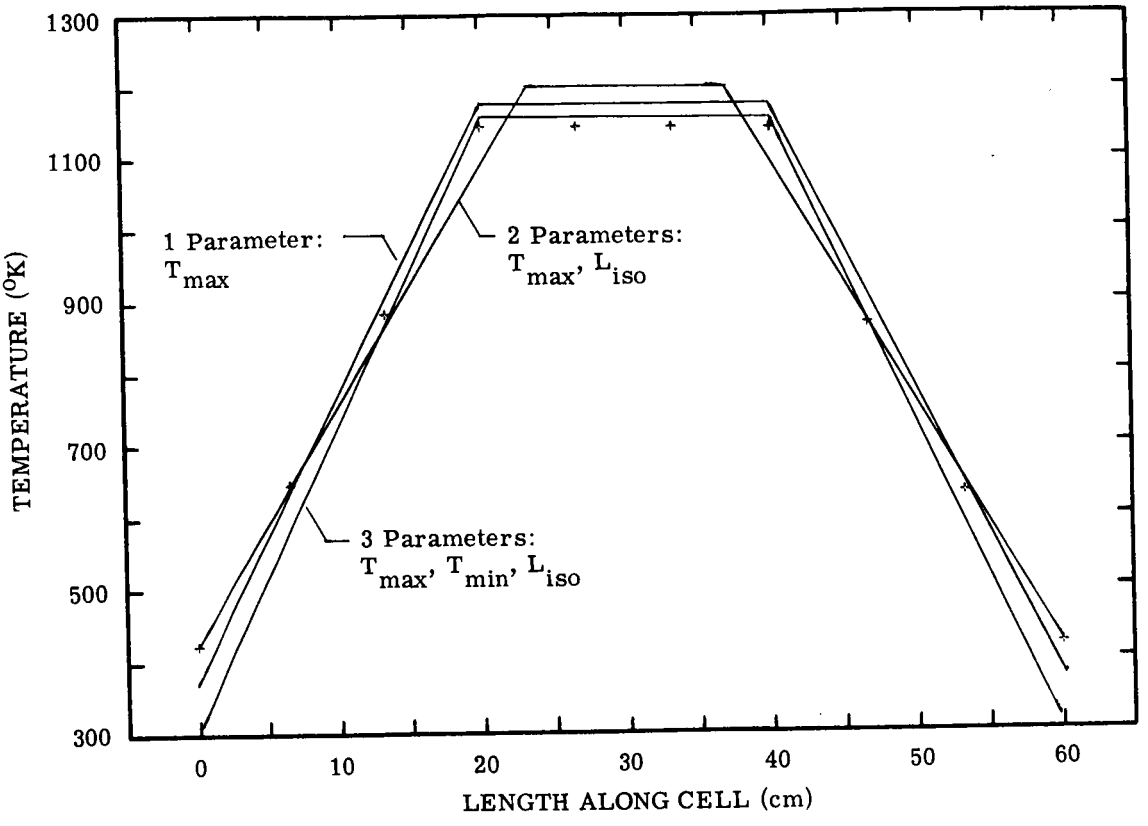

FIGURE 15. TEMPERATURE PROFILES EXTRACTED FROM EMISSION AND ABSORPTION SPECTRA (RUN 10286811)

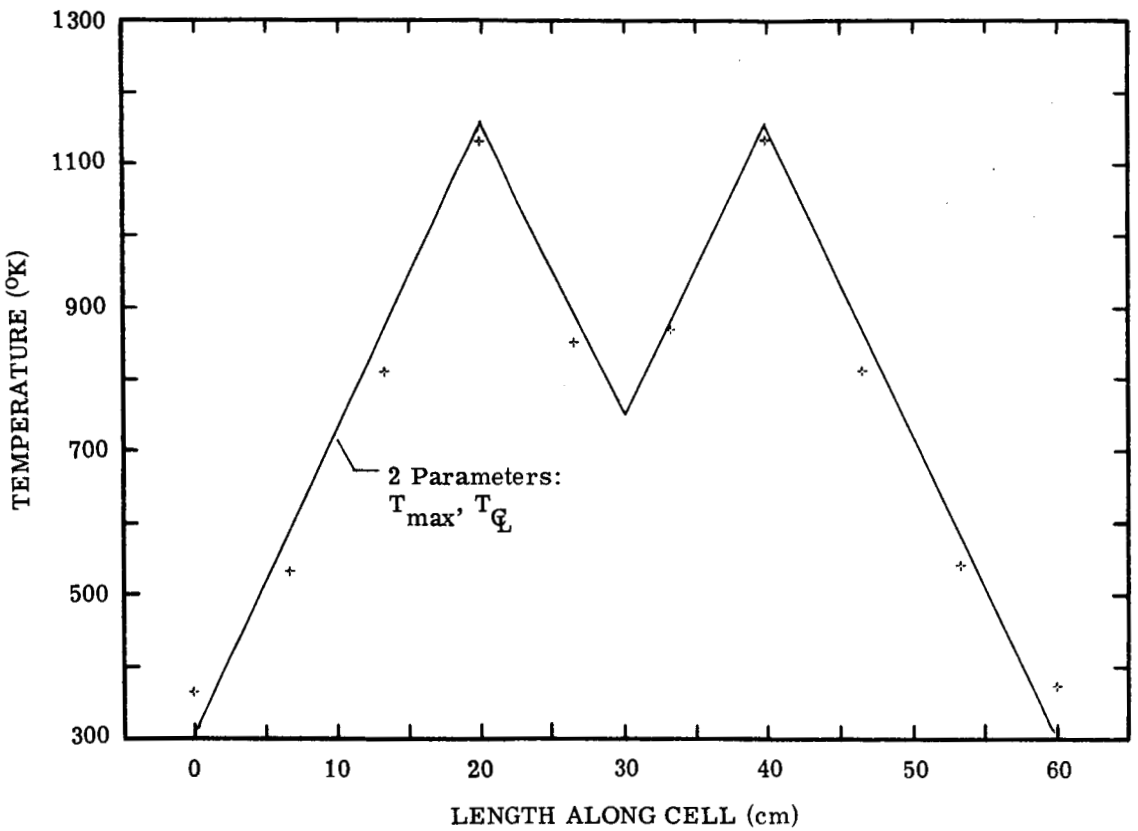

FIGURE 16. TEMPERATURE PROFILES EXTRACTED FROM EMISSION AND ABSORPTION SPECTRA (RUN 10286816)

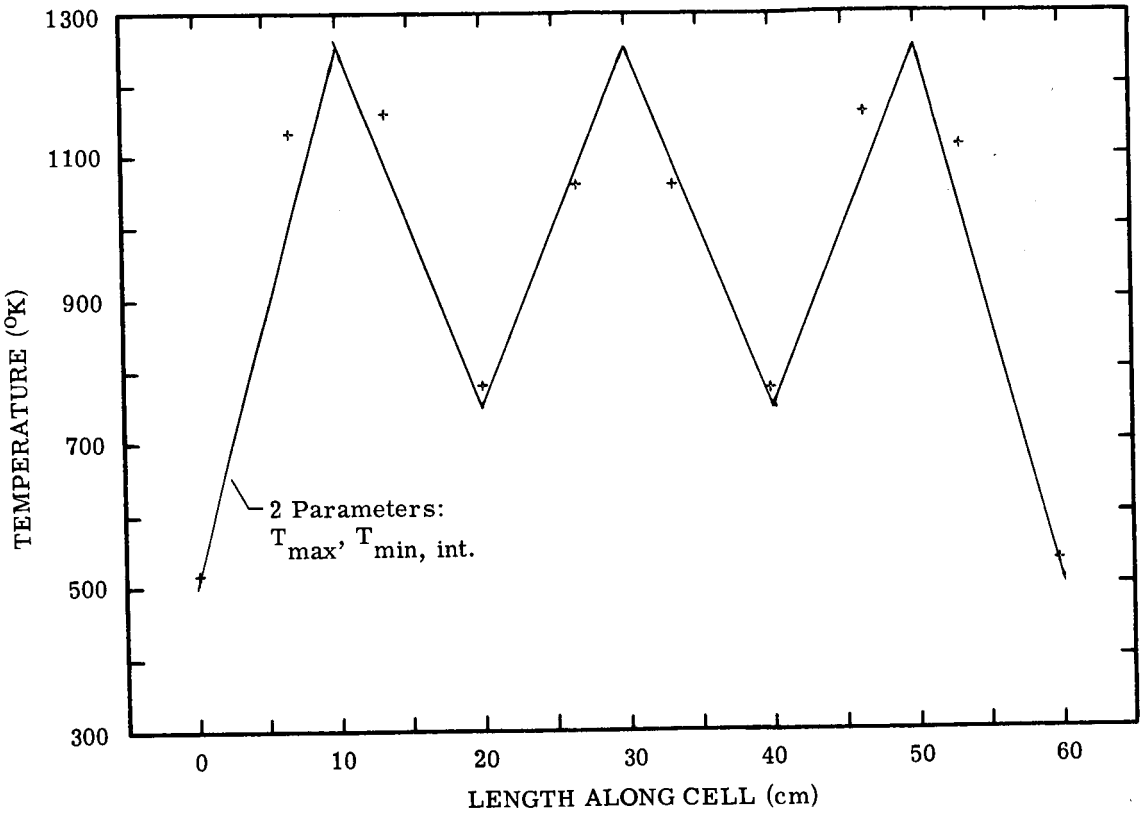

FIGURE 17. TEMPERATURE PROFILES EXTRACTED FROM EMISSION AND ABSORPTION SPECTRA (RUN 10286821)

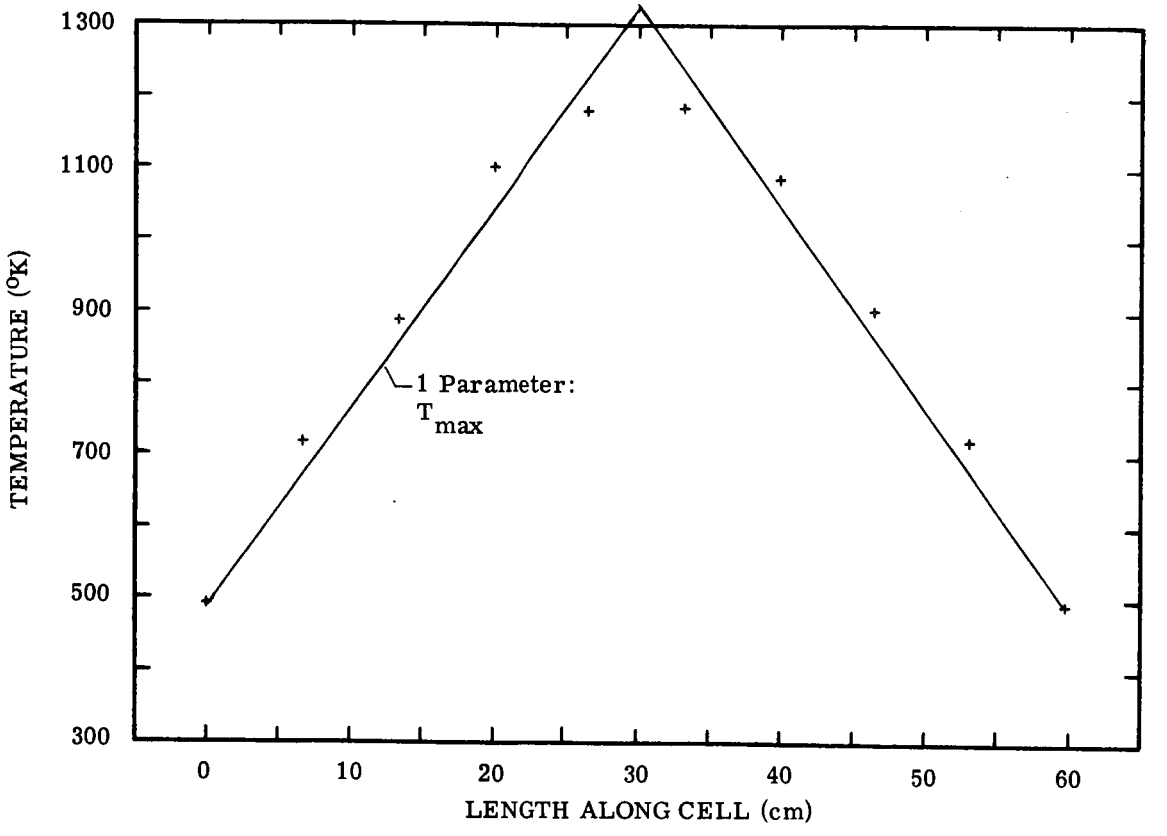

FIGURE 18. TEMPERATURE PROFILES EXTRACTED FROM EMISSION AND ABSORPTION SPECTRA (RUN 12056804)

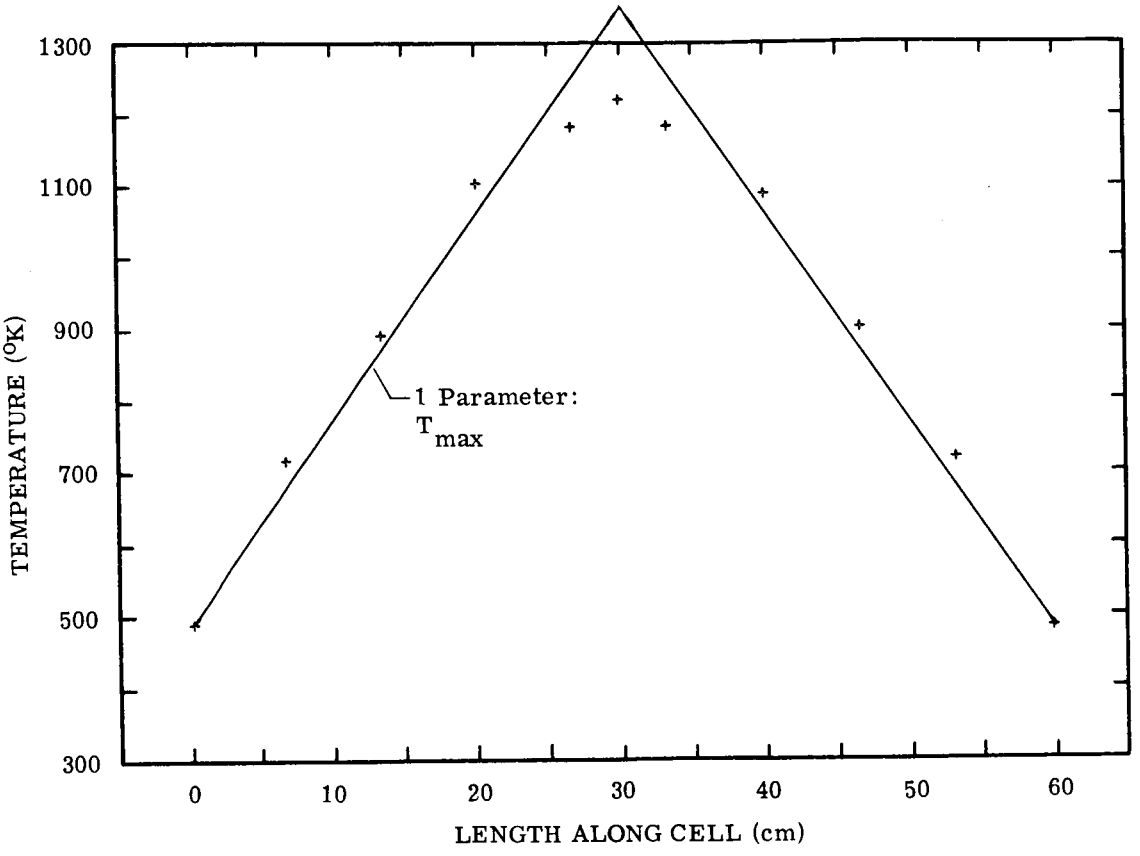

FIGURE 19. TEMPERATURE PROFILES EXTRACTED FROM EMISSION AND ABSORPTION SPECTRA (RUN 12056808)

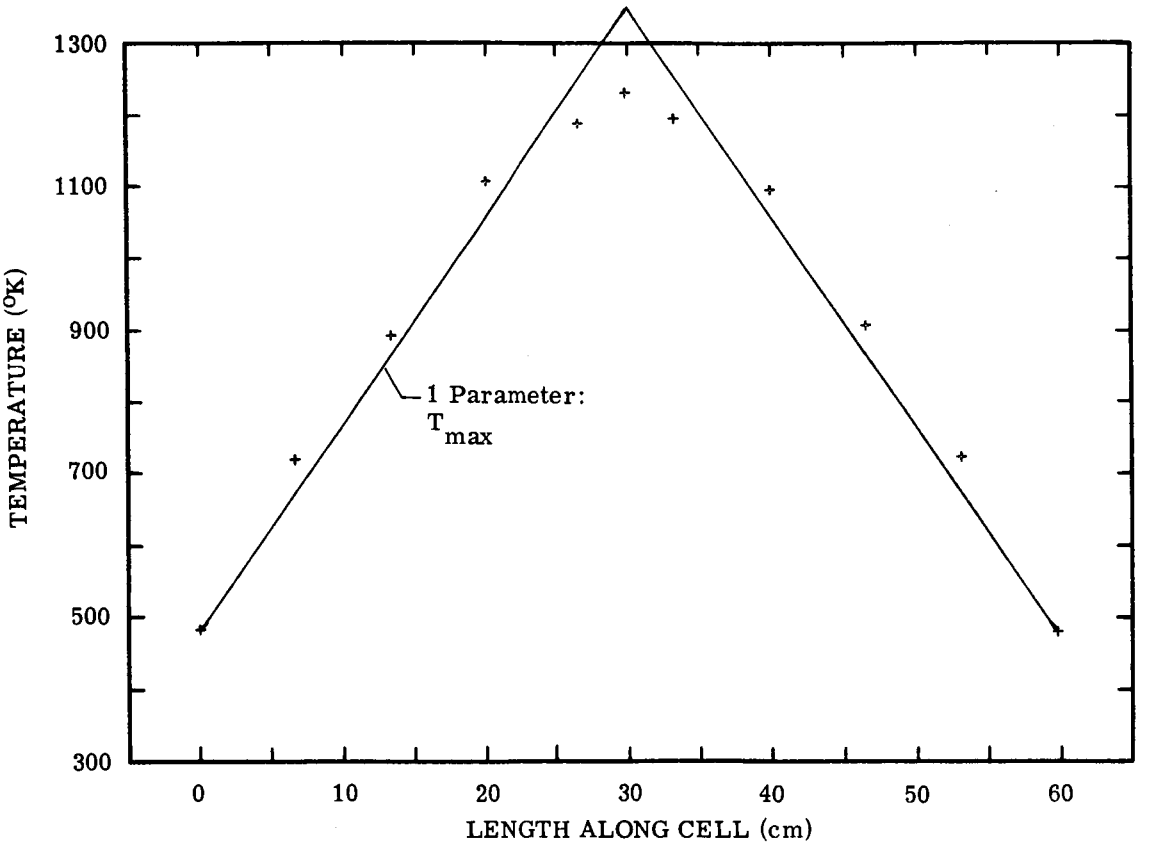

FIGURE 20. TEMPERATURE PROFILES EXTRACTED FROM EMISSION AND ABSORPTION SPECTRA (RUN 12056812)

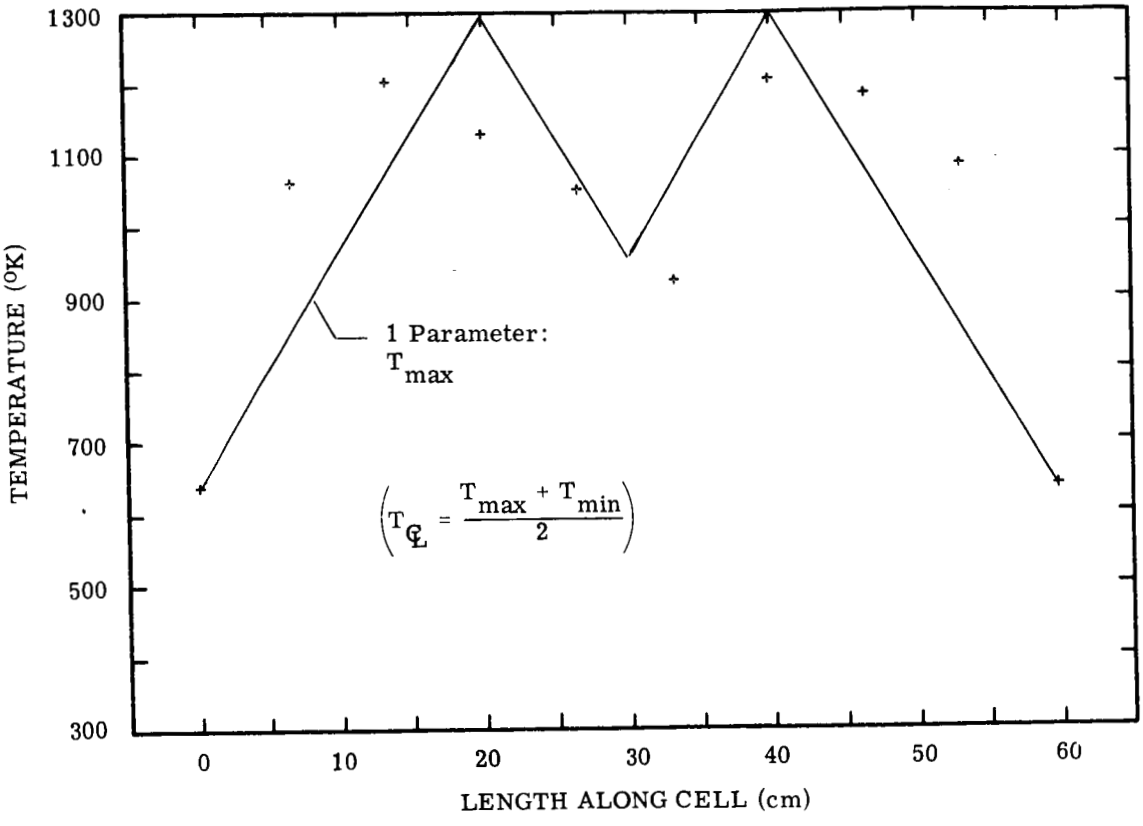

FIGURE 21. TEMPERATURE PROFILES EXTRACTED FROM EMISSION AND ABSORPTION SPECTRA (RUN 12276804)

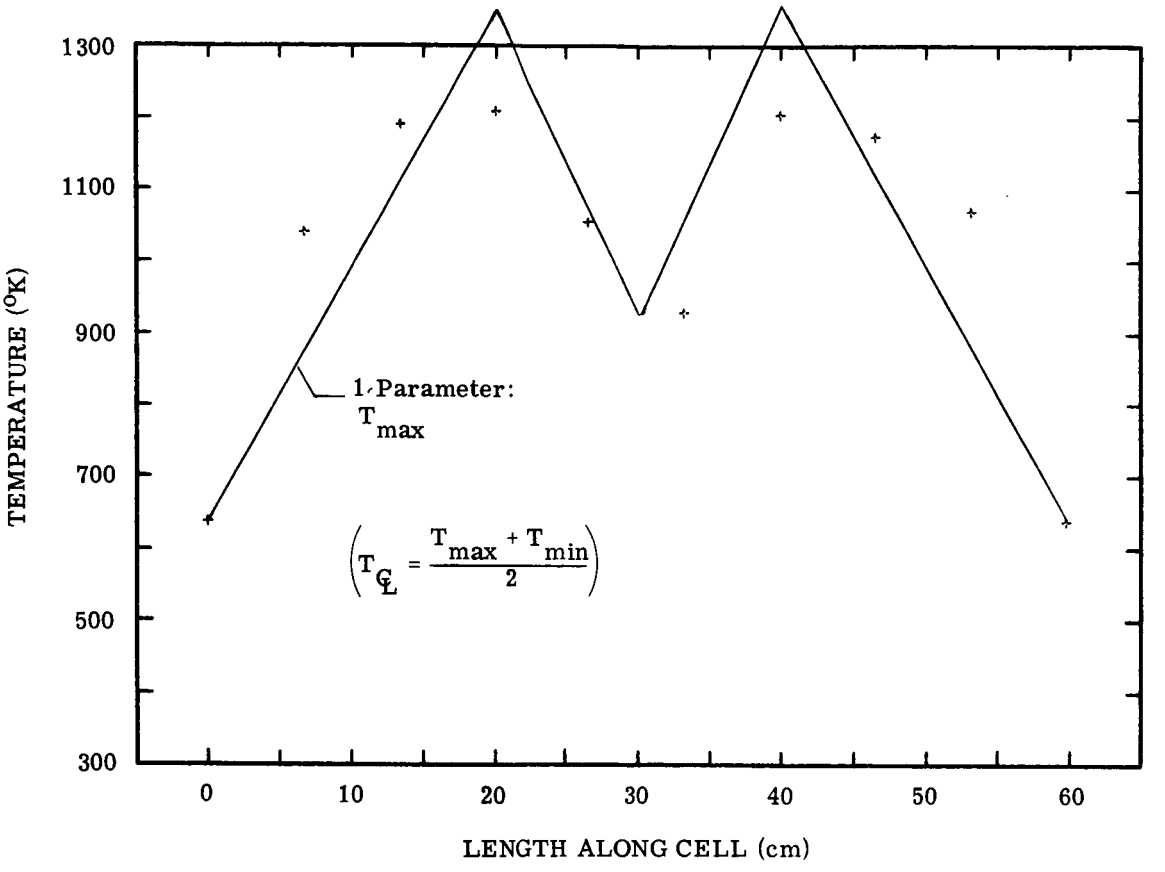

FIGURE 22. TEMPERATURE PROFILES EXTRACTED FROM EMISSION AND ABSORPTION SPECTRA (RUN 12276807)

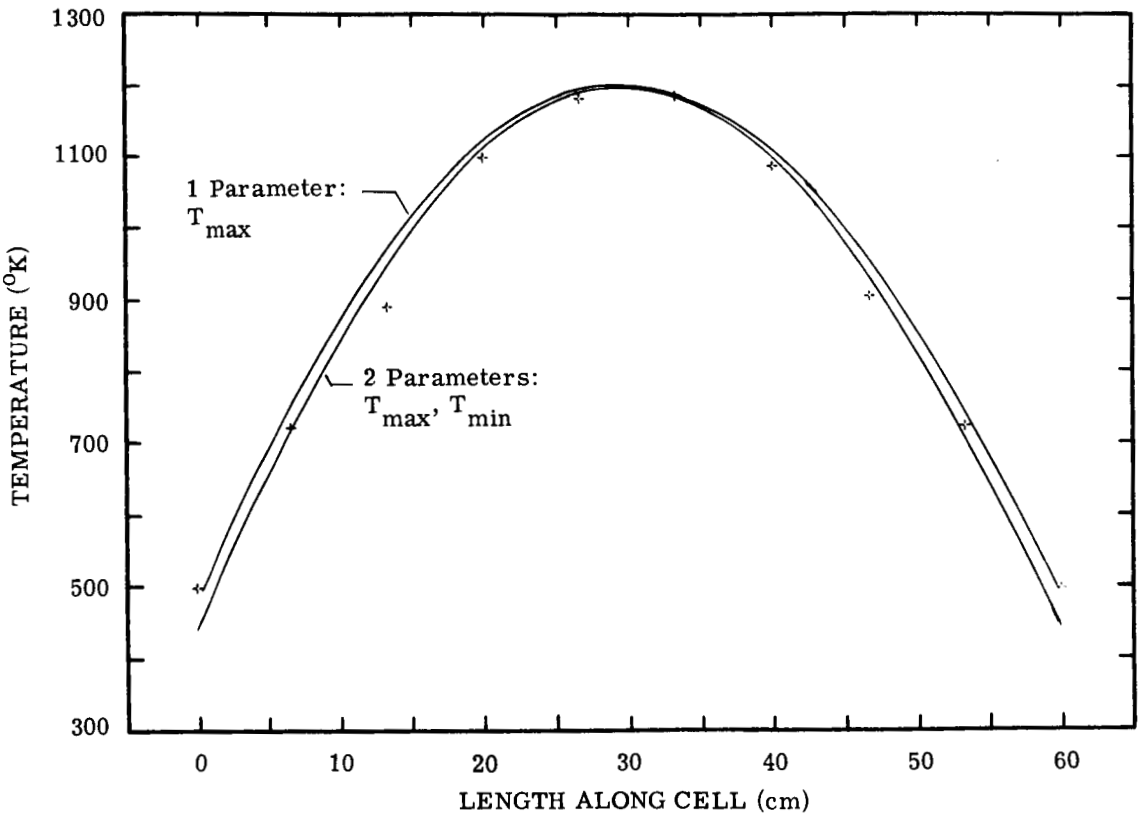

FIGURE 23. TEMPERATURE PROFILES USING PARABOLAS EXTRACTED FROM EMISSION AND ABSORPTION SPECTRA (RUN 12056804)

4
DISCUSSION OF RESULTS

The results of this investigation, as presented in the comparisons of the temperature profiles deduced from the emission and absorption spectra with the directly measured profiles (figs. 13 through 23), clearly validate the present approach in the application of infrared emission-absorption spectroscopy to temperature-profile determination. In all cases the agreement between the inferred and the directly measured temperature profiles was satisfactory in view of the quality and quantity of the information available on the spectral properties of the emitting and absorbing gases, the experimental errors in the measurements of temperatures and radiances, and the representation of the temperature profiles by linear segments. The principal conclusion to be drawn from this work, therefore, is that infrared emission-absorption spectroscopy offers considerable promise as a means for determining temperature profiles in nonisothermal radiating gases. However, further development of this approach would be requisite to the successful extension of the method from the controlled conditions in the furnace-heated cell in the present study to those encountered in the testing of full-size engines. Along these lines, it would be especially appropriate to apply it to an intermediate case of a nonisothermal source created in an appropriate combustion apparatus in the laboratory, in which the temperature profiles could be independently determined.

Further analyses of the mathematical methods for inversion of spectra might also be in order. In this regard it could be expected that the problem of nonuniqueness of the solutions could largely be avoided in an approach which could be characterized as intermediate between the method of the present study based on successive calculations using a profile model, and true inversion calculations which assume no knowledge whatsoever of the profile. One approach would be an inversion calculation involving a trial solution based on a priori knowledge of the shape of the profile, with numerical values obtained by the present method. Another approach, applicable to axisymmetric flow fields, would be to deduce the general shape of the temperature profiles from transverse spatial scans at particular frequencies, thus providing the initial guesses for the inversion. In order to assess the advantages of one approach over another thoroughly, or the possible combination of the two, more complete experimental data representing a greater variety of temperature profiles would be required.

In considering the application of infrared spectroscopy to propulsion studies, it should be kept in mind that, for most combustion systems, the principal products which radiate in the infrared are CO_2 and H_2O, which are also present in the atmosphere. In the present experiment,

the optical path outside of the sample cell was thoroughly flushed with dry nitrogen to eliminate the atmospheric absorption. However, it is not always possible to do this with an instrument viewing a jet or rocket engine; an unflushed path of even a few centimeters will result in appreciable absorption which must be taken into account. The method for doing this is straightforward; the radiative-transfer calculation is simply set up for the entire optical path, not just that through the hot gas stream.

The ultimate accuracy of the temperature profiles deduced by emission-absorption spectroscopy is difficult to establish from the present results alone. Obviously, errors in the radiance and absorptance measurements could be further reduced by more meticulous attention to the calibration method. Using an optically dense charge of gas with a uniform temperature appears to be a preferable means of calibration rather than using a blackbody and evaluating corrections for mirror reflectance changes with wavelength. However, considerable improvement would result in the use of a windowless absorption cell to eliminate corrections for emission, absorption, and reflection by the window materials, the properties of which vary both with temperature and wavelength. Further accuracy could be gained through the use of a precision temperature controller to better equalize the temperatures along the length of the sample cell.

The use of a two-sided instrument is recommended; that is, the reference source for absorption should be located on the opposite side of the hot gas from the detector. One-sided systems utilizing a passive element on the far side of the hot gas, e.g., a flat or spherical mirror or a corner-cube reflector, offer some advantages: convenience in packaging an instrument for installation in a test cell, and, in the case of a corner-cube, resisting the effects of high-level acoustic environment. However, for the most precise measurements, this convenience would be outweighed by the difficulties accounting for the reflectance losses of the mirror, and in treating the more complex profile represented by the apparent doubling of the source.

Finally, the reliability of the inferred temperature profiles could be enhanced by the use of an appropriate calculation, programmed for a computer, for fitting the band-model predictions to the observed variation of apparent temperatures with absorptance.

5
SUMMARY OF RESULTS

Emission-absorption spectroscopy has been shown to provide a means for determining temperature profiles within bodies of hot gases which are nonuniform and optically dense in regions of molecular-band radiation. In review, the approach explored in the present study is based on the following premises.

1. Local thermodynamic equilibrium prevails throughout the gas.
2. The general character of the temperature and density profiles are known so that their shapes can be specified in terms of a very few parameters.
3. The spectral properties of the emitting-absorbing species are known. For polyatomic molecules, the required properties are two band-model parameters characterizing the positions, strengths, and spacings of the lines, as functions of frequency and temperature. For diatomic molecules exhibiting nonoverlapping lines, the alternative requirement is knowledge of line positions, and strengths and widths as functions of temperature.

The recommended procedure for deducing temperature profiles from emission and absorption spectra consists of:

1. Quantitative measurements of emission and absorption to yield values of spectral radiances and absorptances throughout a molecular band.
2. Evaluation of apparent temperature as a function of frequency from the ratio of the spectral radiances and absorptances.
3. Deduction of the temperature profile from the observed variation of apparent temperature, with absorptance (or rotational quantum number) by means of a best fit of band-model calculations (or isolated-line calculations) obtained by appropriately adjusting the profile-shape parameters.

This procedure has been shown to yield satisfactory agreement with direct measurements of temperature profiles of various shapes in water vapor, carbon dioxide, hydrogen fluoride, and a mixture of water vapor, carbon dioxide, and nitrogen.

Appendix A
DATA REDUCTION PROCEDURE

The raw data on the emission and absorption were processed by a digital computer to yield spectral radiances, absorptances, and apparent temperatures. In accordance with the requirements outlined in section 3 (Apparatus and Procedures), the computer program was set up to utilize emission-absorption measurements in an isothermal charge of CO_2 as the fundamental calibration source. Since the output of the instrument, as deflections on the chart recorder or voltages recorded on punched cards, was proportional to the radiance of the blackbody built into the spectrometer, it was necessary to deduce from the observed output of the isothermal CO_2 charge the effective radiation temperature of the blackbody. Furthermore, in order to account for the emission from the cell windows, an in situ measurement of the absorptance spectrum of the window at the operating temperature was a required part of the data collection.

Spectral data were gathered in an appropriate sequence.

1. Absorption, background (cell empty)
2. Absorption, isothermal (CO_2)
3. Absorption, nonisothermal (gas sample)
4. Emission, beam balance (cell empty)
5. Emission, window (cell empty)
6. Emission, isothermal (CO_2)
7. Emission, nonisothermal (gas sample)

In addition, zero energy levels were checked during each scan. Note that, in the absorption mode, the zero energy level represented full scale, whereas the zero absorptance was given by scan 1, the background scan with the cell empty. On the other hand, in the emission mode, zero energy level corresponded to zero radiance, whereas full scale corresponded to the effective radiance of the blackbody as given by scan 4. The two modes of operation are illustrated in figure A1, a schematic representation of the various scans.

The calculations proceeded stepwise as indicated below; the quantity D refers to the signal voltage i.e., the deflection on the chart recorder.

I. Isothermal Absorption

Input:

1. Absorption, zero, $D_{a,0}$
2. Absorption, background $D_{a,bk}$
3. Absorption, CO_2 sample, $D_{a,s}$

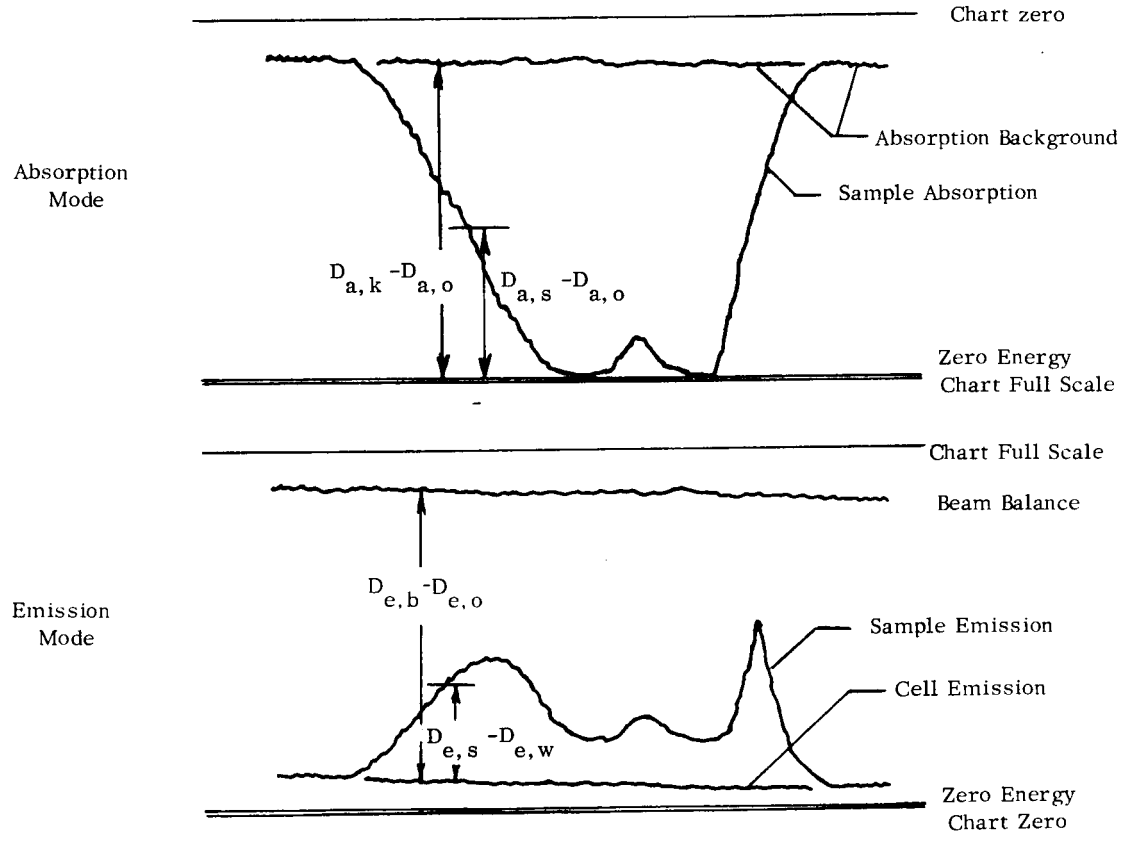

FIGURE A1. SCHEMATIC REPRESENTATION OF VARIOUS SCANS

Output:

1. Absorptance, $\alpha_{iso}(\nu)$

   Equations used:

$$\alpha_{iso}(\nu) = 1 - R_{a,iso}$$

$$R_{a,iso} = \frac{D_{a,s} - D_{a,o}}{D_{a,bk} - D_{a,o}}$$

II. Isothermal Emission

Input:

1. Emission, cell windows, $D_{e,w}$
2. Emission, beam balance, $D_{e,b}$
3. Emission, CO_2 sample, $D_{e,s}$
4. Temperature, average of thermocouple indications, $T_{t.c.}$
5. Window reflectance, ρ_w vs. ν
6. Isothermal absorptance, $\alpha_{iso}(\nu)$

Output:

1. Effective blackbody temperature $T_{bb}(\nu)$
2. Radiance, $L_{\nu,iso}$
3. Apparent temperature, T^*_{iso}
4. Average effective blackbody temperature, $\overline{T}_{bb}$

   Equations used:

$$L^*_{\nu,bb} = \frac{\alpha_{iso}(\nu) L^*_\nu(T_{t.c.})}{R_{e,iso}(1 - \rho_w)^2}$$

$$R_{e,iso} = \frac{D_{e,s} - D_{e,w}}{D_{e,b} - D_{e,w}}$$

$$T_{bb}(\nu) = c_1 \nu^3 \Big/ \ln\left(\frac{c_2 \nu}{L^*_{\nu,bb}} + 1\right)$$

$$\overline{T}_{bb} = \frac{1}{n}\sum_{i=1}^{n} T_{bb}(\nu_i)$$

$$L_{\nu,iso} = R_{e,iso}(1 - \rho_w)^2 L^*_\nu(\overline{T}_{bb})$$

$$T^*_{iso} = c_2 \nu \Big/ \ln\left\{c_1 \nu^3 \alpha_{iso}(\nu) \Big/ L_{\nu,iso}\right] + 1\Big\}$$

III. Window 2 Absorptance at Temperature T_{w2}

Input:

1. Emission, zero, $D_{e,o}$
2. Emission, beam balance, $D_{e,b}$
3. Emission, cell window, $D_{e,w}$
4. Temperature of window 2, T_{w2}
5. Average effective blackbody temperature, $\overline{T}_{bb}$

Output:

1. Window 2 absorptance, $\alpha_2(\nu, T)$

   Equations used:

$$\alpha_2(\nu, T) = \left[1 + \left(\frac{1 - R_w}{R_w}\right) \frac{L_\nu^*(T_{w2})}{L_\nu^*(\overline{T}_{bb})} \frac{1}{(1 - \rho_w)^2}\right]^{-1}$$

$$R_w = \frac{D_{e,w} - D_{e,o}}{D_{e,b} - D_{e,o}}$$

IV. Nonisothermal Absorption

Input:

1. Absorption, zero, $D_{a,o}$
2. Absorption, background, $D_{a,bk}$
3. Absorption, sample gas, $D_{a,s}$

Output:

1. Spectral absorptance, sample gas, $\alpha(\nu)$

   Equations used:

$$\alpha(\nu) = 1 - R_a$$

$$R_a = \frac{D_{a,s} - D_{a,o}}{D_{a,bk} - D_{a,o}}$$

V. Nonisothermal Emission

Input:

1. Emission, cell windows, $D_{e,w}$
2. Emission, beam balance, $D_{e,b}$
3. Emission, sample gas, $D_{e,s}$
4. Blackbody temperature, $\overline{T}_{bb}$

5. Window reflectance, ρ_w
6. Window 2 absorptance, $\alpha_2(\nu, T)$
7. Window 2 temperature, T_{w2}
8. Spectral absorptance, sample gas, $\alpha(\nu)$

Output:

1. Spectral radiance, sample gas, L_ν
2. Apparent temperature, sample gas, $T^*(\nu)$

Equations used:

$$L_\nu = R_e L_\nu^*(\overline{T}_{bb})(1 - \rho_w)^2(1 - \alpha_2) + L_\nu^*(T_{w2})\alpha_2\alpha(\nu)$$

$$R_e = \frac{D_{e,s} - D_{e,w}}{D_{e,b} - D_{e,w}}$$

Appendix B
EMISSION AND ABSORPTION SPECTRA

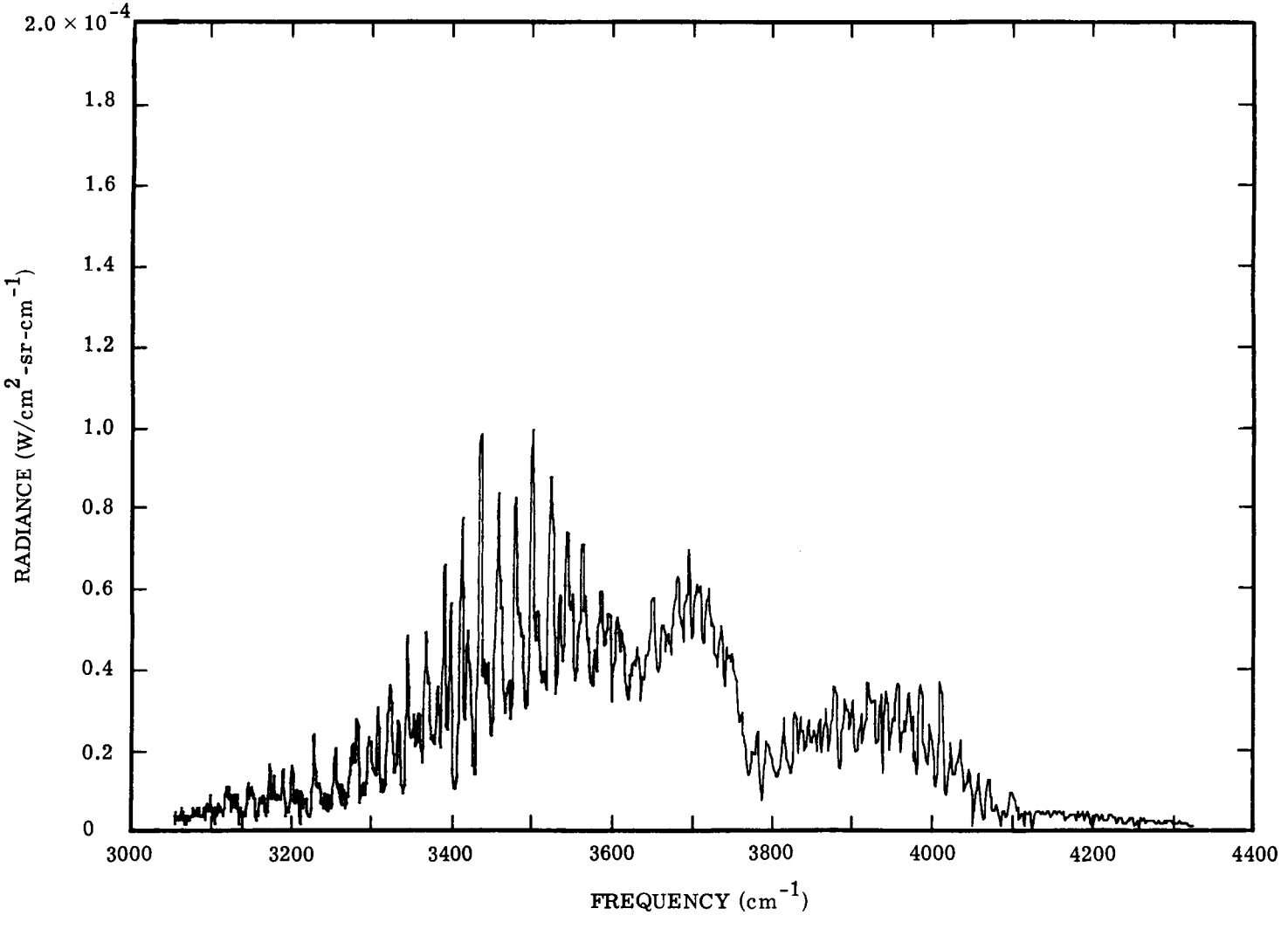

FIGURE B1. SPECTRAL RADIANCE, RUN 10216807. Gas: $H_2O/CO_2/N_2$. P = 57, 28, 675 mm. Temperature (^oK) = 378, 537, 723, 958, 1127, 1158, 990, 752, 555, 383.

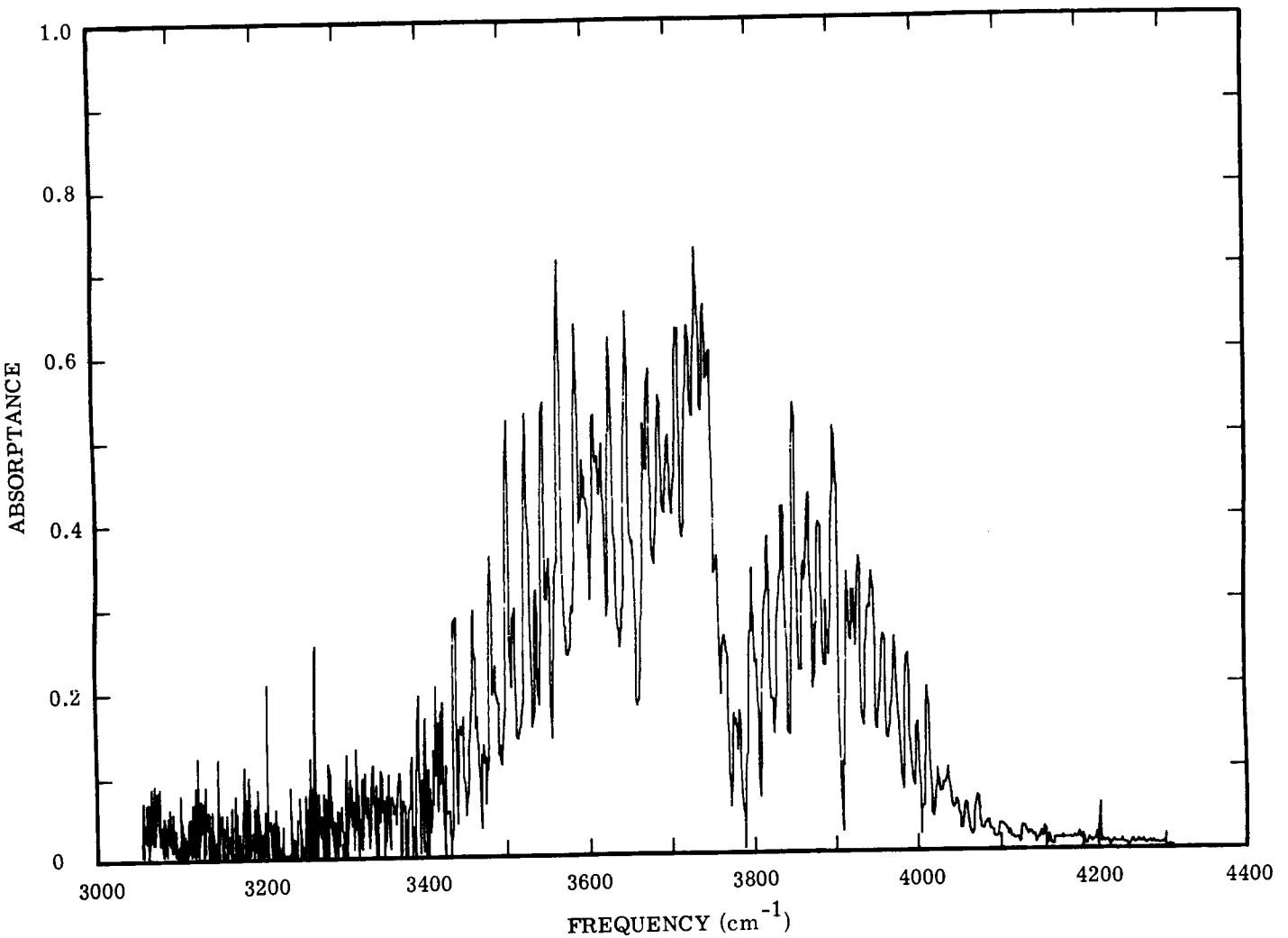

FIGURE B2. SPECTRAL ABSORPTANCE, RUN 10216807. Gas: $H_2O/CO_2/N_2$. P = 57, 28, 675 mm. Temperture (^oK) = 378, 537, 723, 958, 1127, 1158, 990, 752, 555, 383.

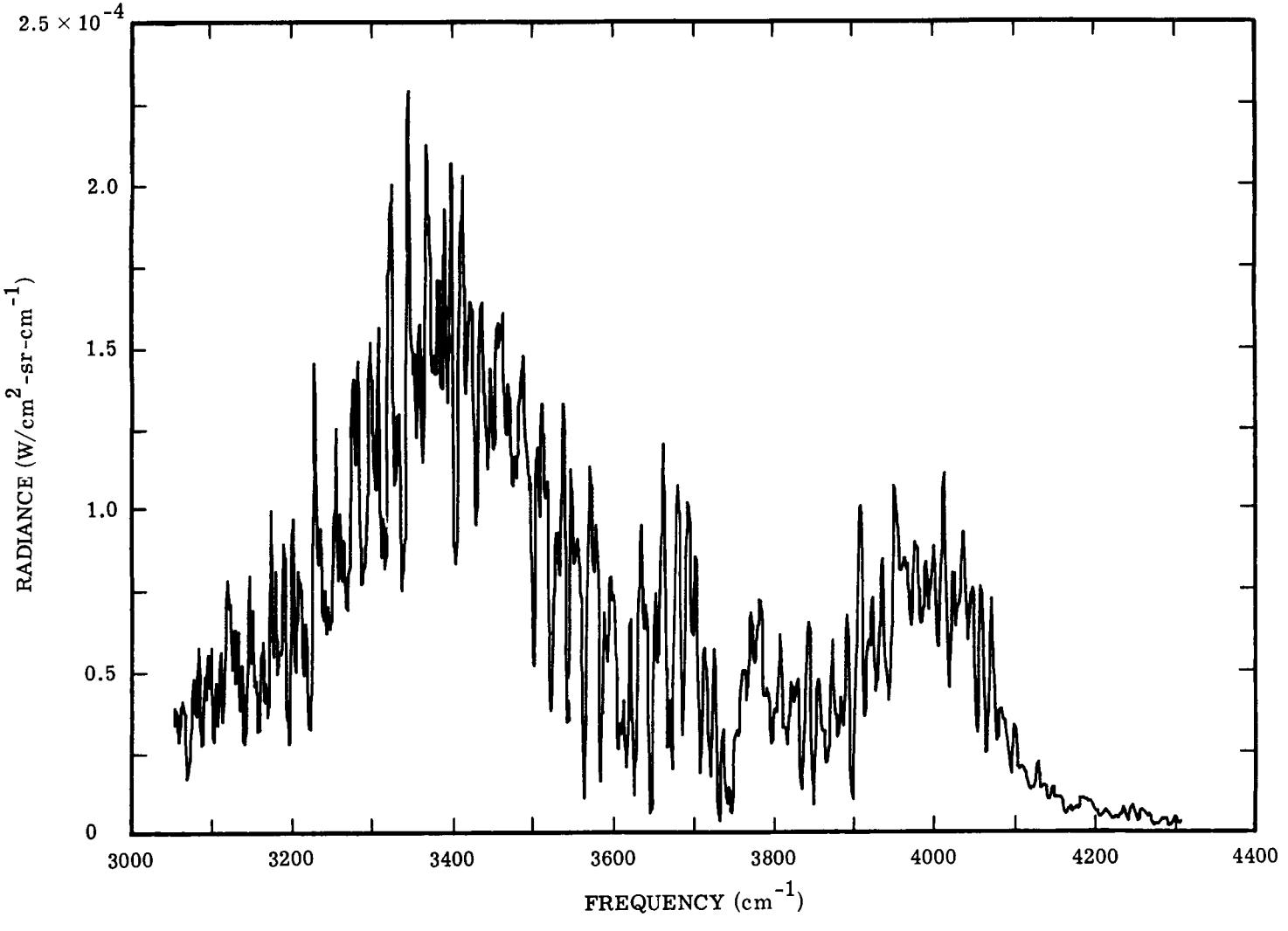

FIGURE B3. SPECTRAL RADIANCE, RUN 10216811. Gas: H_2O. P = 670 mm. Temperature (^oK) = 382, 537, 723, 953, 1128, 1160, 990, 751, 558, 389.

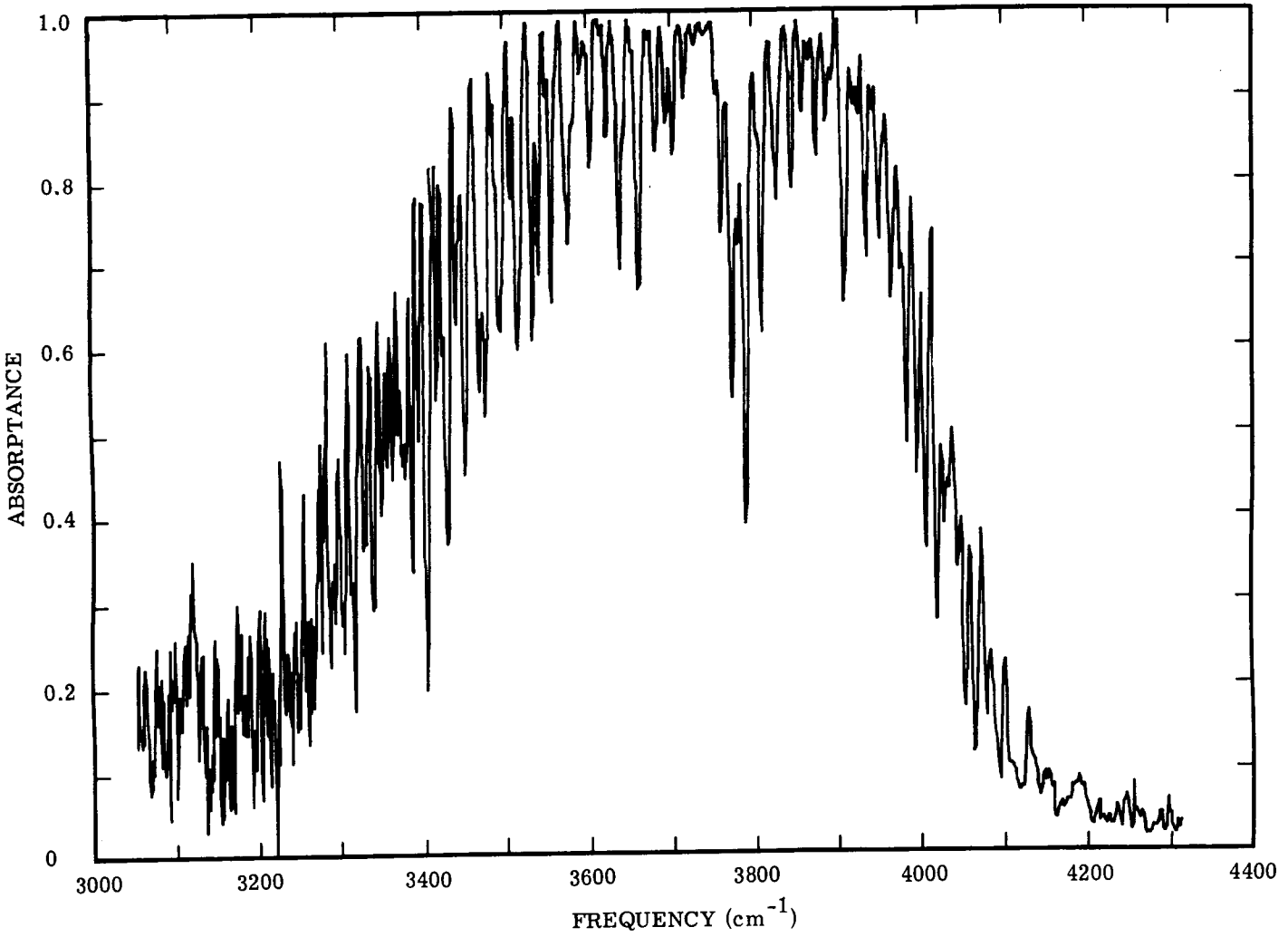

FIGURE B4. SPECTRAL ABSORPTANCE, RUN 10216811. Gas: H_2O. P = 670 mm. Temperature (^oK) = 382, 537, 723, 953, 1128, 1160, 990, 751, 558, 389.

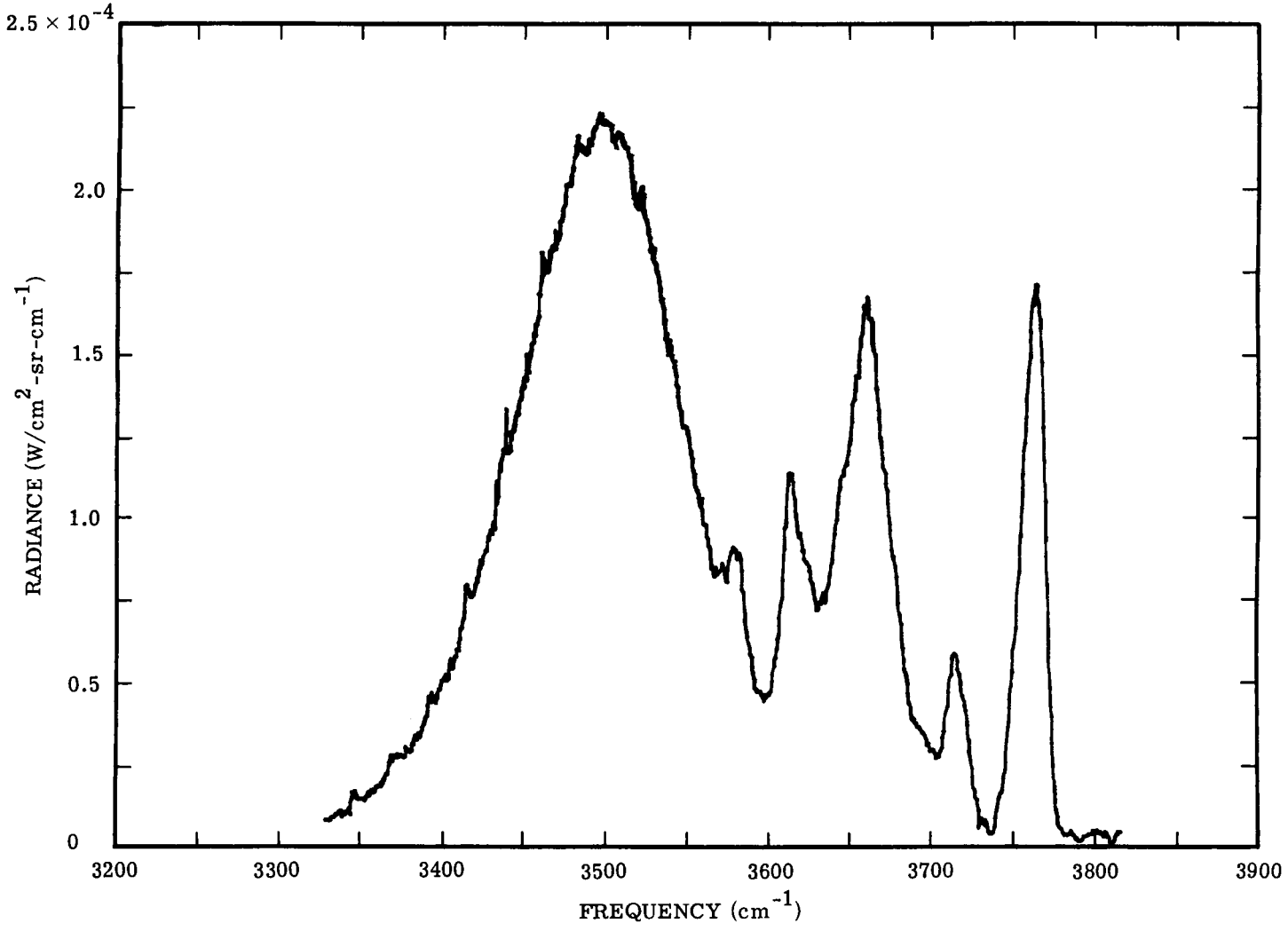

FIGURE B5. SPECTRAL RADIANCE, RUN 10216812. Gas: CO_2. P = 760 mm. Temperature (^{o}K) = 386, 528, 719, 953, 1130, 1160, 979, 737, 541, 387.

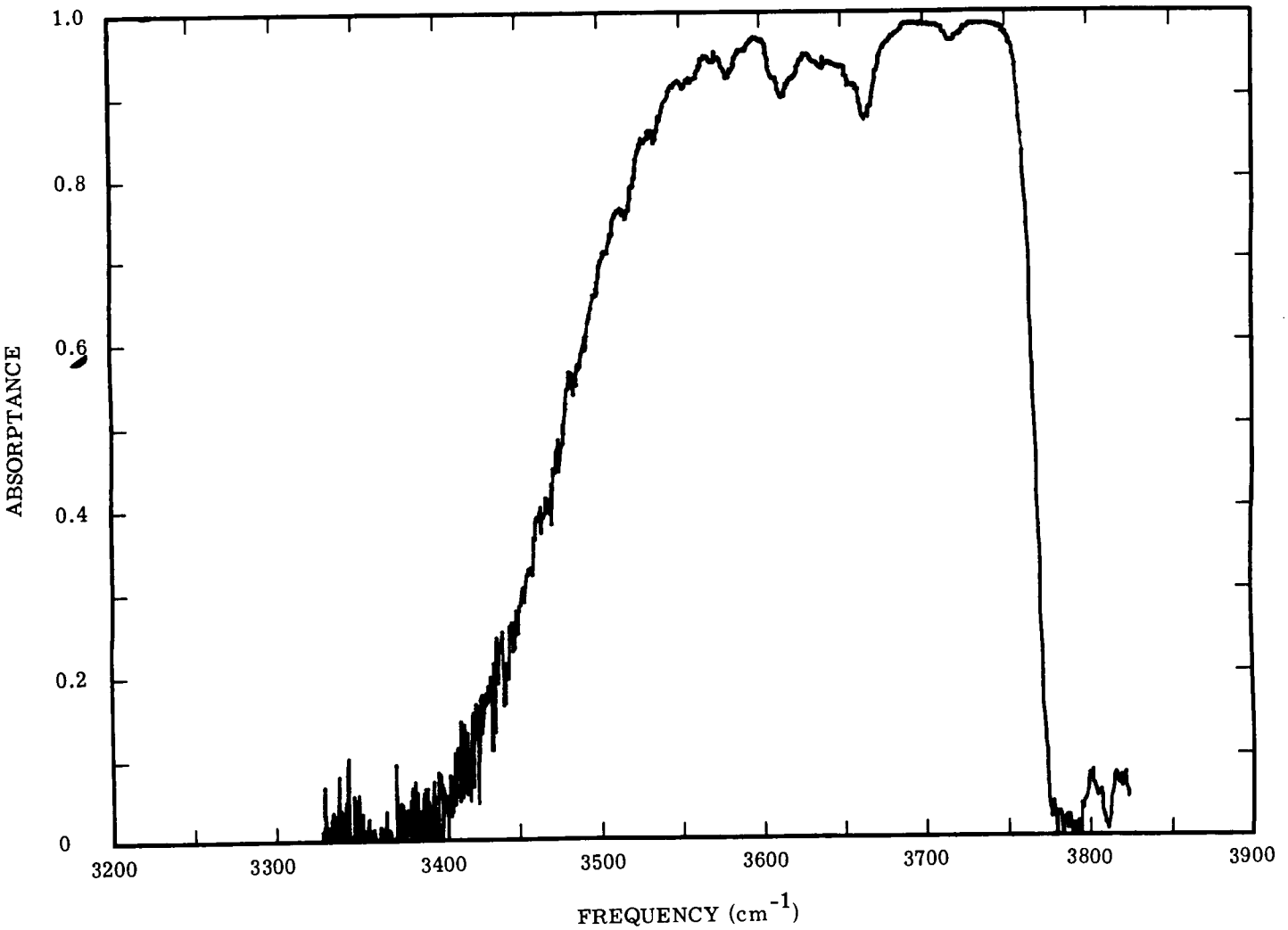

FIGURE B6. SPECTRAL ABSORPTANCE, RUN 10216812. Gas: CO_2. P = 760 mm. Temperature (^{o}K) = 386, 528, 719, 953, 1130, 1160, 979, 737, 541, 387.

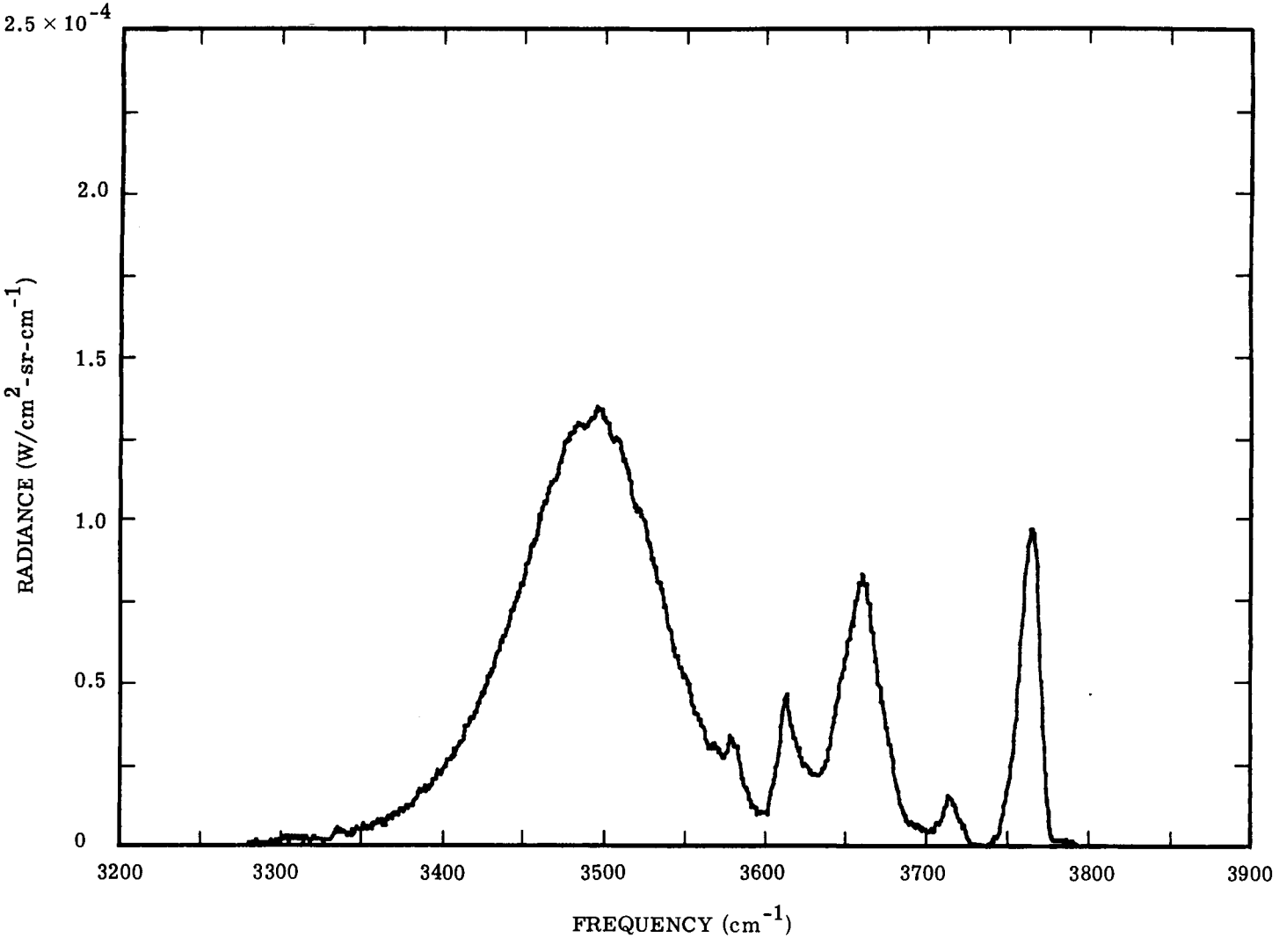

FIGURE B7. SPECTRAL RADIANCE, RUN 10246808. Gas: CO_2. P = 760 mm. Temperature (^oK) = 390, 464, 537, 641, 715, 824, 914, 994, 1061, 1153.

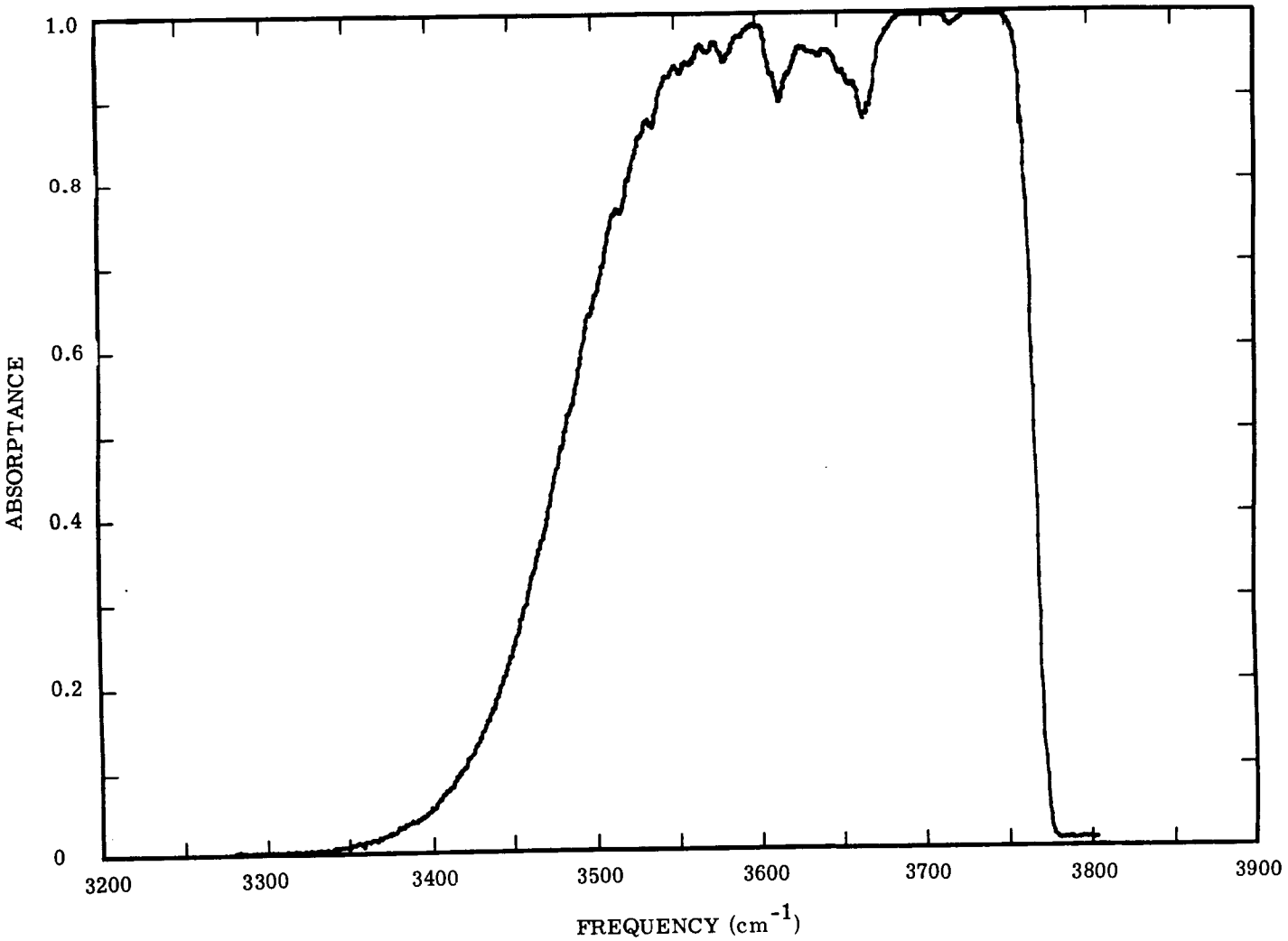

FIGURE B8. SPECTRAL ABSORPTANCE, RUN 10246808. Gas: CO_2. P = 760 mm. Temperature (^{o}K) = 390, 464, 537, 641, 715, 824, 914, 994, 1061, 1153.

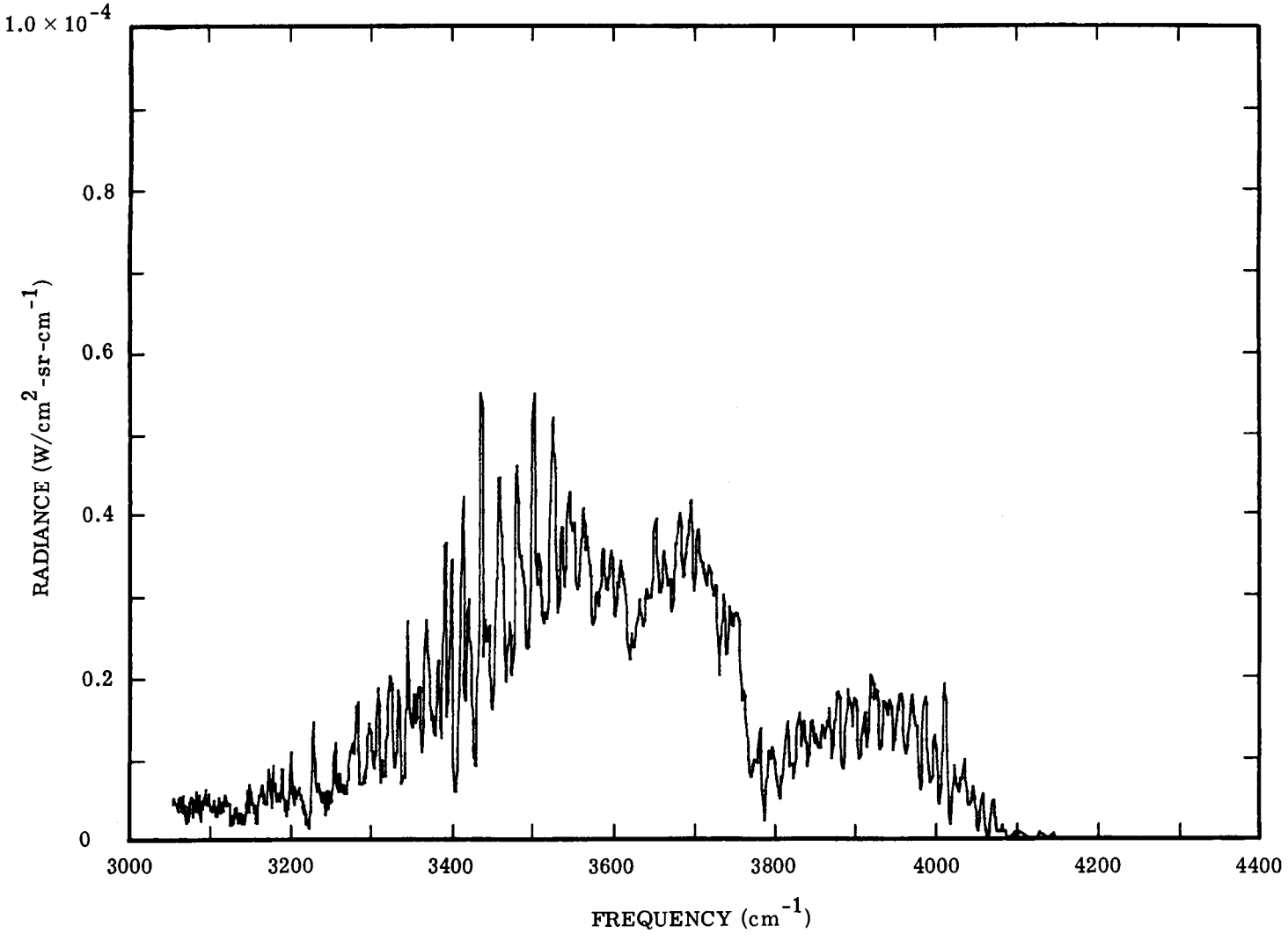

FIGURE B9. SPECTRAL RADIANCE, RUN 10246812. Gas: $H_2O/CO_2/N_2$. P = 54, 28, 679 mm. Temperature (°K) = 395, 517, 594, 673, 744, 833, 915, 990, 1057, 1153.

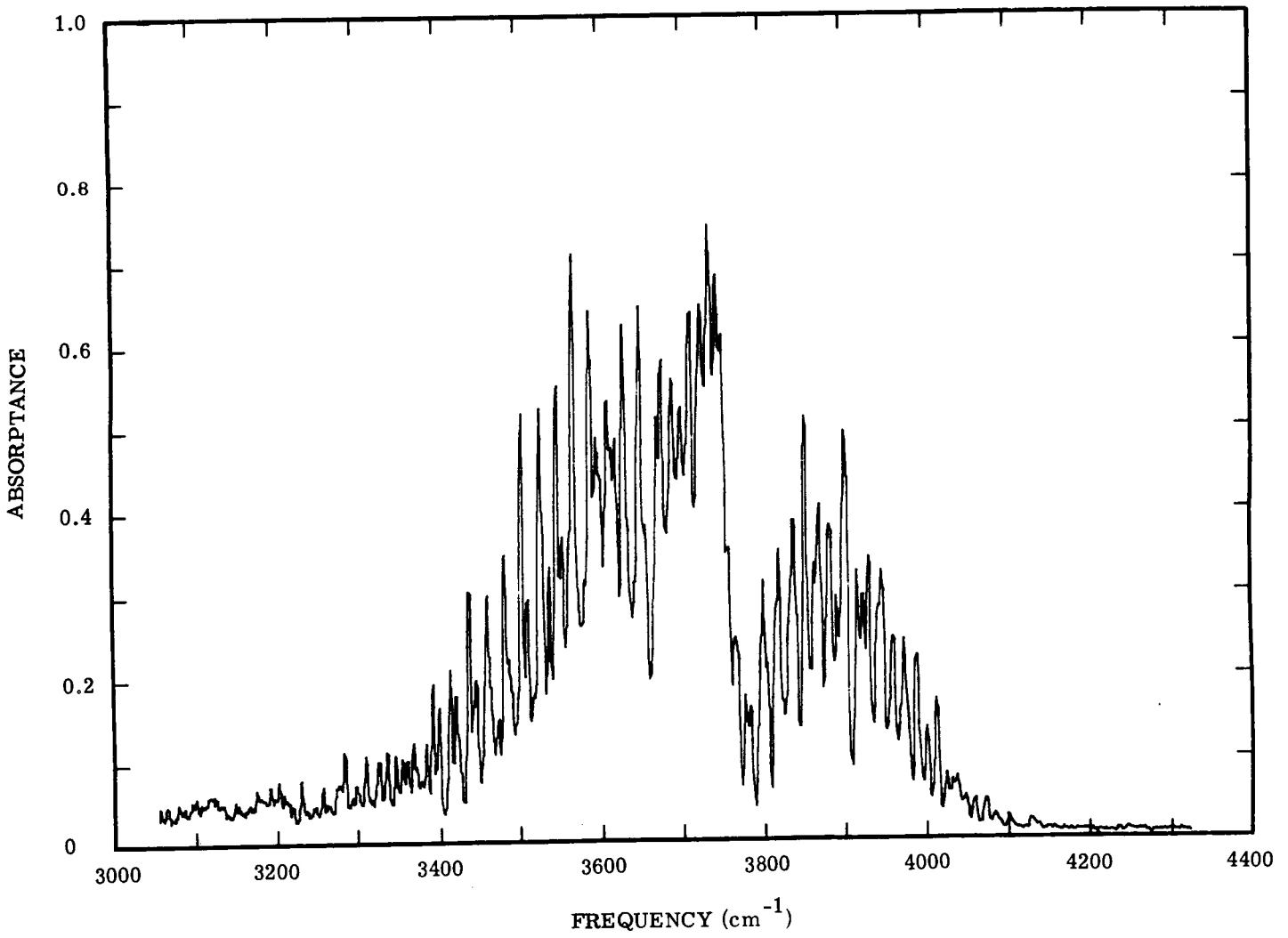

FIGURE B10. SPECTRAL ABSORPTANCE, RUN 10246812. Gas: H_2O/ CO_2/N_2. P = 54, 28, 679 mm. Temperature (^{o}K) = 395, 517, 594, 673, 744, 833, 915, 990, 1057, 1153.

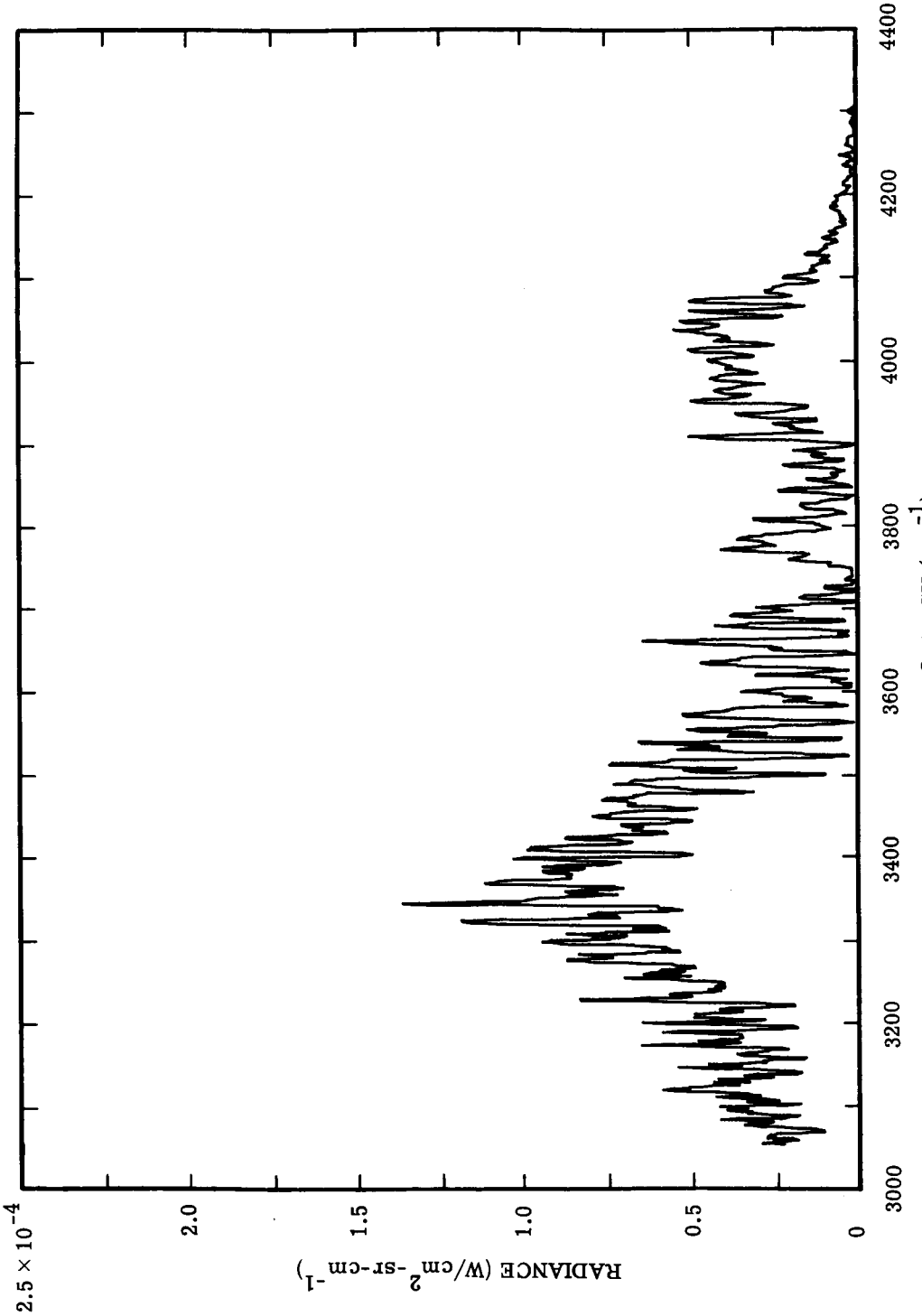

FIGURE B11. SPECTRAL RADIANCE, RUN 10246813. Gas: H_2O. P = 692 mm. Temperature (°K) 392, 513, 593, 671, 745, 835, 918, 993, 1059, 1152.

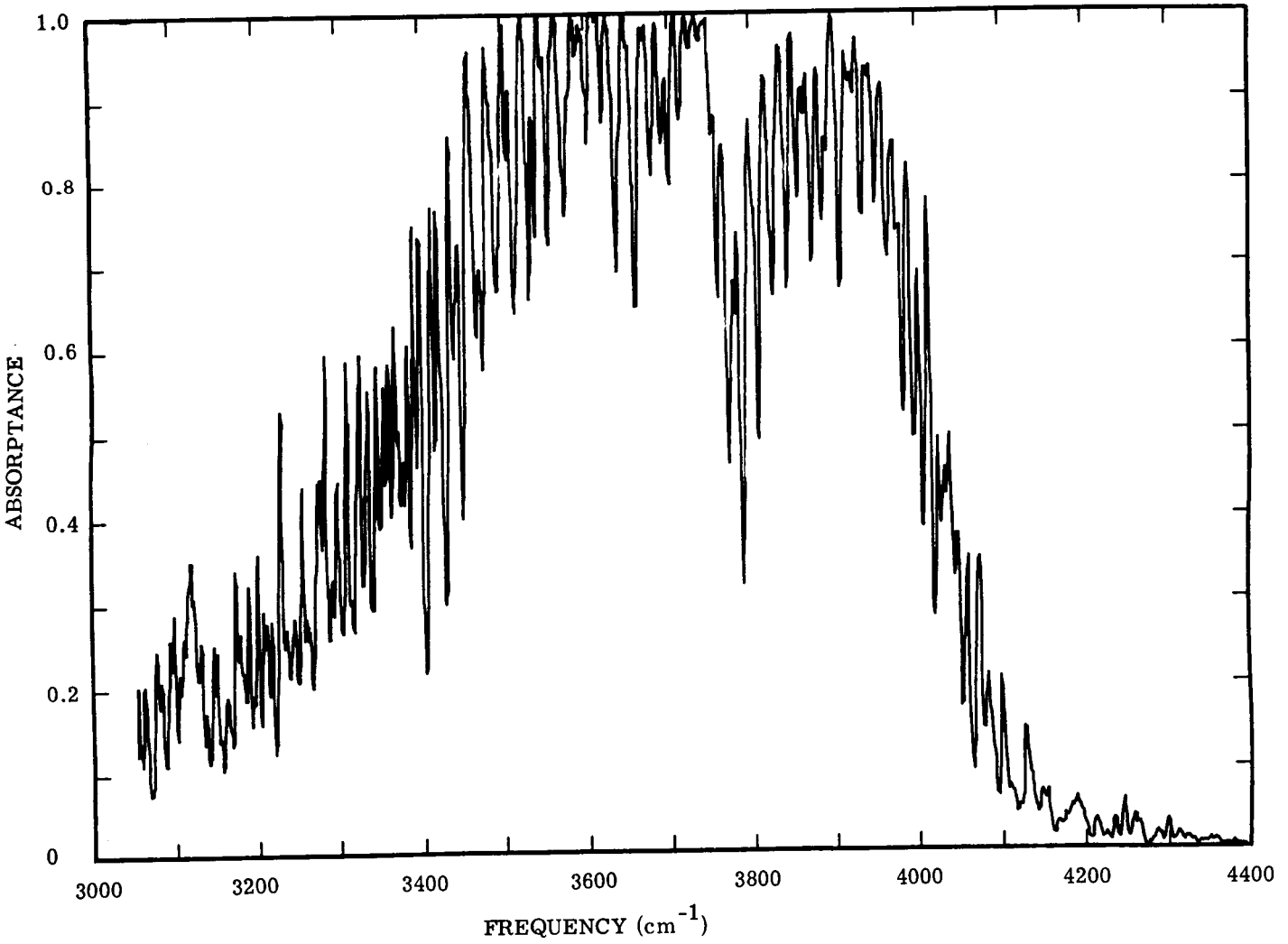

FIGURE B12. SPECTRAL ABSORPTANCE, RUN 10246813, Gas: H_2O. P = 692 mm. Temperature (^oK) = 392, 513, 593, 671, 745, 835, 918, 993, 1059, 1152.

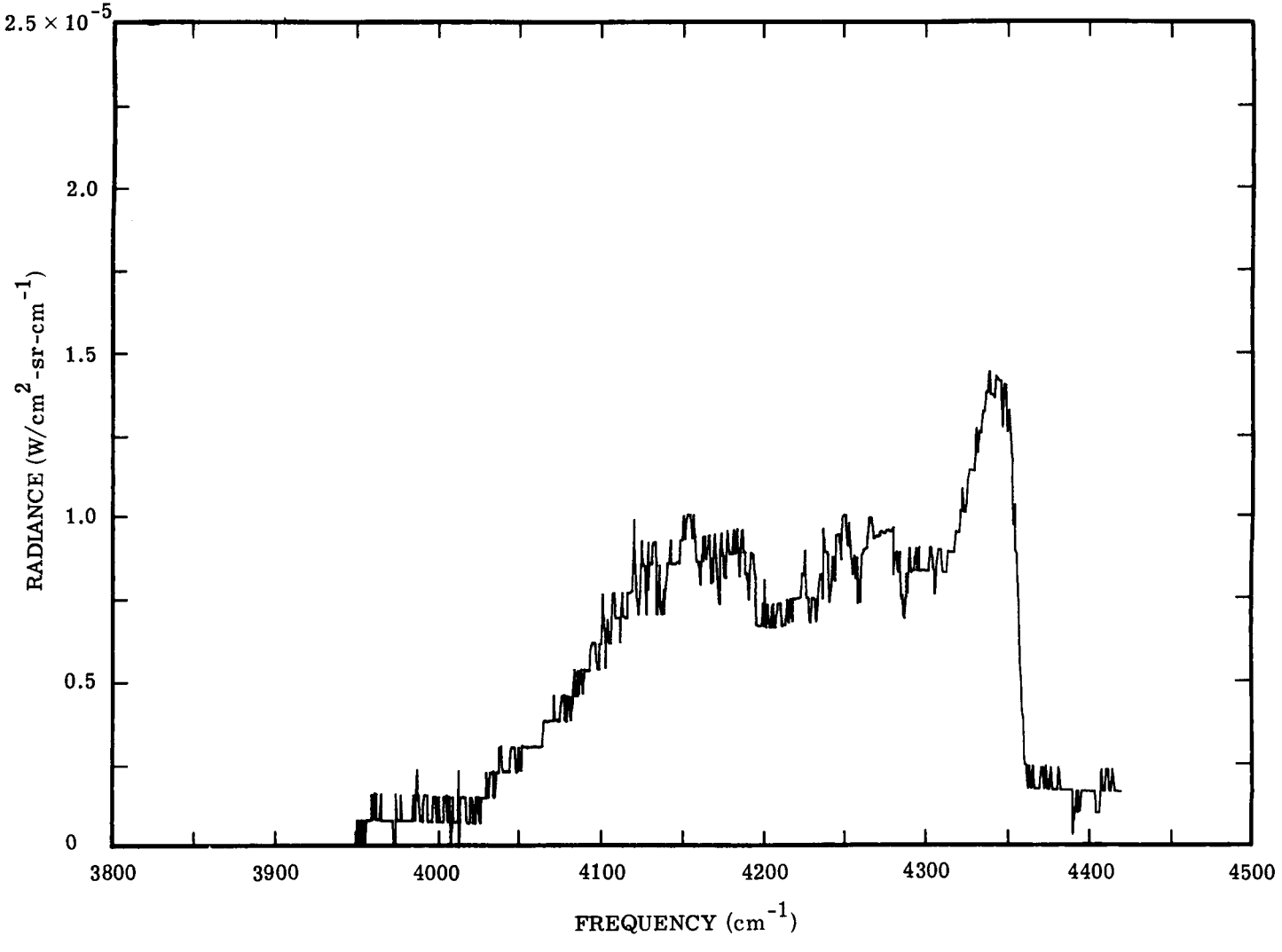

FIGURE B13. SPECTRAL RADIANCE, RUN 10246818. Gas: CO. P = 1520 mm. Temperature (^{O}K) = 388, 485, 554, 639, 729, 831, 918, 994, 1061, 1150.

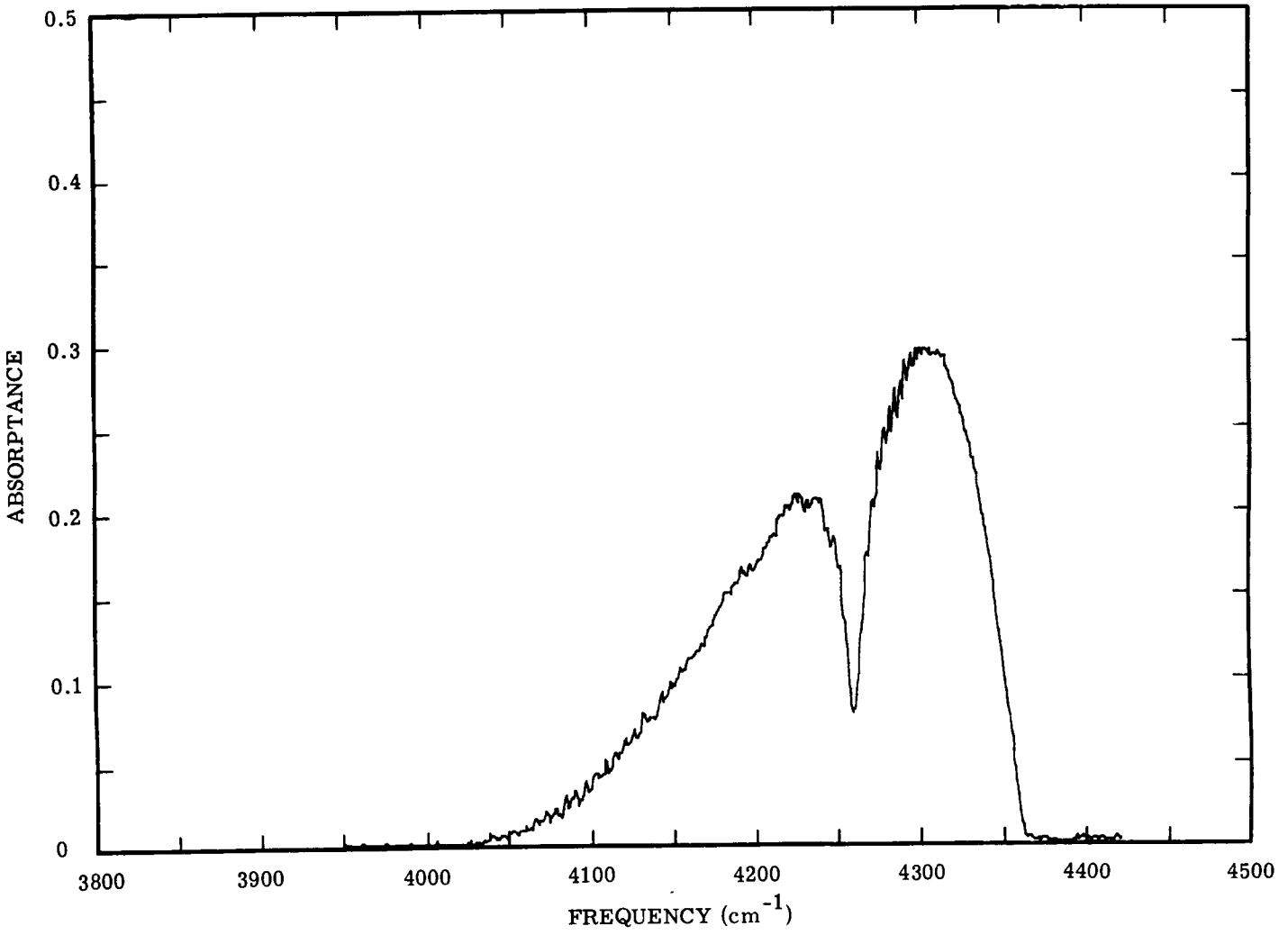

FIGURE B14. SPECTRAL ABSORPTANCE, RUN 10246818. Gas: CO. P = 1520 mm. Temperature (^{o}K) = 388, 485, 554, 639, 729, 831, 918, 994, 1061, 1150.

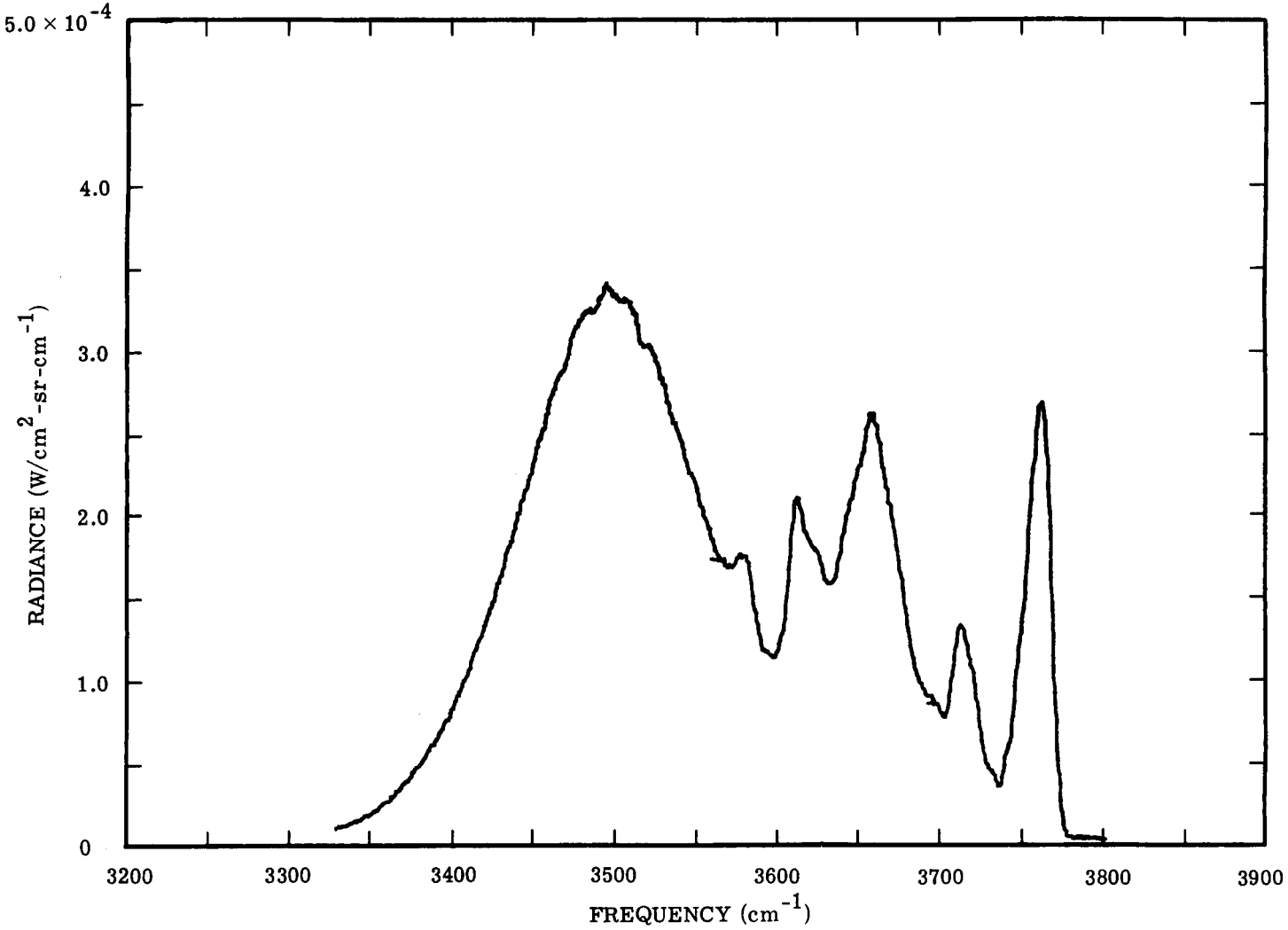

FIGURE B15. SPECTRAL RADIANCE, RUN 10286811. Gas: CO_2. P = 760 mm. Temperature (^{o}K) = 424, 649, 884, 1147, 1147, 1149, 1147, 873, 637, 424.

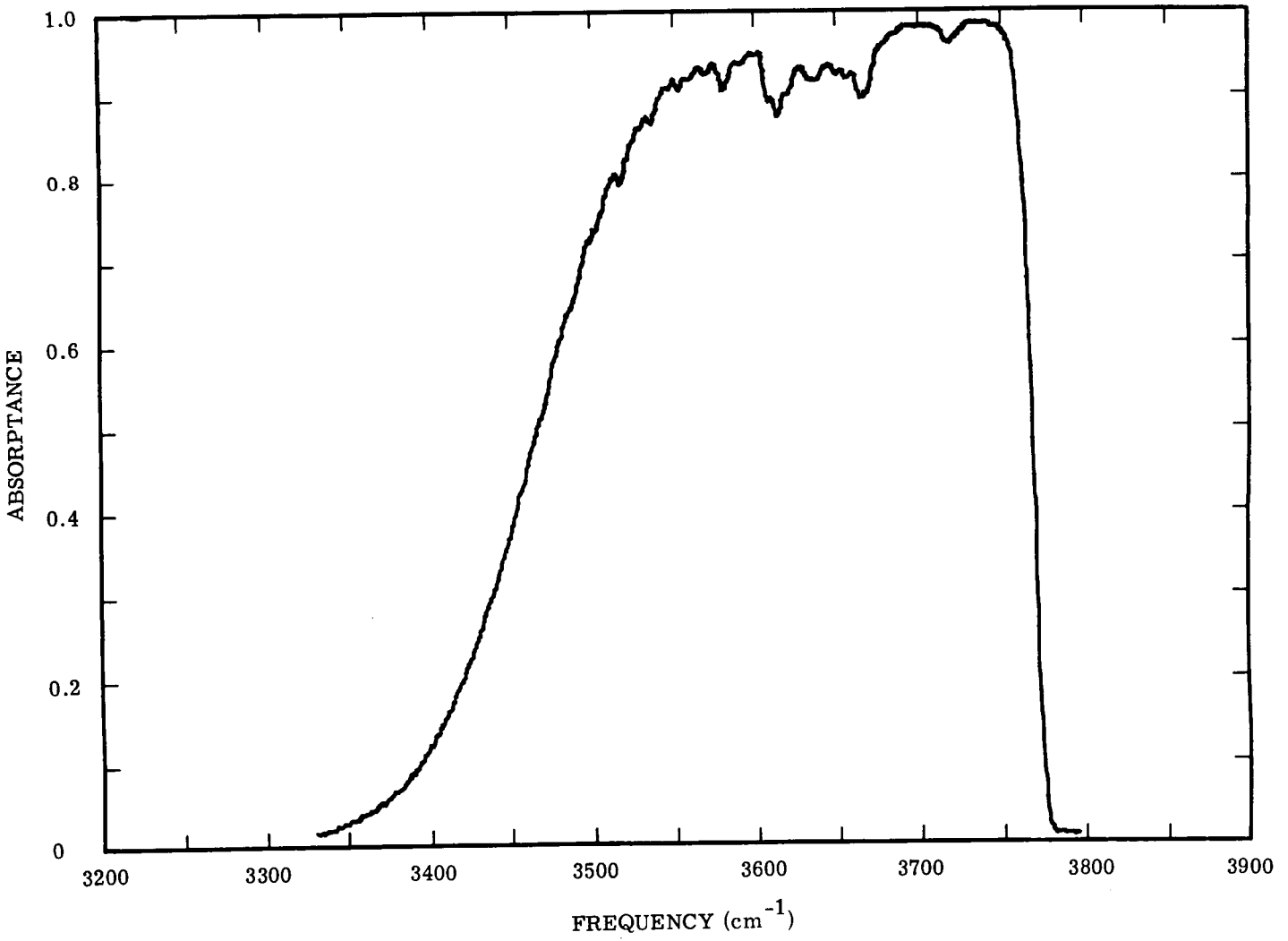

FIGURE B16. SPECTRAL ABSORPTANCE, RUN 10286811. Gas: CO_2. P = 760 mm. Temperature (^{o}K) = 424, 649, 884, 1147, 1147, 1149, 1147, 873, 637, 424.

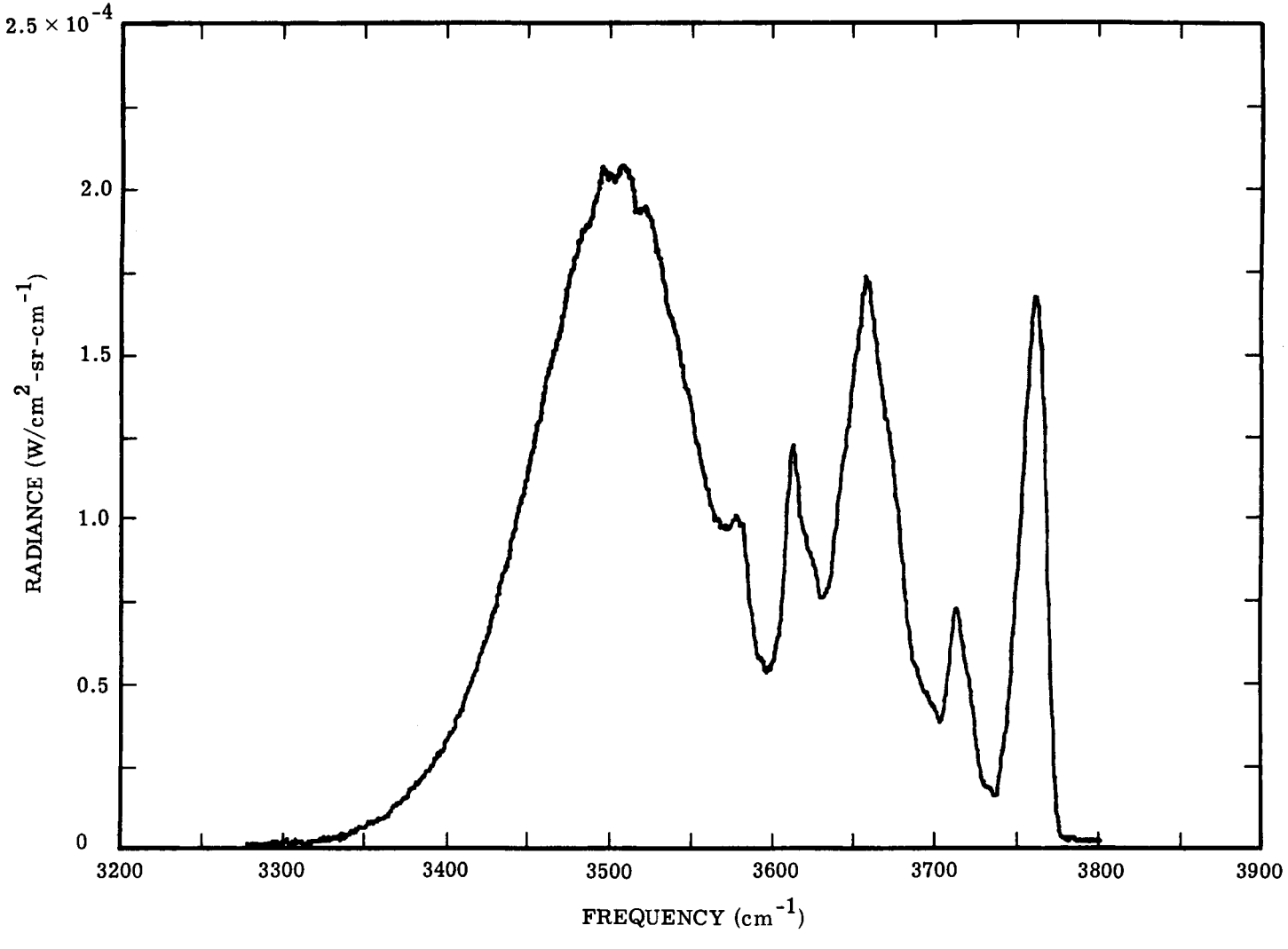

FIGURE B17. SPECTRAL RADIANCE, RUN 10286816. Gas: CO_2. P = 760 mm. Temperature (^oK) = 368, 535, 813, 1136, 855, 871, 1136, 812, 541, 374.

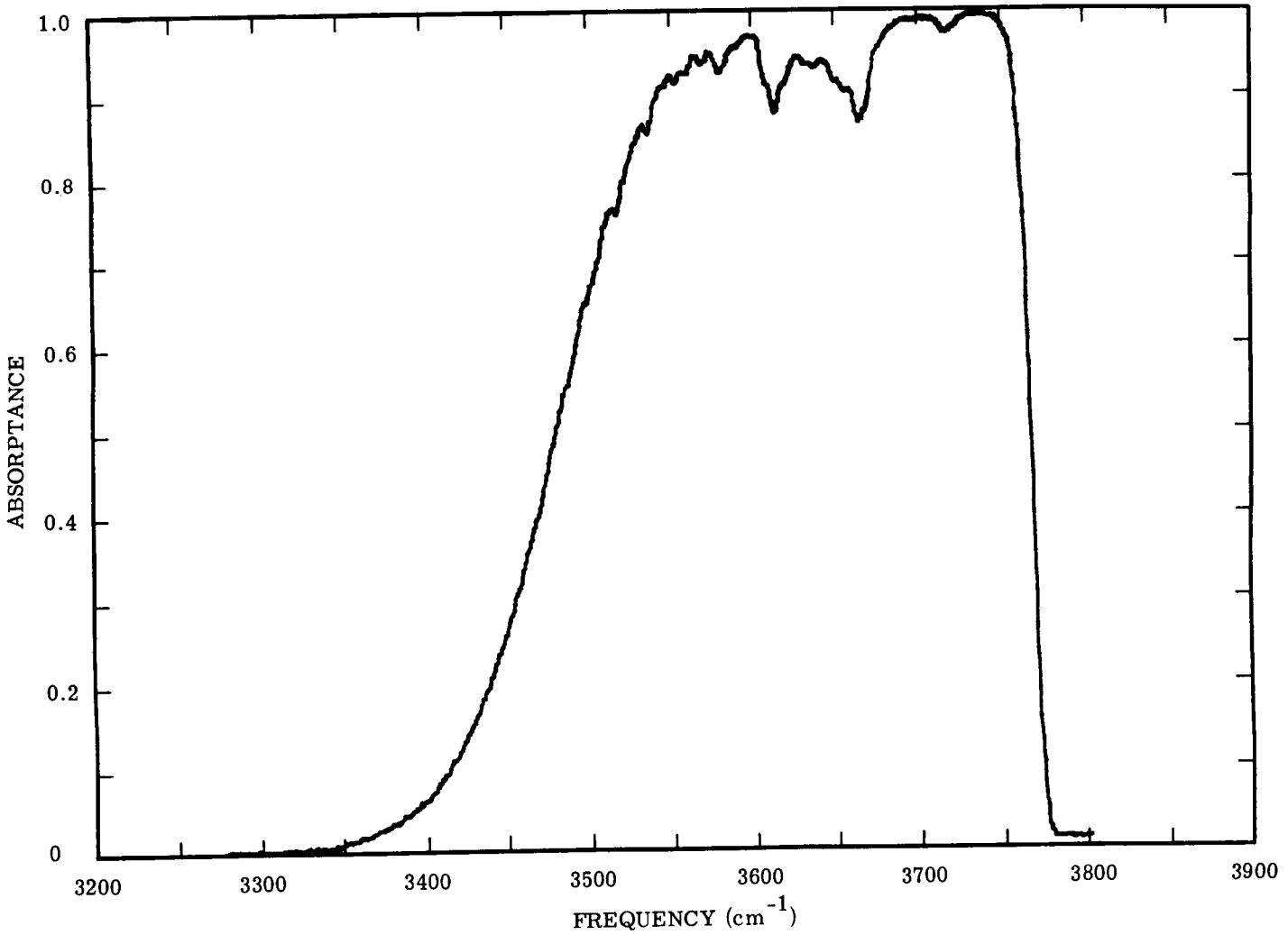

FIGURE B18. SPECTRAL ABSORPTANCE, RUN 10286816. Gas: CO_2. P = 760 mm. Temperature (^{o}K) = 368, 535, 813, 1136, 855, 871, 1136, 812, 541, 374.

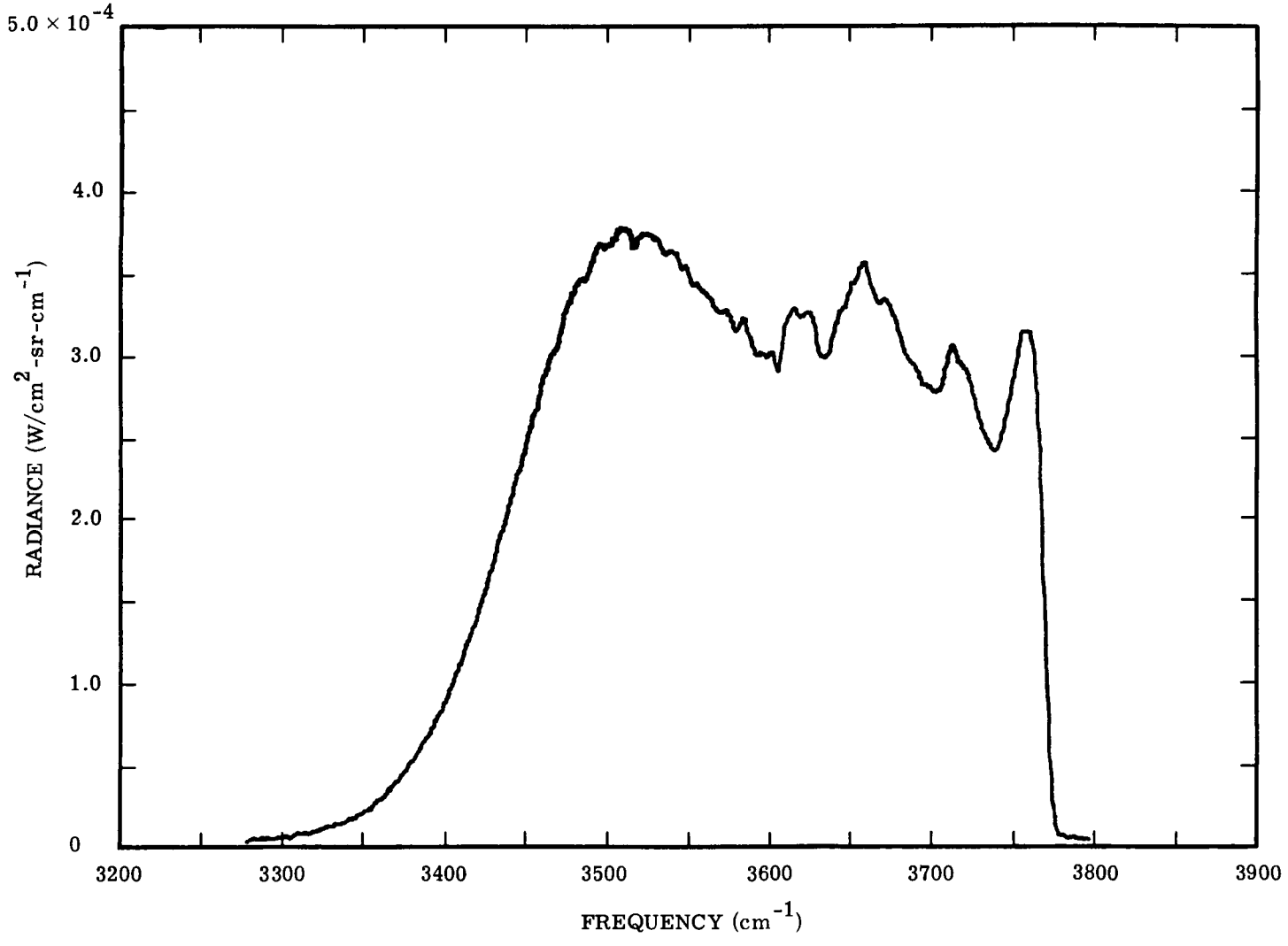

FIGURE B19. SPECTRAL RADIANCE, RUN 10286821. Gas: CO_2. P = 760 mm. Temperature (^oK) = 518, 1132, 1160, 781, 1060, 1062, 777, 1160, 1114, 536.

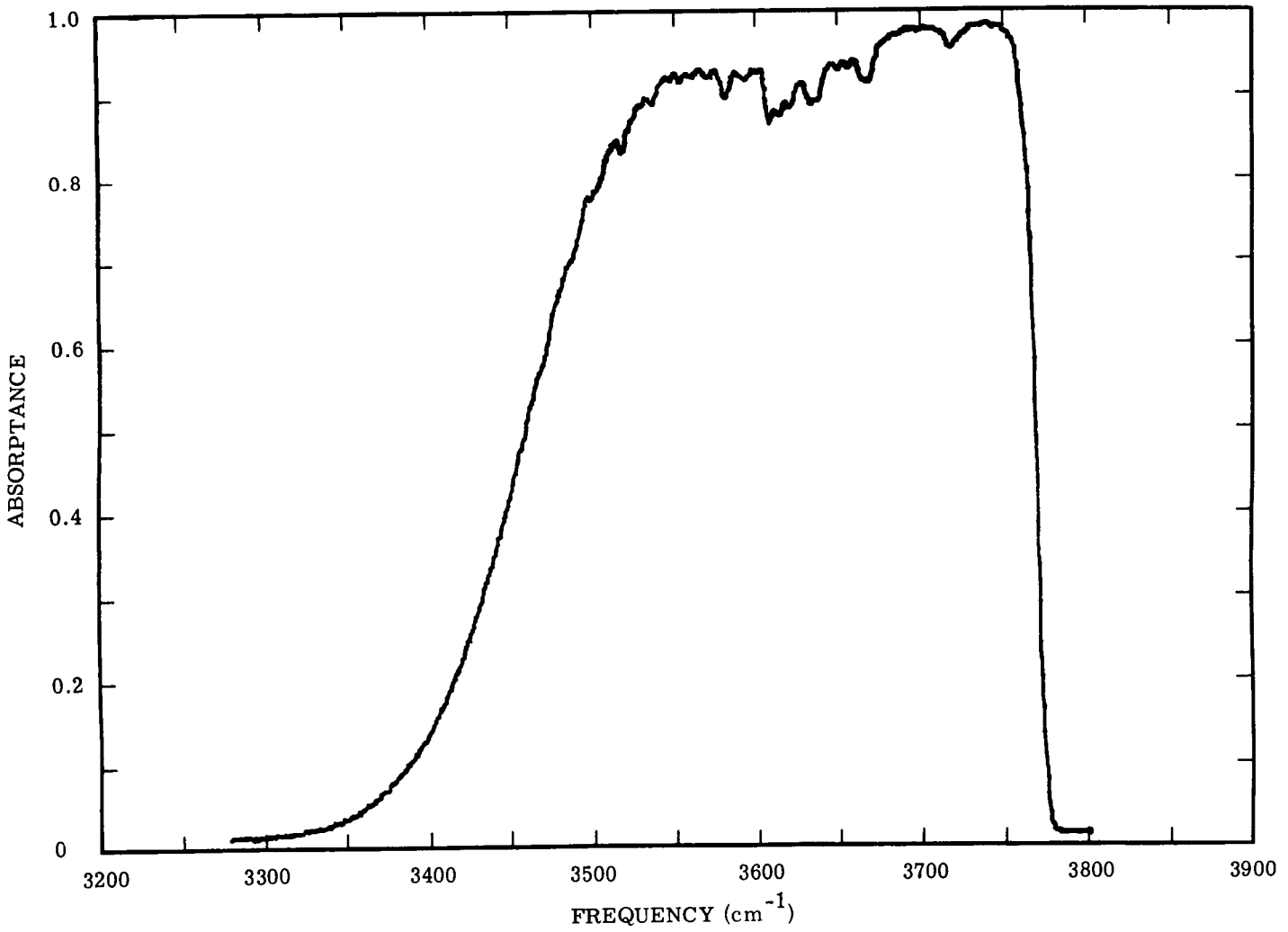

FIGURE B20. SPECTRAL ABSORPTANCE, RUN 1028621. Gas: CO_2. P = 760 mm. Temperature (^{o}K) = 518, 1132, 1160, 781, 1060, 1062, 777, 1160, 1114, 536.

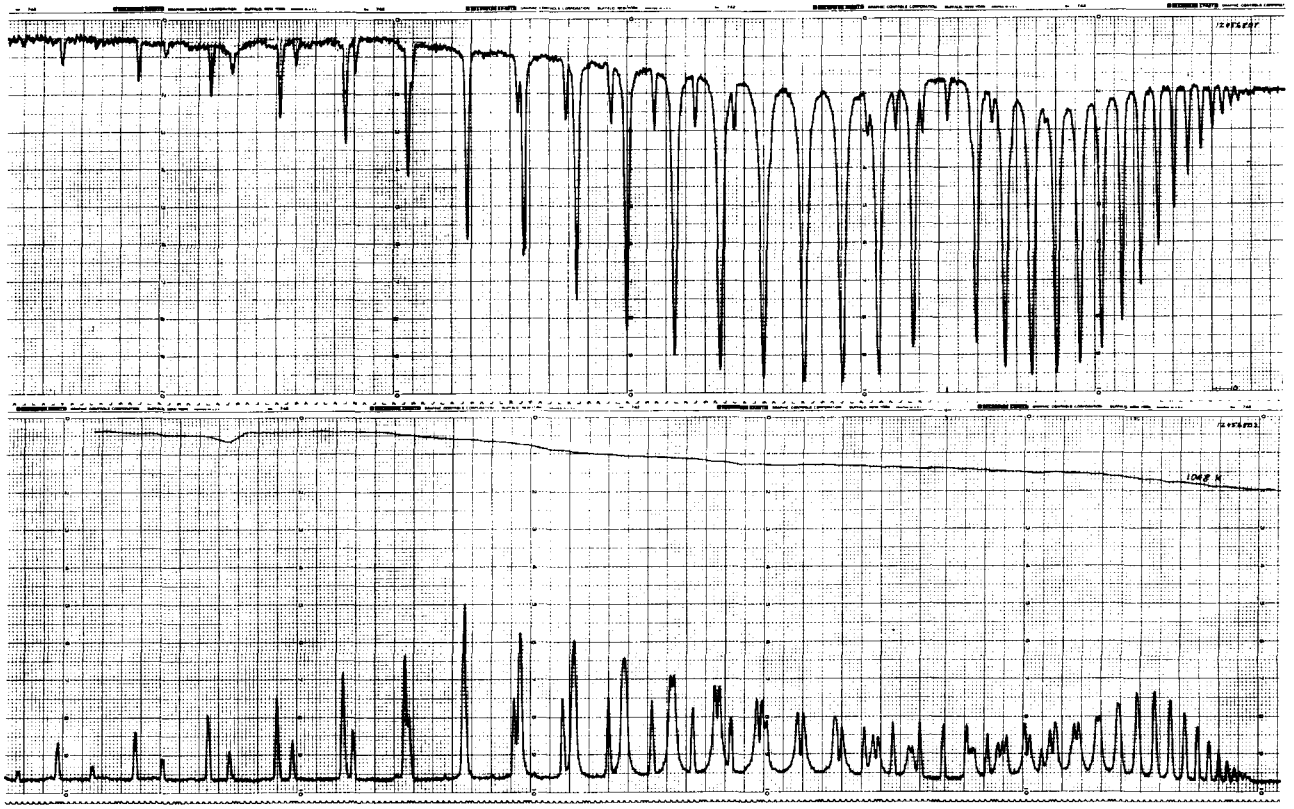

FIGURE B21. EMISSION AND ABSORPTION SPECTRA, RUN 12056804. Gas: HF. P = 397 mm. Temperature (^{O}K) = 498, 723, 892, 1105, 1184, 1189, 1090, 908, 725, 497.

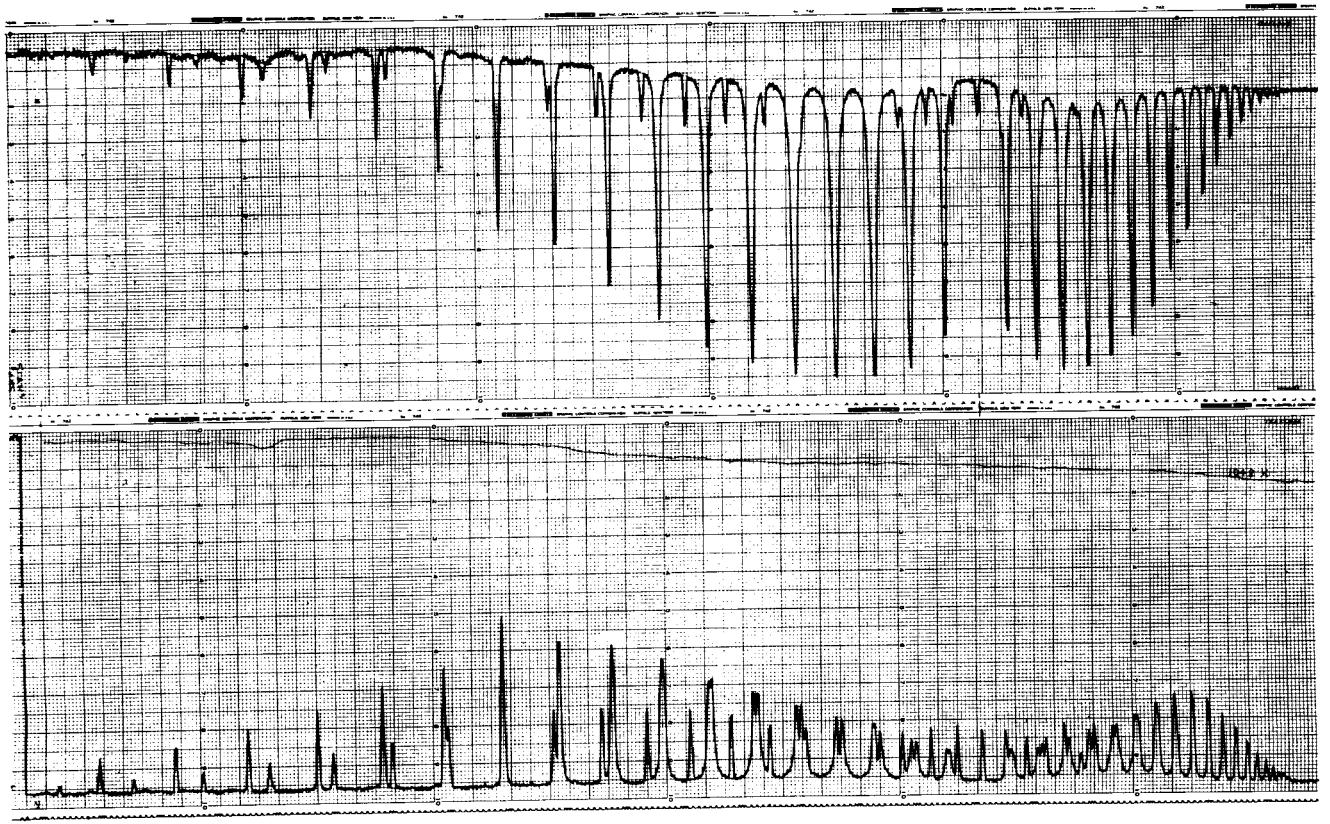

FIGURE B22. EMISSION AND ABSORPTION SPECTRA, RUN 12056804 (REPEAT). Gas: HF. P = 397 mm. Temperature (^{O}K) = 498, 723, 892, 1105, 1184, 1189, 1090, 908, 725, 497.

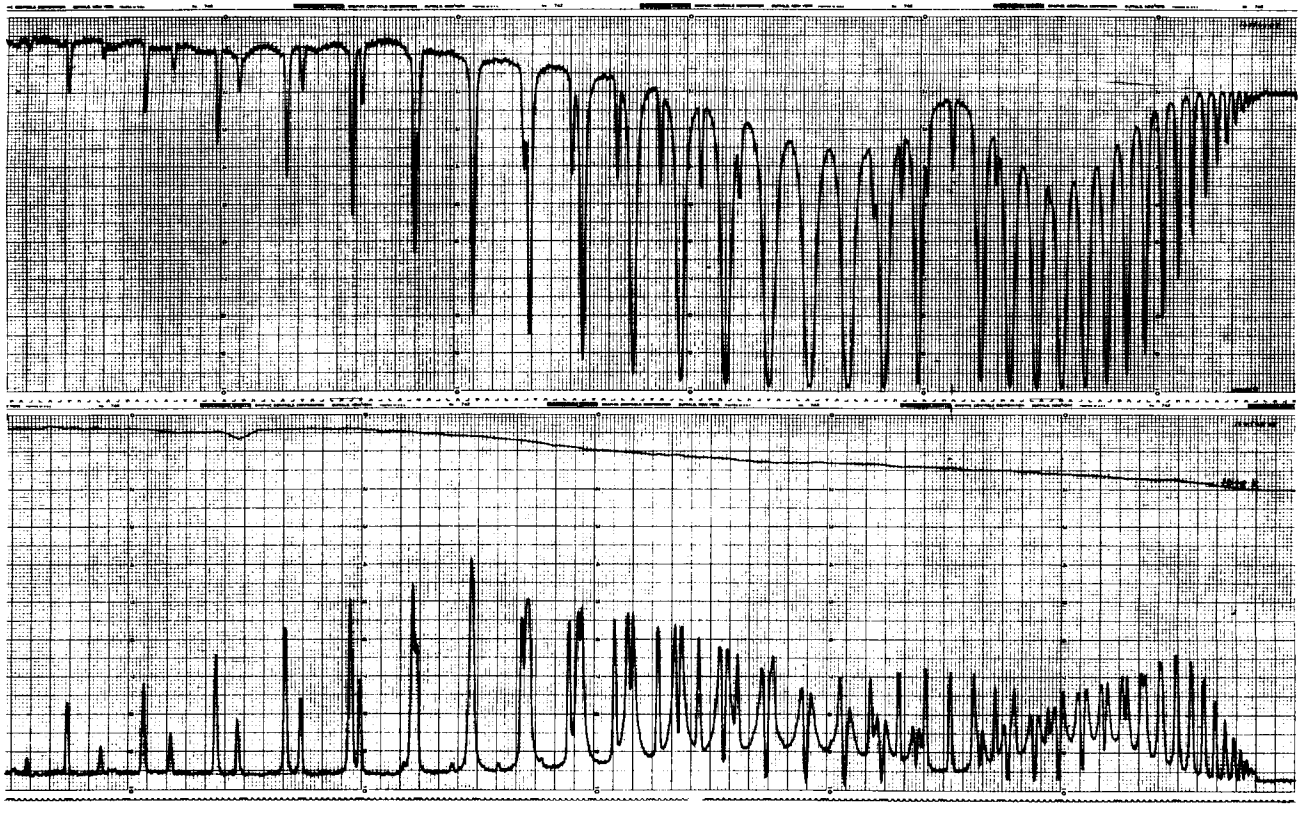

FIGURE B23. EMISSION AND ABSORPTION SPECTRA, RUN 12056808. Gas: HF. P = 751 mm. Temperature (^{O}K) = 494, 723, 896, 1107, 1186, 1189, 1092, 908, 725, 489.

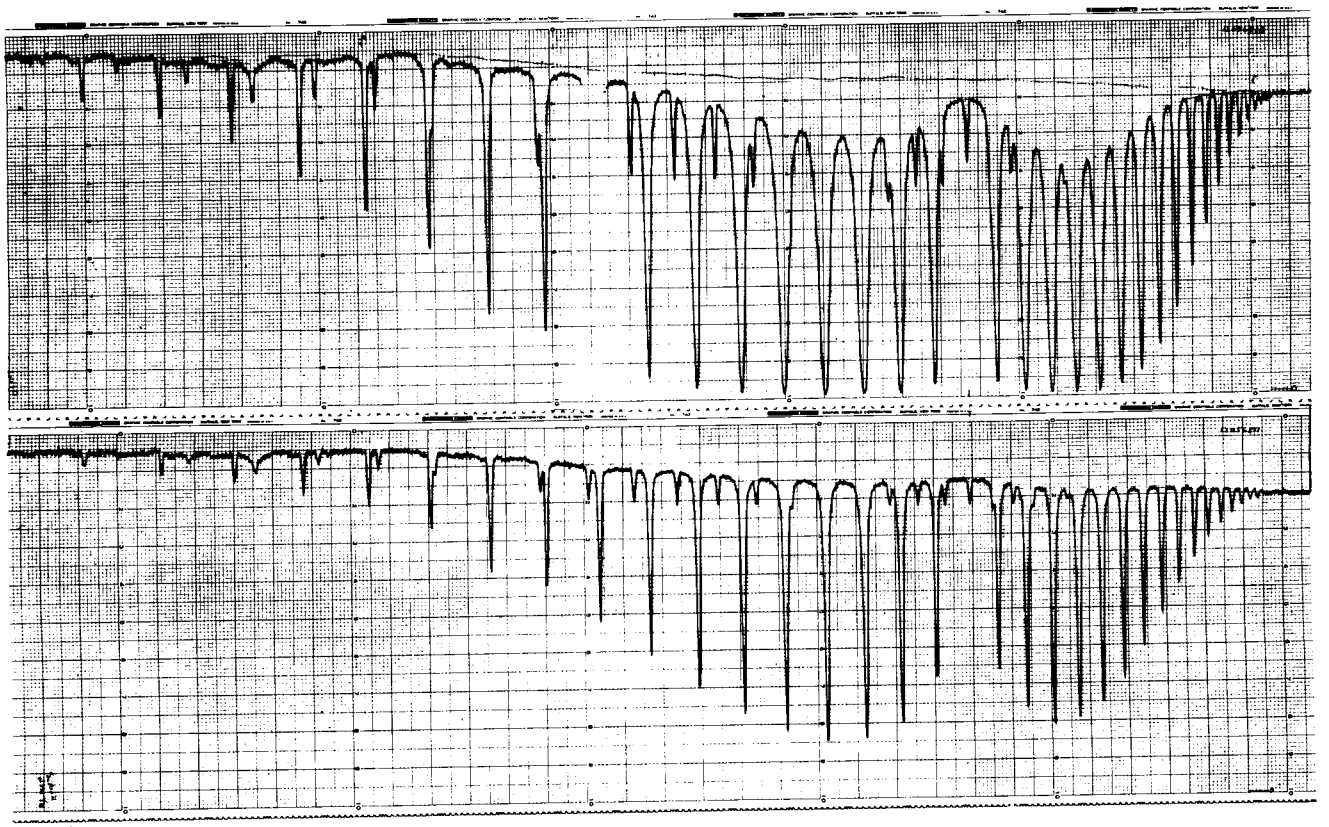

FIGURE B24. ABSORPTION SPECTRA, RUN 12056808 (REPEAT) AND RUN 12056812 (REPEAT). For Run 12056808, Gas: HF. P = 751 mm. Temperature (^{o}K) = 494, 723, 896, 1107, 1186, 1189, 1092, 908, 725, 489. For Run 12056812, gas: HF. P = 191 mm. Temperature (^{o}K) = 488, 725, 898, 1112, 1192, 1199, 1100, 913, 729, 485.

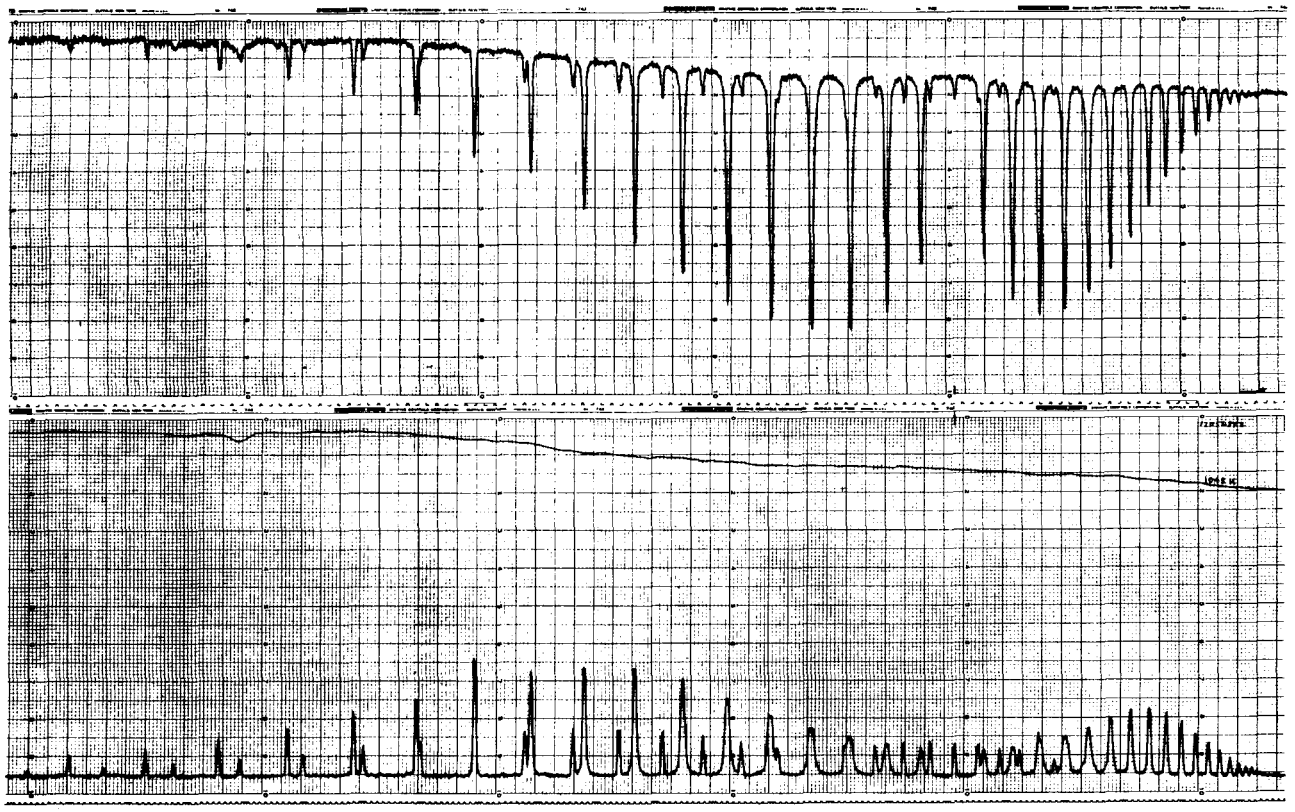

FIGURE B25. EMISSION AND ABSORPTION SPECTRA, RUN 12056812. Gas: HF. P = 191 mm. Temperature (^{O}K) = 488, 725, 898, 1112, 1192, 1199, 1100, 913, 729, 485.

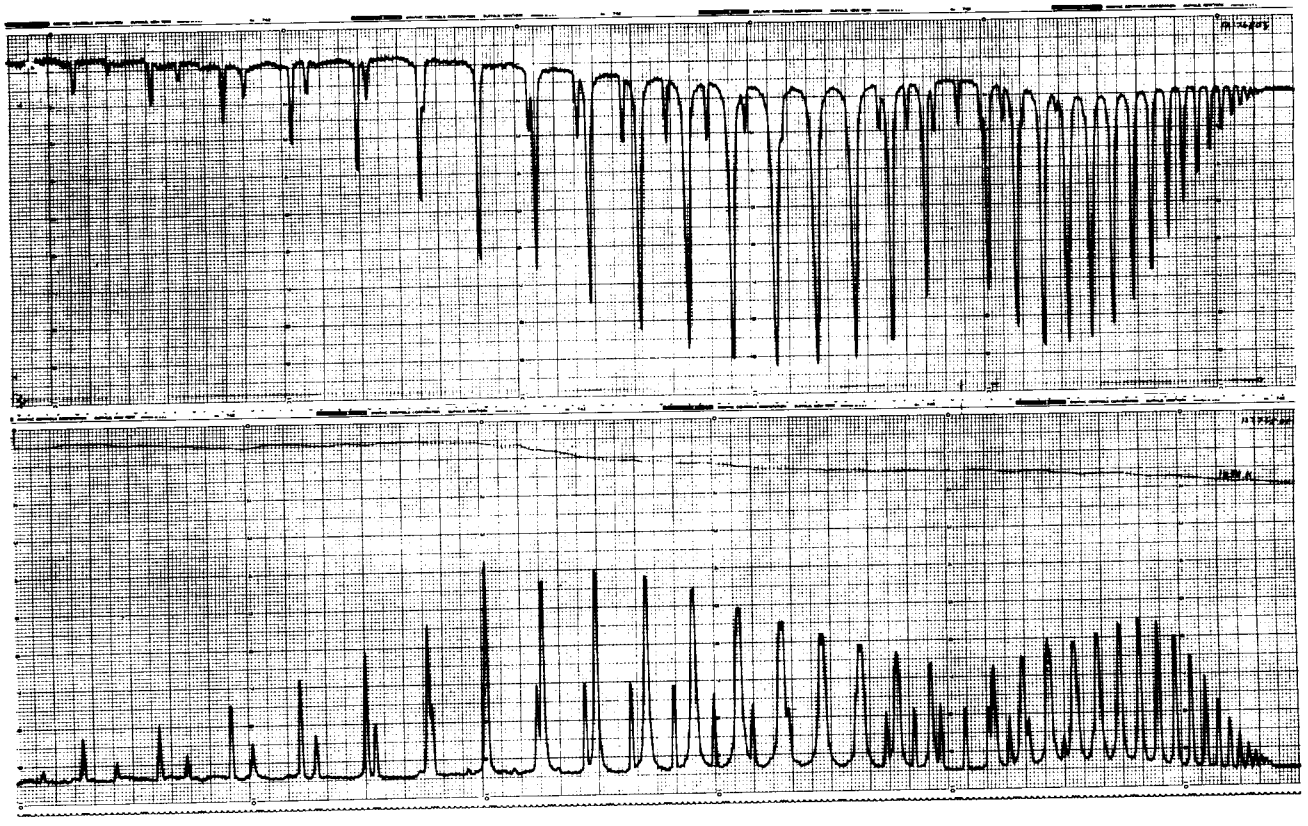

FIGURE B26. EMISSION AND ABSORPTION SPECTRA, RUN 12276804. Gas: HF. P = 367 mm. Temperature (^{O}K) = 645, 1073, 1189, 1209, 1056, 934, 1206, 1182, 1093, 644.

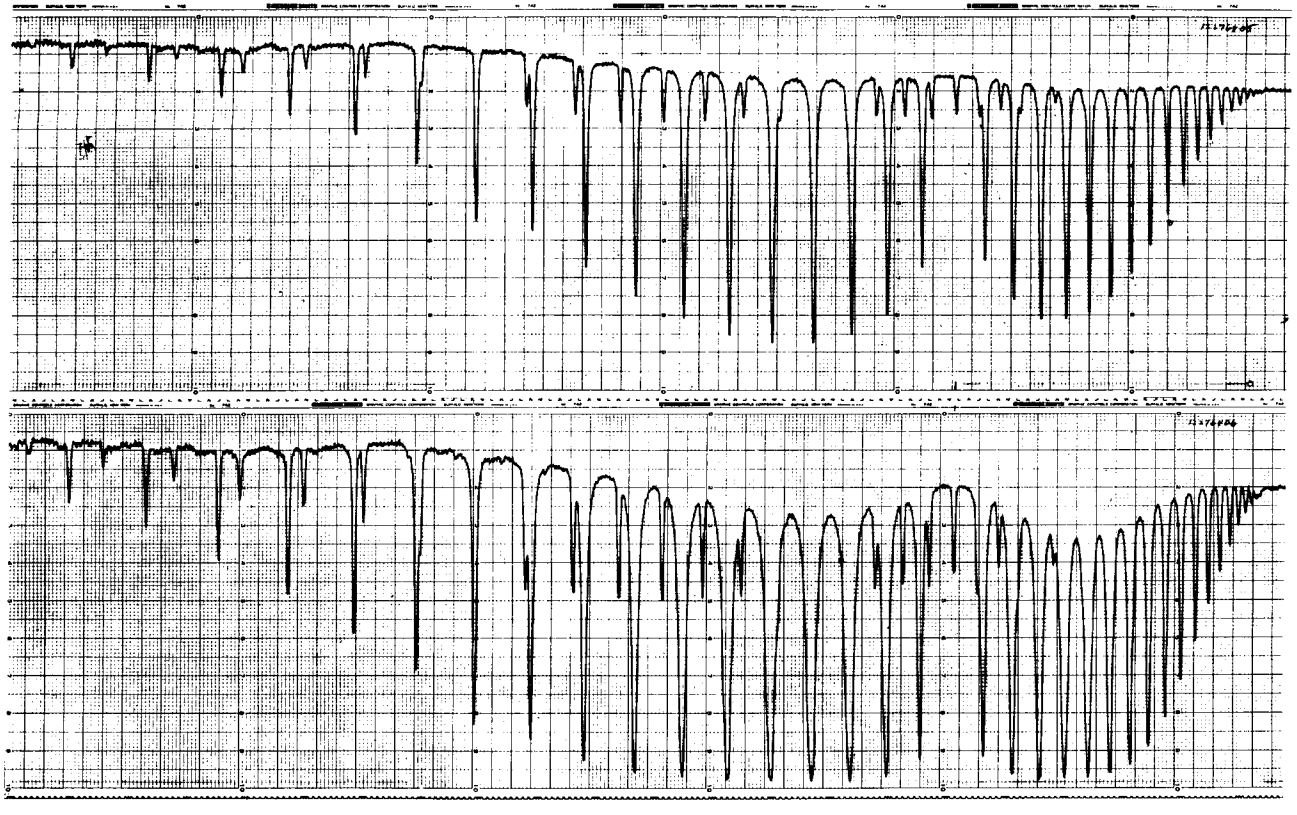

FIGURE B27. ABSORPTION SPECTRA, RUN 12276804 (REPEAT) AND RUN 12276807 (REPEAT). For Run 12276804, gas: HF. P = 367 mm. Temperature (^{O}K) = 645, 1073, 1189, 1209, 1056, 934, 1206, 1182, 1093, 644. For Run 12276807, gas: HF. P = 760 mm. Temperature (^{O}K) = 643, 1046, 1194, 1212, 1060, 934, 1209, 1178, 1074, 643.

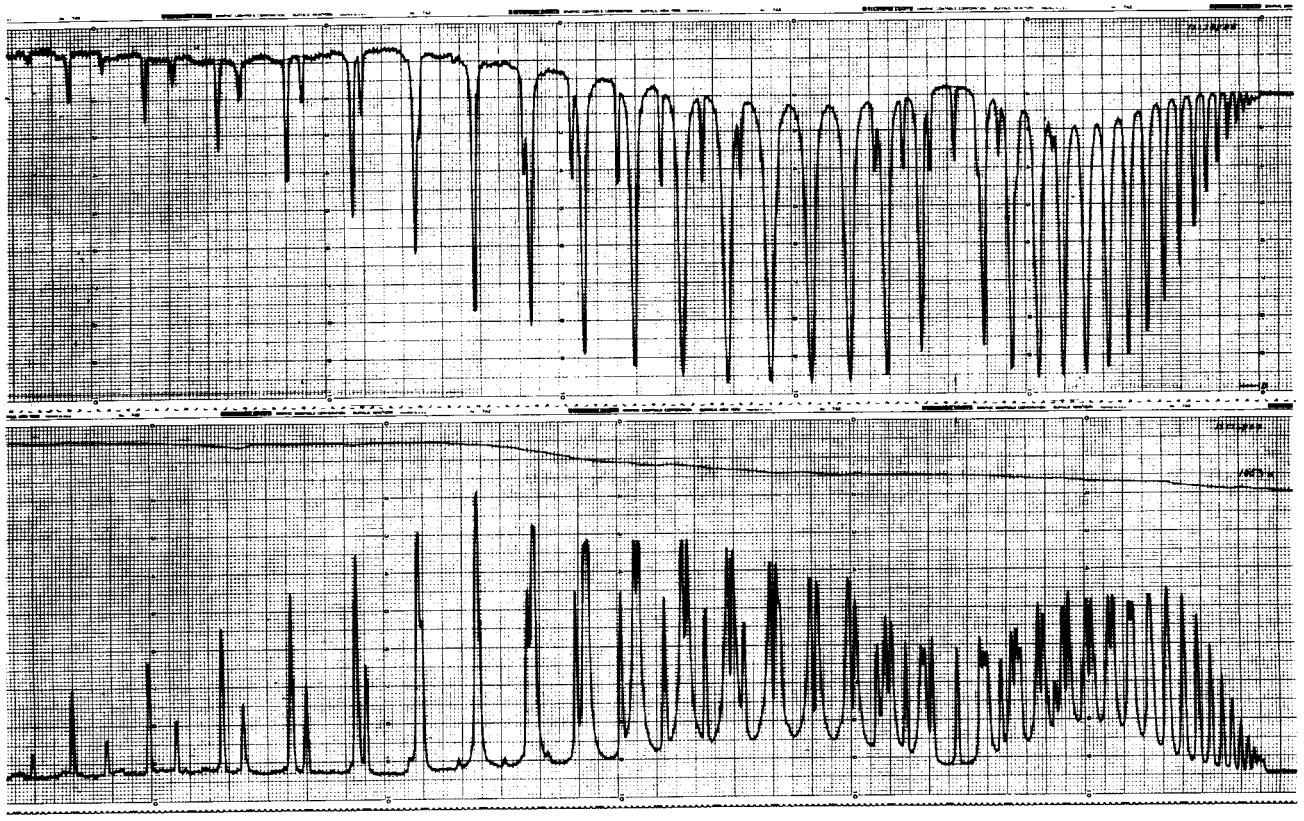

FIGURE B28. EMISSION AND ABSORPTION SPECTRA, RUN 12276807. GAS: HF. P = 760 mm. Temperature (^{O}K) = 643, 1046, 1194, 1212, 1060, 934, 1209, 1178, 1074, 643.

Appendix C
SAMPLE BAND MODEL RADIATION CALCULATION

The programming of equations 16, 17, and 31 for the computation of spectral transmittances, radiances, and apparent temperatures was done in Fortran IV language for The University of Michigan's IBM 360/67 computer. The equations are collected, and steps in the procedure are presented below, along with the printout of a sample calculation at $\nu = 3500\ cm^{-1}$ for run 10246808.

The spectral radiance at the boundary, $\bar{L}_\nu$, is calculated by equations 17, approximated using the trapezoidal rule:

$$\bar{L}_\nu = \sum_{i=1}^{n} L_\nu^*(\bar{\tau}_i)\,(\Delta\bar{\tau})_i$$

in which the spectral transmittance difference $(\Delta\bar{\tau})_i = \bar{\tau}_{i-1} - \bar{\tau}_i$ is obtained from equation 15:

$$\bar{\tau}_i = \exp\,[-\beta_e f(\bar{x}_i)]$$

and

$$\bar{\tau}_0 \equiv 1$$

For a mixture of m absorbing gases:

$$\bar{\tau}_i = \prod_{k=1}^{m} \bar{\tau}_{i,k}$$

The function f(x) is the Ladenburg-Reiche expression:

$$f(x) = xe^{-x}[J_0(ix) - iJ_1(ix)]$$

The argument $\bar{x}$ is the dimensionless optical depth defined by equation 13:

$$\bar{x}_i = \beta_e^{-1} \sum_{j=1}^{i} \bar{k}(T_j)[\beta(T_j)/\beta_e]^{\eta}(\Delta X)_j$$

in which $\bar{k}(T_j)$ is the local value of the first band-model parameter, the average absorption coefficient, corresponding to the average line strength to spacing ratio:

$$\bar{k}(T) = \bar{S}(T)/d$$

$\beta(T_j)$ is the local value of the second band-model parameter, the line-overlap factor, corresponding to the average line width to spacing ratio:

$$\beta(T) = 2\pi\bar{\gamma}(T)/d$$

The optical depth increment is given by

$$(\Delta X)_i = P_i(\Delta L)_i$$

where P_i is the local value of the partial pressure of the radiating species, and $(\Delta L)_i$ is the geometrical path increment. The exponent η is an empirically derived factor given by [5]:

$$\eta = f(0.05\bar{x}_{L,e})\ \sqrt{\pi/(0.1\bar{x}_{L,e})}$$

where the total dimensionless optical depth $\bar{x}_{L,e}$ is the mean between the strong- and weak-line approximations.

The band-model parameters were extracted from the General Dynamics tabulations [12, 32] and entered into the program as two-dimensional tables: $\bar{k}_0$ vs. ν, T and β_0 vs. ν, T with appropriate interpolation subroutines. The tabulated values, k_0, represented the normalization of the experimentally derived values to standard conditions of pressure and temperature to account for the dependency on gas density; accordingly, denormalization consisted of:

$$\bar{k}(\nu, T) = \bar{k}_0(\nu, T)\sqrt{273/T}$$

The pressure dependency is accounted for in the optical depth definition. The tabulated values of the line-overlap factor, β_0, are normalized to a unit effective broadening pressure, defined by

$$P_e = \sum_{k=1}^{m} \alpha_k P_k$$

where $P_{k=1}$ is the value P_i in the optical depth definition; $P_{k>1}$ are the partial pressures of the foreign broadening gases (other species which may or may not be radiating at frequency ν); $\alpha_{k=1} \equiv 1$, and $\alpha_{k>1}$ are the broadening coefficients derived from experimental line-broadening studies. The values of α used in this investigation were extracted from data in the literature [35]:

$\alpha = 0.20$, N_2 broadening H_2O

$\alpha = 0.77$, N_2 broadening CO_2

Thus

$$\beta(\nu, T) = \beta_0(\nu, T)P_e$$

The effective value, β_e, was taken to be the mass-weighted average along the entire path:

$$\beta_e = \frac{\sum_{i=1}^{n} \beta_0(T_i)P_{e,i}(P_i/T_i)(\Delta L)_i}{\sum_{i=1}^{n} (P_i/T_i)(\Delta L)_i}$$

The computation proceeded according to the following steps:

1. Read in:
   (a) Names and number (m) of component gases.
   (b) Frequencies ν_ℓ, $\ell = 1 \ldots q$ (or $\nu_{initial}$, $\Delta\nu$, and number q).
   (c) Incremental lengths $(\Delta L)_i$, $i = 1 \ldots n$ (or total length L and number n).
   (d) Partial pressures, $P_{i,k}$, $i = 1 \ldots n$, $k = 1 \ldots m$.
   (e) Broadening coefficients, α_k, $k = 1 \ldots m$.
   (f) Temperature profile, T_i, $i = 1 \ldots n$.
2. For absorbing gas k = 1:
   (a) Store Program Table I: $k_0(\nu, T)$ vs. ν, T; and Program Table II: $\beta_0(\nu, T)$ vs. ν, T.
   (b) For frequency ν_1:
      (1) Calculate $P_{e,i}$
      (2) Calculate β_e
      (3) Calculate $\bar{x}_{L,w}$ ($\bar{x}_L$ for $\eta = 0$)
      (4) Calculate $\bar{x}_{L,s}$ ($\bar{x}_L$ for $\eta = 1$)
      (5) Calculate $\eta = \eta[(x_{L,w} + x_{L,s})/2]$, using function subprogram in which Program Table III, f(x) vs. x, is stored.
      (6) Calculate $\bar{\tau}_i$, $k = 1$, $\ell = 1$ using Program Tables I, II, and Subprogram Table III, and store $\bar{\tau}_{i,1,1}$, $i = 1 \ldots n$
   (c) Repeat 2(b) for all other ν_ℓ, $\ell = 1 \ldots q$
3. Repeat 2 for next absorbing gas, etc.
4. For ν_1:
   (a) Calculate $\bar{\tau}_{i,1} = \prod_{k=1}^{m} \bar{\tau}_{i,k,\ell}$, $\ell = 1$

(b) Calculate and store $\bar{I}_{\nu_1}$

(c) Calculate and store $(1 - \bar{\tau}_{L,1})$

(d) Calculate $I_{\nu_1}{}^*(T^*)$

(e) Calculate and store T_1^* using Planck function.

5. Repeat 4 for all ν_ℓ, $\ell = 2 \ldots q$.
6. Print out $\bar{L}_{\nu_\ell}$, $(1 - \bar{\tau}_{L,\ell})$, T_i^*, ν_ℓ.
7. Go back to 1 and repeat calculation for other conditions: P_i, T_i, etc.

The following printout for the sample calculation contains, in addition to the normally requested quantities, $\bar{L}_\nu$, $1 - \bar{\tau}_L$, T^*, and ν, for ν_ℓ, $\ell = 1 \ldots q$, the intermediate quantities, $\beta(T_i)$, $\bar{k}(T_i)$, x_i, T_i, $f(x_i)$ and $\bar{\tau}_i$ for $i = 1 \ldots 100$.

```
PLEASE ENTER NAMELIST IN.

&IN GAS='CO2 ',NT=10,TEMP=390.,464.,537.,641.,715.,824.,914.,994.,
1061.,1153.,LENGTH=60.,INU=-10,NU=3500.,MON=10,DAY=24,YEAR=68,
RUN=8,ALPHA=1.,PTAB=1.,NG=1,EXPO=-5.,ITYPE=1,NFREQ=1,NDIV=-100,
TODAY='06/25/69' &END

> INTERPOLATED VALUES OF TEMPERATURE
>    393.33  399.99  406.65  413.31  419.97  426.63  433.29  439.95
>    446.61  453.27  459.93  466.55  473.12  479.69  486.26  492.83
>    499.40  505.97  512.54  519.11  525.68  532.25  539.60  548.96
>    558.32  567.68  577.04  586.40  595.76  605.12  614.48  623.84
>    633.20  642.11  648.77  655.43  662.09  668.75  675.41  682.07
>    688.73  695.39  702.05  708.71  715.54  725.35  735.16  744.97
>    754.78  764.59  774.40  784.21  794.02  803.83  813.64  823.45
>    831.65  839.75  847.85  855.95  864.05  872.15  880.25  888.35
>    896.45  904.55  912.65  920.00  927.20  934.40  941.60  948.79
>    955.99  963.19  970.39  977.59  984.79  991.99  998.35 1004.38
>   1010.41 1016.44 1022.47 1028.50 1034.53 1040.56 1046.59 1052.62
>   1058.65 1066.05 1074.33 1082.61 1090.89 1099.17 1107.45 1115.73
>   1124.01 1132.29 1140.57 1148.85

> PATHLENGTH INCREMENT =   0.60 CM.


> 06/25/69                                        PAGE     1

>        NONISOTHERMAL BAND MODEL CALCULATIONS
>                 (OVERLAPPING LINES)

> RUN   8,ON 10/24/68, L=    60.00 CM, TMP(1)=  393.3
> DEG K,TMP( 100)= 1148.9 DEG K, P(CO2 )= 1.000 ATM
> FREQUENCY    RADIANCE       T STAR          ABSORP.
>  (1/CM)    (W/(CM*STR))     (DEG K)
>
>  3500.0     1.4205E-04     9.0339E 02      0.73046
#
```

> EFFECTIVE TEMPERATURE = 697.27 DEG K.
> EFFECTIVE PRESSURE = 1.00 ATM.

> EFFECTIVE BETA = 0.1061E 02.

BETA/EFFECTIVE BETA	ABSORPTION COEFFICIENT
0.2760E 00	0.3892E-02
0.2891E 00	0.4100E-02
0.3003E 00	0.4301E-02
0.3114E 00	0.4496E-02
0.3225E 00	0.4684E-02
0.3337E 00	0.4866E-02
0.3448E 00	0.5043E-02
0.3560E 00	0.5214E-02
0.3671E 00	0.5381E-02
0.3782E 00	0.5542E-02
0.3894E 00	0.5699E-02
0.4004E 00	0.5851E-02
0.4114E 00	0.5997E-02
0.4224E 00	0.6139E-02
0.4334E 00	0.6277E-02
0.4444E 00	0.6411E-02
0.4554E 00	0.6542E-02
0.4663E 00	0.6670E-02
0.4773E 00	0.6794E-02
0.4883E 00	0.6916E-02
0.4993E 00	0.7034E-02
0.5103E 00	0.7149E-02
0.5286E 00	0.7274E-02
0.5362E 00	0.7429E-02
0.5539E 00	0.7579E-02
0.5695E 00	0.7724E-02
0.5852E 00	0.7864E-02
0.6008E 00	0.8000E-02
0.6164E 00	0.8132E-02
0.6434E 00	0.8767E-02
0.6796E 00	0.9796E-02
0.7158E 00	0.1079E-01
0.7520E 00	0.1176E-01
0.7865E 00	0.1266E-01
0.8123E 00	0.1331E-01
0.8381E 00	0.1395E-01
0.8638E 00	0.1458E-01
0.8896E 00	0.1520E-01
0.9154E 00	0.1580E-01
0.9412E 00	0.1639E-01
0.9669E 00	0.1697E-01
0.9927E 00	0.1754E-01
0.1018E 01	0.1810E-01
0.1044E 01	0.1864E-01
0.1071E 01	0.1920E-01
0.1109E 01	0.1997E-01
0.1147E 01	0.2078E-01
0.1185E 01	0.2145E-01
0.1223E 01	0.2217E-01
0.1261E 01	0.2286E-01

>	0.1299E 01	0.2354E-01
>	0.1336E 01	0.2480E-01
>	0.1374E 01	0.2484E-01
>	0.1412E 01	0.2547E-01
>	0.1450E 01	0.2609E-01
>	0.1488E 01	0.2669E-01
>	0.1520E 01	0.2718E-01
>	0.1551E 01	0.2765E-01
>	0.1583E 01	0.2811E-01
>	0.1614E 01	0.2857E-01
>	0.1645E 01	0.2902E-01
>	0.1677E 01	0.2946E-01
>	0.1708E 01	0.2989E-01
>	0.1739E 01	0.3031E-01
>	0.1771E 01	0.3073E-01
>	0.1802E 01	0.3114E-01
>	0.1834E 01	0.3154E-01
>	0.1862E 01	0.3190E-01
>	0.1890E 01	0.3224E-01
>	0.1918E 01	0.3258E-01
>	0.1946E 01	0.3292E-01
>	0.1973E 01	0.3325E-01
>	0.2001E 01	0.3357E-01
>	0.2029E 01	0.3389E-01
>	0.2057E 01	0.3421E-01
>	0.2085E 01	0.3452E-01
>	0.2113E 01	0.3482E-01
>	0.2141E 01	0.3512E-01
>	0.2165E 01	0.3539E-01
	0.2189E 01	0.3563E-01
>	0.2212E 01	0.3588E-01
>	0.2235E 01	0.3612E-01
>	0.2259E 01	0.3635E-01
>	0.2282E 01	0.3659E-01
>	0.2305E 01	0.3682E-01
>	0.2329E 01	0.3705E-01
>	0.2352E 01	0.3727E-01
>	0.2375E 01	0.3750E-01
>	0.2399E 01	0.3772E-01
>	0.2427E 01	0.3799E-01
>	0.2459E 01	0.3828E-01
>	0.2491E 01	0.3857E-01
>	0.2523E 01	0.3886E-01
>	0.2555E 01	0.3914E-01
>	0.2587E 01	0.3942E-01
>	0.2620E 01	0.3970E-01
>	0.2652E 01	0.3997E-01
>	0.2684E 01	0.4023E-01
>	0.2716E 01	0.4049E-01
>	0.2748E 01	0.4075E-01

> EFFECTIVE MODIFIED OPTICAL DEPTH XE = 0.8699E-02.

> L-R FUNCTION OF XE = 0.8654E-02.

> ETA = 0.1163E 00.

MODIFIED OPTICAL DEPTH	L-R FUNCTION	TRANSMITTANCE
0.1897E-03	0.1895E-03	0.9980E 00
0.3904E-03	0.3900E-03	0.9959E 00
0.6019E-03	0.6011E-03	0.9936E 00
0.8239E-03	0.8228E-03	0.9913E 00
0.1056E-02	0.1055E-02	0.9889E 00
0.1298E-02	0.1296E-02	0.9863E 00
0.1550E-02	0.1548E-02	0.9837E 00
0.1812E-02	0.1809E-02	0.9810E 00
0.2083E-02	0.2079E-02	0.9782E 00
0.2363E-02	0.2358E-02	0.9753E 00
0.2652E-02	0.2645E-02	0.9723E 00
0.2949E-02	0.2942E-02	0.9693E 00
0.3255E-02	0.3246E-02	0.9661E 00
0.3569E-02	0.3559E-02	0.9629E 00
0.3891E-02	0.3880E-02	0.9597E 00
0.4221E-02	0.4208E-02	0.9563E 00
0.4559E-02	0.4544E-02	0.9529E 00
0.4904E-02	0.4887E-02	0.9495E 00
0.5257E-02	0.5238E-02	0.9459E 00
0.5616E-02	0.5595E-02	0.9424E 00
0.5983E-02	0.5960E-02	0.9387E 00
0.6357E-02	0.6331E-02	0.9350E 00
0.6739E-02	0.6710E-02	0.9313E 00
0.7130E-02	0.7098E-02	0.9275E 00
0.7530E-02	0.7495E-02	0.9236E 00
0.7939E-02	0.7900E-02	0.9196E 00
0.8357E-02	0.8315E-02	0.9156E 00
0.8783E-02	0.8737E-02	0.9115E 00
0.9218E-02	0.9167E-02	0.9073E 00
0.9689E-02	0.9634E-02	0.9028E 00
0.1022E-01	0.1016E-01	0.8978E 00
0.1081E-01	0.1074E-01	0.8923E 00
0.1145E-01	0.1137E-01	0.8863E 00
0.1215E-01	0.1206E-01	0.8799E 00
0.1288E-01	0.1279E-01	0.8731E 00
0.1365E-01	0.1355E-01	0.8661E 00
0.1446E-01	0.1435E-01	0.8588E 00
0.1531E-01	0.1518E-01	0.8512E 00
0.1620E-01	0.1605E-01	0.8434E 00
0.1712E-01	0.1696E-01	0.8353E 00
0.1807E-01	0.1790E-01	0.8271E 00
0.1906E-01	0.1887E-01	0.8186E 00
0.2009E-01	0.1987E-01	0.8099E 00
0.2115E-01	0.2091E-01	0.8010E 00
0.2224E-01	0.2198E-01	0.7920E 00
0.2339E-01	0.2310E-01	0.7827E 00
0.2458E-01	0.2426E-01	0.7731E 00
0.2582E-01	0.2547E-01	0.7632E 00
0.2710E-01	0.2672E-01	0.7532E 00
0.2843E-01	0.2801E-01	0.7429E 00

>	0.2980E-01	0.2934E-01	0.7325E 00
>	0.3122E-01	0.3071E-01	0.7219E 00
>	0.3267E-01	0.3213E-01	0.7112E 00
>	0.3417E-01	0.3358E-01	0.7003E 00
>	0.3571E-01	0.3506E-01	0.6894E 00
>	0.3729E-01	0.3659E-01	0.6783E 00
>	0.3891E-01	0.3814E-01	0.6672E 00
>	0.4055E-01	0.3972E-01	0.6561E 00
>	0.4223E-01	0.4133E-01	0.6450E 00
>	0.4394E-01	0.4297E-01	0.6339E 00
>	0.4565E-01	0.4463E-01	0.6228E 00
>	0.4745E-01	0.4632E-01	0.6118E 00
>	0.4925E-01	0.4803E-01	0.6007E 00
>	0.5108E-01	0.4977E-01	0.5898E 00
>	0.5293E-01	0.5154E-01	0.5788E 00
>	0.5482E-01	0.5332E-01	0.5680E 00
>	0.5673E-01	0.5514E-01	0.5571E 00
>	0.5867E-01	0.5697E-01	0.5464E 00
>	0.6064E-01	0.5882E-01	0.5358E 00
>	0.6262E-01	0.6069E-01	0.5253E 00
>	0.6464E-01	0.6258E-01	0.5149E 00
>	0.6667E-01	0.6448E-01	0.5045E 00
>	0.6873E-01	0.6641E-01	0.4943E 00
>	0.7081E-01	0.6835E-01	0.4843E 00
>	0.7291E-01	0.7031E-01	0.4743E 00
>	0.7504E-01	0.7229E-01	0.4644E 00
>	0.7719E-01	0.7428E-01	0.4547E 00
>	0.7936E-01	0.7629E-01	0.4451E 00
>	0.8155E-01	0.7832E-01	0.4357E 00
>	0.8375E-01	0.8035E-01	0.4264E 00
>	0.8598E-01	0.8240E-01	0.4172E 00
>	0.8822E-01	0.8446E-01	0.4082E 00
>	0.9048E-01	0.8653E-01	0.3993E 00
>	0.9276E-01	0.8861E-01	0.3906E 00
>	0.9506E-01	0.9070E-01	0.3820E 00
>	0.9737E-01	0.9281E-01	0.3736E 00
>	0.9970E-01	0.9492E-01	0.3653E 00
>	0.1020E 00	0.9705E-01	0.3572E 00
>	0.1044E 00	0.9918E-01	0.3492E 00
>	0.1068E 00	0.1013E 00	0.3413E 00
>	0.1092E 00	0.1035E 00	0.3336E 00
>	0.1116E 00	0.1057E 00	0.3260E 00
>	0.1141E 00	0.1079E 00	0.3185E 00
>	0.1165E 00	0.1101E 00	0.3111E 00
>	0.1190E 00	0.1123E 00	0.3039E 00
>	0.1215E 00	0.1145E 00	0.2967E 00
>	0.1241E 00	0.1168E 00	0.2898E 00
>	0.1266E 00	0.1190E 00	0.2829E 00
>	0.1292E 00	0.1213E 00	0.2762E 00
>	0.1318E 00	0.1236E 00	0.2695E 00
#			

Appendix D
ILLUSTRATION OF METHOD FOR TEMPERATURE PROFILE DETERMINATION

A typical calculation for the extraction of a temperature profile from observed spectra using a band-model radiative-transfer expression proceeded as follows. From the radiance and absorptance spectra, such as figures B7 and B8 for this example, the apparent temperatures T^* were extracted and plotted as a function of absorptances, as in figure D1. The resultant curves of T^* vs. α were all quite similar (a fact which itself suggests the need for a priori information on the profile shape for reliable analysis) and at first glance simple in shape, approaching asymptotically a constant value for the optically thin extreme, and rapidly decreasing towards a value representing the boundary temperature in the optically dense extreme. However, the shape of the T^* vs. α curves show two salient features: a complex pattern of behavior, quite repeatable, at absorptances between 0.9 and 1.0, and an apparent "hysteresis" in the low-absorptance data between values obtained for the short- and long-wavelength wings of the band. Both of these features are explicable. The first can be accounted for by the fact that apparent temperatures are not functions only of absorptance; at substantial optical depths, the variation of the Planck function and the temperature dependence of the band-model parameters with wavelength appreciably influence the values of the observed radiances, hence apparent temperatures.

The low-absorptance discrepancy, on the other hand, is attributable to an imperfection in the apparatus: the presence of a small amount of light scattered from the grating onto the exit slit of the monochromator. This scattered light appeared only when the continuous blackbody radiance passed through the sample cell during the absorption scans or the beam-balance scans for setting the emission scale. Since this scattered light became completely negligible at frequencies greater than 4000 cm^{-1}, the shorter wavelength data, (the lower sequence of points on the T^* vs. α plots) were therefore weighted more heavily in the fitting of the band-model calculations.

The deduction of the temperature profile was then a simple and straightforward matter. An initial temperature profile was assumed, based on the a priori knowledge of the profile shape. The simplest shape, linear with temperature and increasing along the line of sight from the monochromator, was selected for this illustration. A reasonable initial set of values could be obtained by inspection of the T^* vs. α plot: the initial minimum temperature could be based on the extrapolation to $\alpha = 1$, and an initial maximum temperature taken as the intercept at $\alpha = 0$. The former could be a very realistic estimate; the latter, however, is bound to be

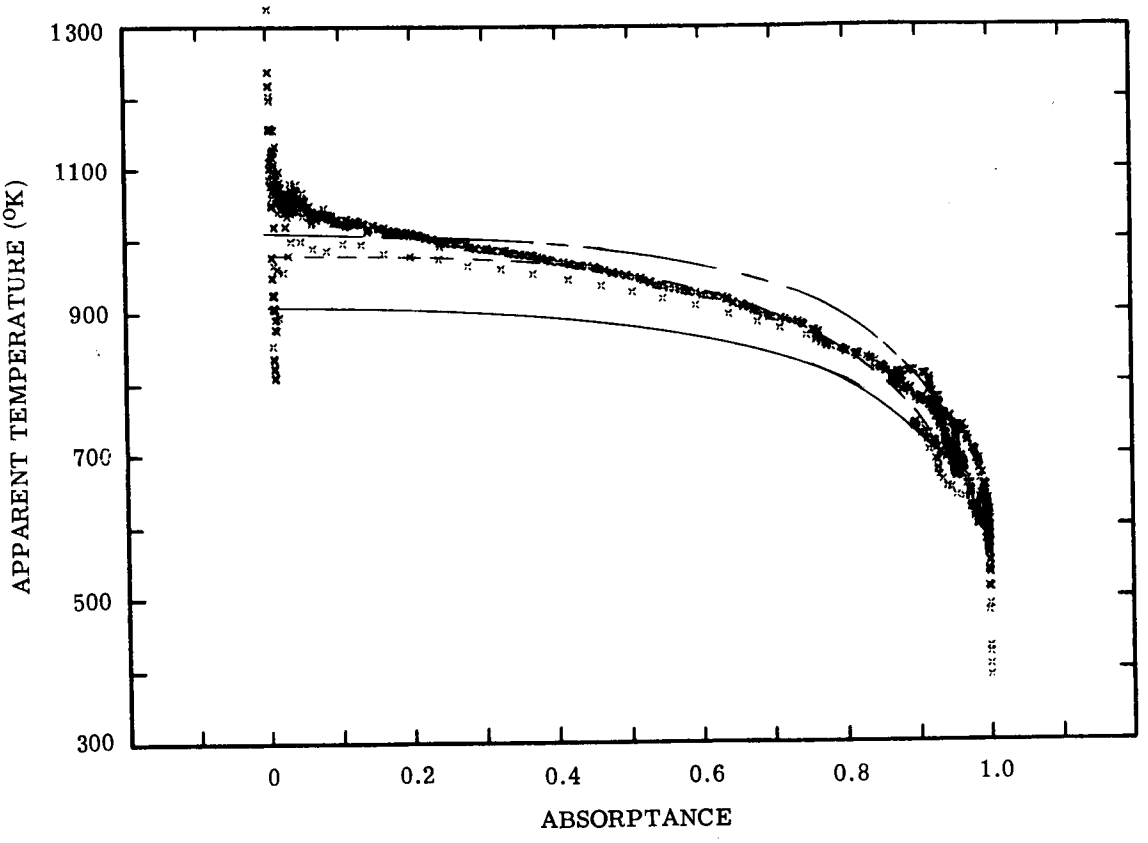

FIGURE D1. FITTING OF BAND-MODEL CALCULATIONS TO OBSERVED VARIATION IN APPARENT TEMPERATURE

considerably lower than the actual maximum temperature, but provided a convenient starting point. Using the band-model expression given by equation (31) in the main text, values of T^* were calculated throughout the band and plotted against absorptance. The assumed temperature profile was then adjusted and the calculation repeated until an optimum fit with the observed data was obtained. In this example, a one-parameter fit was chosen for purposes of illustration; with the minimum temperature taken to be known, the three profiles could be specified by three maximum temperatures. These profiles, shown in figure D3, provided the three curves of calculated T^* vs. α shown in figure C1. (The actual graphical fitting was done on larger scale plots in which the band-model calculations also showed nonuniform variations in the $0.9 < \alpha < 1.0$ region; for purposes of this illustration only the mean curves are shown.) Clearly, the intermediate curve represents the best fit in figure C1; this profile also showed the best agreement with the observed temperatures, as shown in figure C2. For the purposes of this study, such fits were made by inspection; obviously, future analyses programmed for routine applications should include an appropriate mathematical fitting procedure.

For the fits involving adjustments of two or more parameters, many more calculations were required, but the basic approach was the same. The example above illustrated the deduction of a temperature profile in a sample of CO_2. For the case of water vapor, the very same procedure was used. There was, however, an appreciable difference in the appearance of the T^* vs. α plots, namely, a great deal more scatter in the data. This was attributed to the fact that the H_2O line overlapping was not as great as for CO_2. Hence the spectra showed much more rotational line detail; this structure appeared also in the T^* vs. ν plots (cf. figure 7c), as the consequence of an imperfect register of the L_ν vs. ν and $\alpha(\nu)$ vs. ν data in the calculation of $L^*_\nu = L_\nu/\alpha(\nu)$ and hence T^*. This scatter, however, did not introduce any particular difficulty in the judgment of the best fit.

For the case of the isolated line spectra of HF, an exactly analogous procedure was used. In this case, apparent temperatures were calculated using equation 30 and plotted against the generalized rotational quantum number. Again the assumed profiles were adjusted until a best fit was determined by inspection.

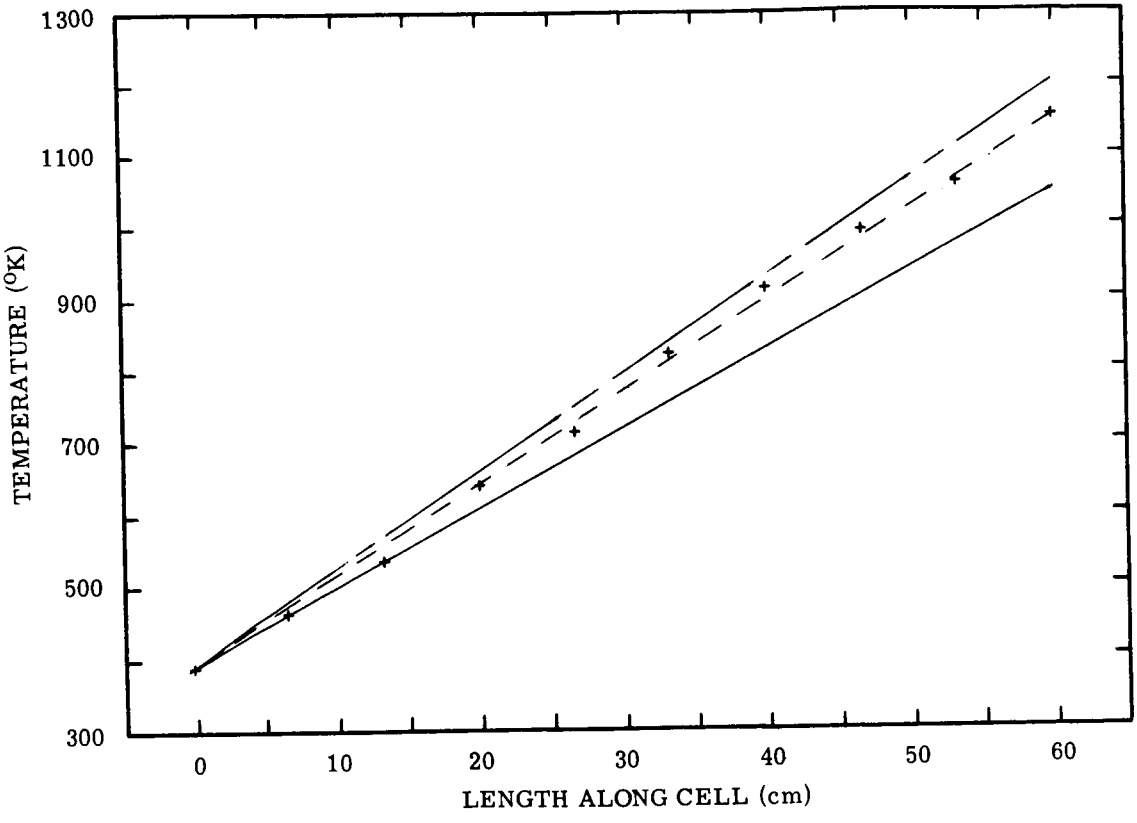

FIGURE D2. TEMPERATURE PROFILE ASSUMED FOR FITTING BAND-MODEL CALCULATIONS TO OBSERVED DATA

Appendix E
SYMBOLS

d	average line spacing
F	$= (\gamma/\gamma_e)^\eta$ or $(\beta/\beta_e)^\eta$, function characterizing variation of line half-width with temperature and pressure
f	= f(x), Ladenburg-Reiche function for line growth
g	slit function of spectrometer
k	spectral absorption coefficient (cm^{-1}-atm^{-1})
L	integrated line radiance (W/cm^2-sr)
L_ν	spectral radiance (W/cm^2-sr-cm^{-1})
L^*_ν	ratio of L_ν to $\alpha(\nu)$ (Planck function of T^*)
m	generalized rotational quantum number (-J for P-branch, J + 1 for R-branch transitions)
P	pressure (atm)
S	line strength (cm^{-2}-atm^{-1})
T	temperature (^oK)
T^*	apparent temperature (^oK) [inverse Planck function of $L_\nu/\alpha(\nu)$]
W	equivalent width of spectral line (cm^{-1})
X	optical depth (cm-atm)
x	dimensionless optical depth
α	spectral absorptance
β	$= 2\pi\bar{\gamma}/d$, line overlap factor
γ	half-width of Lorentz spectral line (cm^{-1})
$\delta\nu$	spectral interval (cm^{-1})
ϵ	spectral emissivity
ν	frequency (cm^{-1})
ρ	reflectance
τ	spectral transmittance

Subscripts

e	effective value (mass-weight average along line of sight)
L	value appropriate for entire path along line of sight
o	reference value
p	value for probability line strength distribution
0	line center

Superscripts

'	variable of integration
–	average over spectral interval $\delta\nu$
*	reference to Planck function
η	empirically determined parameter, $0 < \eta < 1$

REFERENCES

1. S. S. Penner, Quantitative Molecular Spectroscopy and Gas Emissivities, Addison-Wesley (1959).
2. R. W. Ladenburg et al. (eds.), Physical Measurements in Gas Dynamics and Combustion, Princeton University Press (1954).
3. R. H. Tourin, Spectroscopic Gas Temperature Measurement, Elsevier (1966).
4. Temperature, Its Measurement and Control in Science and Industry, Reinhold, Vol. I (1941); Vol. II (1954); Vol. III (1962).
5. F. S. Simmons, Radiances and Equivalent Widths of Lorentz Lines for Nonisothermal Paths, J. Quant. Spectros. Rad. Trans., 7, 111 (1967).
6. H. Y. Yamada, Total Radiances and Equivalent Widths of Doppler Lines for Nonisothermal Paths, J. Quant. Spectros. Rad. Trans., 7, 997 (1967).
7. H. Y. Yamada, Total Radiances and Equivalent Widths of Isolated Lines with Combined Doppler and Collision Broadened Profiles, J. Quant. Spectros. Rad. Trans., 8, 1463 (1968).
8. F. S. Simmons and H. Y. Yamada, Relations for Molecular Radiative Transfer Based on a Random-Line Band Model, Rept. 4613-150-T, Willow Run Laboratories of the Institute of Science and Technology, The University of Michigan, Ann Arbor, February 1967.
9. F. S. Simmons, Application of Band Models to Inhomogeneous Gases, Specialist Conference on Molecular Radiation, NASA TMX 53711 (October 1967).
10. H. Babrov, Instrumental Effects in Infrared Gas Spectra and Spectroscopic Temperature Measurements, J. Opt. Soc. Am., 51, 171 (1961).
11. B. Krakow, H. J. Babrov, G. J. Maclay, and A. L. Shabott, Use of the Curtis-Godson Approximation in Calculations of Radiant Heating by Inhomogeneous Gases, NASA TMX 53411 (1966).
12. C. B. Ludwig et al., Study on Exhaust Plume Radiation Predictions, General Dynamics Corp., NASA CR-61233 (1968).
13. R. M. Huffaker and M. J. Dash, A General Program for the Calculation of Radiation from a Inhomogeneous, Nonisobaric, Nonisothermal Rocket Exhaust Plume, NASA TM-53622 (1967).
14. F. S. Simmons, Further Notes on Band Models for Nonisothermal Radiating Gases, Appl. Opt., 6, 1423 (1967).
15. G. N. Plass, Radiation from Nonisothermal Gases, Appl. Opt., 6, 1995 (1967).
16. A. Goldman, On Simple Approximations to the Equivalent Width of a Lorentz Line, J. Quant. Spectros. Rad. Trans., 8, 829 (1968).
17. D. M. Gates, R. F. Calfee, D. W. Hansen, and W. S. Benedict, Line Parameters and Computed Spectra for Water Vapor Bands at 2.7 μ, NBS Monograph 71 (1964).
18. J. R. Auman, Jr., The Infrared Opacity of Hot Water Vapor, Proceedings of a Conference on Molecular Radiation, NASA TMX 53711 (October 1967).

19. C. B. Ludwig and W. Malkmus, Band Model Representatives for High Temperature Water Vapor and Carbon Dioxide, Specialist Conference on Molecular Radiation, NASA TMX 53711 (October 1967).

20. J. A. L. Thomson, Radiation Model for Nonscattering Rocket Exhaust Gases, Specialist Conference on Molecular Radiation, NASA TMX 53711 (October 1967).

21. B. Krakow, Spectroscopic Temperature Profile Measurements in Inhomogeneous Hot Gases, Appl. Opt., Vol. 5, 201 (1966).

22. L. D. Kaplan, Inference of Atmospheric Structure from Remote Radiation Measurements, J. Opt. Soc. Am., Vol. 49, 1004 (1959).

23. D. T. Hilleary, D. Q. Wark, and D. G. James, An Experimental Determination of the Atmospheric Temperature Profile by Indirect Means, Nature (January 30, 1965).

24. R. A. McClatchey, Sensing of the Earth from Satellites, R. Zirkind (ed.), Polytechnic Press (1965).

25. D. Q. Wark and H. E. Fleming, Indirect Measurements of Atmospheric Temperature Profiles from Satellites, Monthly Weather Rev., Vol. 94, 351 (1966).

26. M. T. Chahine, Determination of the Temperature Profile in an Atmosphere from Its Outgoing Radiation, California Institute of Technology, Jet Propulsion Laboratory, paper submitted to J. Opt. Soc. Am. (1969).

27. S. Twomey, The Application of Numerical Filtering to the Solution of Integral Equations Encountered in Indirect Sensing Measurements, J. Franklin Inst., 279, 95 (1965).

28. F. S. Simmons, An Analytic and Experimental Study of Molecular Radiative Transfer in Nonisothermal Gases, Tenth Symposium on Combustion, The Combustion Institute, Pittsburgh, Pa. (1965).

29. F. S. Simmons, A. G. DeBell, and Q. S. Anderson, A 2000°C Slit-Aperture Blackbody Source, Rev. Sci. Instr., 32, 1265 (1961).

30. R. L. Jarry and W. Davis, Jr., The Vapor Pressure, Association, and Heat of Vaporization of Hydrogen Fluoride, J. Phys. Chem., 57, 600 (1953).

31. F. S. Simmons, C. B. Arnold, and D. H. Smith, Studies of Infrared Radiative Transfer in Hot Gases; I. Spectral Absorptance Measurements in the 2.7 μ H_2O Bands, Rept. 4613-91-T, Willow Run Laboratories of the Institute of Science and Technology, The University of Michigan, Ann Arbor, August 1965.

32. C. B. Ludwig et al., Study on Exhaust Plume Radiation Predictions, General Dynamics/Convair, Repts. DBE 66-017, -001a (1966).

33. R. E. Meredith and N. F. Kent, Line Strength Calculations for the $0 \rightarrow 1$, $0 \rightarrow 2$, $0 \rightarrow 3$, and $1 \rightarrow 2$ Vibration Rotation Bands of HF, Rept. 4613-125-T, Willow Run Laboratories of the Institute of Science and Technology, The University of Michigan, Ann Arbor, April 1966.

34. F. S. Simmons, Infrared Spectroscopic Study of Hydrogen-Fluorine Flames, AIAA J., 5, 778 (1967).

35. D. E. Burch, E. B. Singleton, and D. Williams, Absorption Line Broadening in the Infrared. Applied Optics 1, 359 (1962).

DISTRIBUTION LIST

Addressee	
NASA Lewis Research Center 21000 Brookpark Road Cleveland, Ohio 44135 ATTN: Report Control Office MS 5-5	(1)
NASA Lewis Research Center 21000 Brookpark Road Cleveland, Ohio 44135 ATTN: Technology Utilization Office MS 3-19	(1)
NASA Lewis Research Center 21000 Brookpark Road Cleveland, Ohio 44135 ATTN: Library MS 60-3	(2)
NASA Lewis Research Center 21000 Brookpark Road Cleveland, Ohio 44135 ATTN: Fluid Systems Components Division MS 5-3	(1)
NASA Lewis Research Center 21000 Brookpark Road Cleveland, Ohio 44135 ATTN: I. I. Pinkel MS 5-3	(1)
NASA Lewis Research Center 21000 Brookpark Road Cleveland, Ohio 44135 ATTN: W. L. Stewart MS 77-2	(1)
NASA Lewis Research Center 21000 Brookpark Road Cleveland, Ohio 44135 ATTN: P. Hacker MS 5-3	(1)
NASA Lewis Research Center 21000 Brookpark Road Cleveland, Ohio 44135 ATTN: J. Howard Childs MS 60-4	(1)
NASA Lewis Research Center 21000 Brookpark Road Cleveland, Ohio 44135 ATTN: W. H. Roudebush MS 60-4	(1)
NASA Lewis Research Center 21000 Brookpark Road Cleveland, Ohio 44135 ATTN: John H. DeFord MS 77-3	(1)
NASA Lewis Research Center 21000 Brookpark Road Cleveland, Ohio 44135 ATTN: J. B. Esgar MS 60-4	(1)
NASA Lewis Research Center 21000 Brookpark Road Cleveland, Ohio 44135 ATTN: H. Ellerbrock MS 60-4	(1)
NASA Lewis Research Center 21000 Brookpark Road Cleveland, Ohio 44135 ATTN: L. Macioce MS 60-6	(1)
NASA Lewis Research Center 21000 Brookpark Road Cleveland, Ohio 44135 ATTN: W. T. Olson MS 3-16	(1)
NASA Lewis Research Center 21000 Brookpark Road Cleveland, Ohio 44135 ATTN: Robert R. Hibbard MS 302-1	(1)

Addressee	
NASA Lewis Research Center 21000 Brookpark Road Cleveland, Ohio 44135 ATTN: J. F. Dugan, Jr. MS 501-2	(1)
NASA Lewis Research Center 2100 Brookpark Road Cleveland, Ohio 44135 ATTN: Seymour Lieblein MS 100-1	(1)
NASA Lewis Research Center 21000 Brookpark Road Cleveland, Ohio 44135 ATTN: R. E. Jones MS 60-6	(1)
NASA Lewis Research Center 21000 Brookpark Road Cleveland, Ohio 44135 ATTN: Jack Grobman MS 60-6	(45)
NASA Scientific and Technical Information Facility P. O. Box 33 College Park, Maryland 20740 ATTN: NASA Representative RQT-2448	(6)
FAA Headquarters 800 Independence Avenue, S.W. Washington, D. C. 20553 ATTN: Brigadier General J. C. Maxwell	(1)
FAA Headquarters 800 Independence Avenue, S.W. Washington, D. C. 20553 ATTN: F. B. Howard/SS120	(1)
NASA Headquarters 600 Independence Avenue, S.W. Washington, D. C. 20546 ATTN: N F. Rekos (RAP)	(1)
Department of the Army U. S. Army Aviation Material Laboratory Fort Eustis, Virginia 23604 ATTN: John White	(1)
Headquarters Wright-Patterson AFB, Ohio 45433 ATTN: J. L. Wilkins, SESOS	(2)
AFAPL (APTC) Wright-Patterson AFB, Ohio 45433 ATTN: Lt. D. H. Quick	(1)
Air Force Office of Scientific Research 1400 Wilson Boulevard Arlington, Virginia 22209 ATTN: SREP	(1)
Defense Documentation Center (DDC) Cameron Station 5010 Duke Street Alexandria, Virginia 22314	(1)
Department of the Navy Bureau of Naval Weapons Washington, D. C. 20025 ATTN: Robert Brown, RAPP14	(1)
Department of the Navy Bureau of Ships Washington, D. C. 20360 ATTN: G. L. Graves	(1)
NASA-Langley Research Center Langley Station Technical Library Hampton, Virginia 23365 ATTN: Mark R. Nichols	(1)
NASA-Langley Research Center Langley Station Technical Library Hampton, Virginia 23365 ATTN: John V. Becker	(1)

Addressee	
United States Air Force Aero Propulsion Laboratory Building 18D, Room 119 Wright-Patterson AFB, Ohio 45433 ATTN: Robert E. Henderson	(1)
United States Air Force Cambridge Research Center Electronics Research Center L. G. Hanscom Field, Bedford, Massachusetts 01730 ATTN: Library	(1)
United Aircraft Corporation Pratt and Whitney Aircraft 400 Main Atreet East Hartford, Connecticut 06108 ATTN: G. Andreini	(2)
United Aircraft Corporation Pratt and Whitney Aircraft Division 400 Main Street East Hartford, Connecticut 06108 ATTN: Library	(1)
United Aircraft Research East Hartford, Connecticut 06027 ATTN: Library	(1)
Allison Division of GMC Department 8894, Plant 8 P. O. Box 894 Indianapolis, Indiana 46206 ATTN: J. N. Barney	(1)
Allison Division of GMC Department 8894, Plant 8 P. O. Box 894 Indianapolis, Indiana 46206 ATTN: G. E. Holbrook	(1)
Allison Division of GMC Department 8894, Plant 8 P. O. Box 894 Indianapolis, Indiana 46206 ATTN: Library	(1)
Northern Research and Engineering Corporation 219 Vassar Street Cambridge, Massachusetts 02139 ATTN: K. Ginwala	(1)
General Electric Company Flight Propulsion Division Cincinnati, Ohio 45215 ATTN: J. W. McBride H-44	(1)
General Electric Company Space Sciences Laboratory King of Prussia, Pennsylvania 19406	(1)
General Electric Company Flight Propulsion Division Cincinnati, Ohio 45215 ATTN: C. Danforth H-32	(1)
General Electric Company Flight Propulsion Division Cincinnati, Ohio 45215 ATTN: Technical Information Center N-32	(1)
General Electric Company 1000 Western Avenue West Lynn, Massachusetts 01905 ATTN: Dr. C. W. Smith, Library Building 2-40M	(1)
Curtiss-Wright Corporation Wright Aeronautical Division Wood-Ridge, New Jersey 07075 ATTN: S. Lombardo	(1)
Curtiss-Wright Corporation Wright Aeronautical Division Wood-Ridge, New Jersey 07075 ATTN: G. Provenzale	(1)

Addressee	
Air Research Manufacturing Company 402 South 36th Street Phoenix, Arizona 85034 ATTN: Robert O. Bullock	(1)
Air Research Manufacturing Company 9851 Sepulveda Boulevard Los Angeles, California 90009 ATTN: Dr. N. Van Le	(1)
AVCO Corporation Lycoming Division 550 South Main Street Stratford, Connecticut 06497 ATTN: Claus W. Bolton	(1)
AVCO Corporation Lycoming Division 550 South Main Street Stratford, Connecticut 06497 ATTN: Charles Kuintzle	(1)
Continental Aviation and Engineering Corporation 12700 Kercheval Detroit, Michigan 48215 ATTN: Eli H. Bernstein	(1)
Continental Aviation and Engineering Corporation 12700 Kercheval Detroit, Michigan 48215 ATTN: Howard C. Walch	(1)
International Harvester Company Solar Division 2200 Pacific Highway San Diego, California 92112 ATTN: P. A. Pitt	(1)
International Harvester Company Solar Division 2200 Pacific Highway San Diego, California 92112 ATTN: Mrs. L. Walper	(1)
Goodyear Atomic Corporation Box 628 Piketon, Ohio 45661 ATTN: C. O. Langebrake	(1)
George Derderian AIR 53622 B Department of the Navy Bureau of Navy Washington, D. C. 20360	(1)
The Boeing Company Missile and Information Systems Division 224 N. Wilkinson Street Dayton, Ohio 45402 ATTN: Warren K. Thorson	(1)
North American Rockwell Corporation Rocketdyne Division Canoga Park, California 91305 ATTN: W. Herget	(1)
The Southwest Center for Advanced Studies P. O. Box 30365 Dallas, Texas 75230 ATTN: Gilbert N. Plass	(1)
Aerojet-General Corporation Sacramento, California 95809 ATTN: M. S. Nylin	(1)
Aerojet-General Corporation Sacramento, California 95809 ATTN: Library	(1)
New England Materials Laboratory, Incorporated 35 Commercial Street Medford, Massachusetts 02155 ATTN: Allan S. Bufferd	(1)
Cornell Aeronautical Laboratory 4455 Genessee Street Buffalo, 21, New York 14204	(1)
Marquardt Corporation 16555 Saticoy Street Van Nuys, California 91406	(1)

Addressee	
Thompson Ramo Wooldridge 7209 Platt Avenue Cleveland, Ohio 44104	(1)
Aro, Incorporated Arnold Air Force Station, Tennessee 37389	(1)
S. C. Fiorello Aeronautical Engine Laboratory Naval Air Engineering Center Philadelphia, Pennsylvania 19112	(1)
Aerospace Research Laboratory Wright-Patterson AFB, Ohio 45433 ATTN: Dr. R. G. Dunn	(1)

Addressee	
NASA-MSFC Aero-Astrodynamics Laboratory Huntsville, Alabama 35812 ATTN: Werner K. Dahm	(1)
General Dynamics/Convair Space Science Laboratory San Diego, California 92112 ATTN: C. B. Ludwig	(1)
Warner & Swasey Control Instrument Division 32-16 Downing Street Flushing, New York 11354 ATTN: R. H. Tourin	(1)